Muscle mechanics and hydrodynamics of jet propulsion swimming in marine invertebrates

Thomas Robert Neil

Submitted in accordance with the requirements for the degree of
Doctor of Philosophy

The University of Leeds
Faculty of Biological Sciences
School of Biomedical Sciences

July 2016

Intellectual property rights

The candidate confirms that the work submitted is his own and that appropriate credit has been given where reference has been made to the work of others.

This copy has been supplied on the understanding that it is copyright material and that no quotation from the thesis may be published without proper acknowledgement.

Declaration

The work carried out in this thesis was supported by several individuals. Dr Graham Askew assisted in the collection of all the data gathered in chapter two. Marion Kaufmann instrumented the animals and collected the majority of the *in vivo* power output measurements of the king scallops. Dr David Ellerby provided laboratory space and equipment at Wellesley College for the collection of the bay scallop data. Dr Richard Marsh assisted with the instrumenting and swimming of the bay scallops. Dr Graham Askew assisted with muscle preparations, equipment set up and analysis in chapter three. Dr Graham Askew assisted in data analysis and the implementation of equations in chapters four, five and six.

Acknowledgements

First and foremost I would like to thank Dr Graham Askew for giving me this great opportunity to study in his laboratory and provide invaluable guidance throughout my PhD. I have learnt a great deal under his supervision and the work we have done together has been both interesting and a great deal of fun.

I would like to thank Dr Richard Marsh and Dr David Ellerby for their assistance with data collection at Wellesley college. In particular I would like to give thanks to Rich and his wife Judy for putting Graham and I up for three weeks and taking very good care of us!

Thank you to all my lab mates past and present, I'm glad you came along for the ride and made this whole process an enjoyable one, I will forever have fond memories of lunch time crosswords, sporcle and gun fights.

Thank you to Yazi for making our time in Leeds special and putting up with me this whole time, unfortunately I'm not going to stop talking about the sea any time soon.

I would also like to thank my family for all their support despite never really understanding what it was I was doing.

Finally, thanks go to the EPSRC for funding this research and making this whole project possible.

Abstract

Locomotion amongst animals is widespread and diverse. Movement is of fundamental biological importance to animals, enabling them to forage, migrate, pursue prey and mate. Animals have evolved a great range of locomotor mechanisms that span huge size ranges and diversity across the animal kingdom, yet several common principles underlie most of these mechanisms, the understanding of which can help explain why certain biological locomotor systems have evolved for particular environments.

Constraints on an animal's morphological traits are bought about by body size, meaning that several aspects of locomotor performance are found to vary with body mass. Burst performance plays a crucial role in many animals lives, with the ability to accelerate and manoeuvre quickly often being essential for survival. The power available from the muscles during this type of locomotion is generally thought to decrease with increasing body size, with cycle frequency predicted to limit maximal muscle mass-specific performance. Muscle mass-specific power was measured *in vivo* in scallops covering a 96-fold range in body mass. Power was measured using sonomicrometry crystals to measure muscle length changes during swimming whilst pressure was simultaneously monitored within the mantle cavity.

The scaling of the contractile characteristics of the adductor muscles of scallops was investigated to determine what affect the intrinsic properties of the muscle have on the scaling of muscle power output. Muscle fibre bundles were dissected and attached to a force transducer to measure force and muscle length change. Muscles were electrically stimulated via platinum plate electrodes. The scaling of twitch kinetics and the force velocity relationship were characterised *in vitro*.

Jet propulsion via pulsed jets have been shown to be able to produce more thrust per unit of ejected fluid then an equivalent steady jet. The benefit is bought about through the production of isolated vortex rings, which entrain additional ambient fluid into the wake. There are numerous biological swimmers that use jet propulsion as their primary form of locomotion, however, their ability to be able to use vortex rings to enhance their propulsive performance has only been investigated in a few systems.

Jet wake structure and swimming performance were quantified in three animals that swim by jet propulsion; scallops, *Nautilus* and jellyfish. The properties of the wakes were characterised using particle image velocimetry to measure the wake structure of the jets that were produced.

Muscle mass-specific power output was found to decrease with increasing size in scallops. Frequency decreased with increasing size, muscle stress was found to be approximately constant whilst muscle strain decreased with increasing size in king scallops. The scaling exponents for muscle power were greater than those of the scaling of cycle frequency, suggesting that cycle frequency is not the sole determinant of the scaling of muscle power output.

Muscle power output measured *in vitro* was also found to decrease with increasing body mass, but scaled with an exponent greater than that measured *in vivo*. The $V_{\max}$ of the muscles decreased with increasing size, but did not scale in the same way as cycle frequency, suggesting that the intrinsic contractile properties of the muscle were not the sole determinant of cycle frequency in scallops.

King scallops and *Nautilus* were found to produce two distinct jet modes, one in which isolated vortex rings were produced (Jet mode 1) and one which consisted of a leading vortex ring followed by a trailing jet of fluid (Jet mode 2). No differences were found in jet mode and the thrust produced from the jet, although enhanced thrust was found in king scallops producing jets at formation numbers of ~4. The wake structure of Rhizostomeae jellyfish revealed that they propel themselves via and interaction of two vortex rings that are produced as they swim. They were also found to manipulate the formation of a vortex ring that is formed as they swim, manoeuvring it to within their sub-umbrella cavity, providing them with an additional boost during swimming.

Table of Contents

List of Tables

List of Figures

List of Abbreviations

a	acceleration
A	constant
A_1	constant
A_v	valve area
A_j	jet orifice area
A_m	muscle cross sectional area
A_r	jet refill area
b	distance from hinge to sonomicrometry hole
B	constant
B_1	allometric relationship of the valve size
C	constant
Ca^{2+}	calcium
CoL	cost of locomotion
D	cylinder diameter
D_j	jet diameter based on vorticity peaks
DC	duty cycle
f	frequency
F	formation number
F_p	average propulsive force
I	momentum
L	length of column of fluid
L_j	jet length
L_0	muscle operating length
L_ap	anterior-posterior shell length

L_{cl}	closed muscle length
L_{dv}	dorsal-ventral shell length
L_{iv}	inter-valve distance
L_{max}	maximum muscle length during swimming
L_s	short length of an ellipses
L_{sh}	shell height
L_{ve}	sonomicrometry inter-valve distance
M_b	body mass
M_{hi}	hinge moment
M_m	muscle mass
n	frame number
P_0	maximum tetanic force
P^o	pressure
r	vortex ring radius
Re	Reynolds number
S	slip
t	time
T	thrust
t0.5r	time to 50% relaxation
t_c	twitch contraction time
t_{cd}	cycle duration
t_j	jet duration
tPtw	twitch rise time
t_r	refill duration
U	swimming speed

$\bar{U}$	average swimming speed
U_f	final velocity
U_i	initial velocity
$\bar{u}_\mathrm{j}$	average jet velocity
$\bar{u}_\mathrm{r}$	average refill velocity
v	animal velocity
V	velocity of shortening
v_wake	acceleration of water mass
$V_\mathrm{\beta}$	angular velocity of the valves
V_exp	expellable water volume
$\dot{V}_\mathrm{exp}$	water flow rate
V_iv	proportion of inter-valve volume occupied by adductor muscle
V_max	maximum shortening velocity
V_sh	muscle shortening velocity
V_v	inter-valve volume
W	work
x, y	co-ordinates describing two dimensional position of animal
$x_\mathrm{c}, y_\mathrm{c}$	co-ordinates of the centroid of the valve determined relative to the hinge
β	jet angle
β_0	constant
β_hi	hinge angle
Γ	vortex ring circulation
ε	strain
η_p	passive whole-cycle swimming efficiency
η_{wc}	whole-cycle swimming efficiency

Π	muscle power
Π^*	muscle mass-specific power
$\overline{\Pi}^*$	net muscle mass-specific power
$\overline{\Pi}^*_{\mathrm{hi}}$	average hinge power
Π^*_{max}	maximum mass-specific isotonic muscle power
ρ	water density
ρ_{M}	muscle density
σ	mean stress difference
τ	proportion of cycle spent shortening

Chapter 1

General Introduction

Movement is an essential component to life in most animals, enabling them to forage, migrate, escape from predators and search for mates. Natural selection has driven the evolution of animal locomotor performance, shaping numerous different strategies for an animal to move; with each one tuned to best suit each animal's specific needs.

The study of animal locomotion stretches from the molecular level to whole animal biomechanics. Muscles are the driving force of animal movement. Numerous methods have been developed to characterise the structure and properties of muscle and relate these to function and impact on locomotor performance.

1.1 Muscle function during locomotion

Animals generate the forces required to move through the contraction of their locomotory muscles. Muscles can operate isometrically i.e. at a constant length, resulting in no work net being done, or can be actively shortened or stretched to either produce positive or negative work, respectively. The rate at which work is produced yields the power output of that muscle. Isometric contractions may contribute to more economic force generation, or towards tendon elastic energy recovery (Biewener et al., 1998). Active shortening of muscles often results in limb movement due to the work the muscle is doing on a specific body part, whilst muscles undergoing active lengthening will absorb energy to aid in the control of inertial movements (Biewener and Daley, 2007). Additionally, force development and the amount of work done during shortening can be enhanced if a muscle undergoes a brief period of active stretch whilst lengthening (Edman et al., 1978). The force a muscle is able to produce and the velocity at which it shortens are affected by the timing of muscle activation and deactivation, and the changes in load that occur during locomotion (Biewener and Gillis, 1999). This results in muscle force and velocity varying with time, with conditions in which they are constant being rare. As such, the study of muscle physiology and function must be coupled with an understanding of the dynamics of animal locomotor systems.

1.1.1 Quantifying *in vitro* muscle characteristics

The physiological characteristics of a muscle can be investigated *in vitro* using an isolated muscle or a bundle of fascicles from an animal. The isolated fibres can be kept alive by bathing them in oxygenated Ringer's solution. One end of the muscle is attached to an immovable pin or clamped down, with the other end being attached to the lever arm of a force transducer. In the absence of a nervous system, the muscle is stimulated by applying an electrical current either to the muscle directly, or to the solution that the muscle is sitting in.

1.1.2 Isometric muscle performance

Muscles can be held at a constant length (isometric conditions) under *in vitro* conditions and be stimulated to contract via the application of an electrical impulse. A single electrical stimulus results in the muscle producing a twitch. During a twitch the tension in the muscle rises quickly, resulting in a sharp increase in force before tension is restored to resting levels. If several stimuli are applied in rapid succession the muscle will contract maximally, with force reaching a plateau before relaxing again, resulting in mechanical summation. The value of the plateau reached is that muscles' maximal isometric force. The amount isometric force is largely dependent on the initial sarcomere length of the muscle. Sarcomere length determines the amount of overlap between the thick and thin filaments, which in turn affects the number of cross bridges that are formed and therefore the force generated (Huxley, 1957). Maximal isometric force is achieved at a sarcomere length which gives maximal overlap between the thick and thin filaments (Gordon et al., 1966). Muscles activation and contraction occurs due to the release of calcium (Ca^{2+}) from the sarcoplasmic reticulum, which binds the contractile proteins. Muscles are subsequently deactivated and relax when Ca^{2+} is released from these binding sites and sequestered by the sarcoplasmic reticulum (Ebashi and Endo, 1968). The time course of these events are referred to as twitch kinetics, and relate to the rate of activation and deactivation of a muscle.

1.1.3 The force velocity relationship

The amount of force that a muscle is capable of producing is related its shortening velocity. As muscle shortening velocity increases, the amount of force it can produce decreases. If the force produced by a muscle equals the load acting on it, the muscle will contract isometrically, producing its maximal isometric force (P_0). If the muscle contracts against no load, it will achieve its maximum shortening velocity (V_{max}).

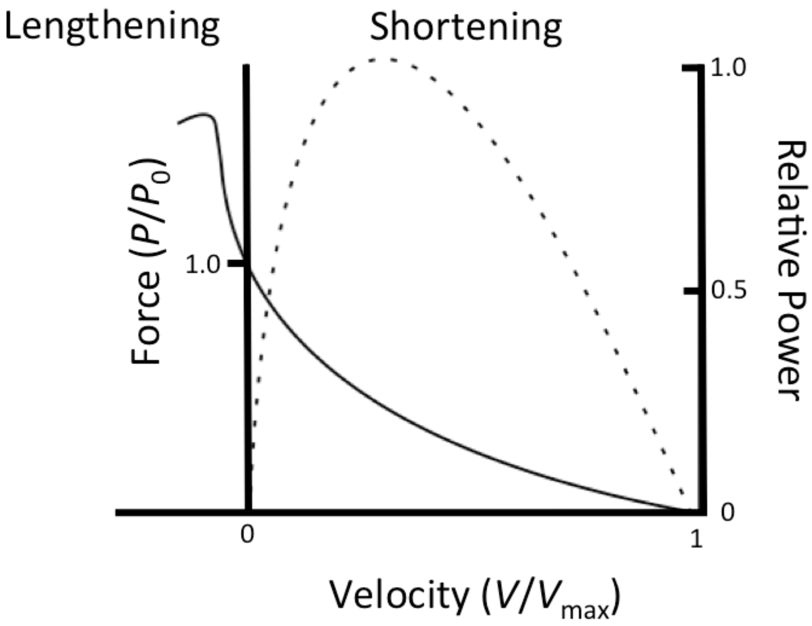

Figure 1.1 Representative force-velocity relationship obtained from after-loaded isotonic measurements. Schematic shows force velocity (solid line) and power velocity (dashed line) relationships. Adapted from Biewener (2003).

If a muscle shortens whilst producing force it will produce positive work. Alternatively, if the load placed on the muscle exceeds the maximum amount of force the muscle can produce, the muscle will be actively lengthened, resulting in negative work.

The relationship between force and velocity was first described by Hill (1938) as being hyperbolic. Subsequent research revealed that at high levels of *P*, a hyperbolic linear equation better described the relationship (Marsh and Bennett, 1985) and could be calculated as:

$$V = [B(1 - P/P_0)/(A+P/P_0)]+C(1 - P/P_0) \qquad [1.1]$$

Where P is force and V is the velocity of shortening. A, B and C are constants. Figure 1.1 shows a typical force velocity relationship curve, with velocity increasing as the load the muscle is acting on decreases. The relationship between force and velocity in muscles results in peak power output being achieved at relative shortening velocities (V/V_{max}) of around 0.3, though the value depends on the curvature of the force-velocity relationship. Studies into *in vivo* muscle mechanical performance have since shown that some muscles do operate around this value during locomotion (Lutz et al., 1994; Rome et al., 1990), although work on jumping muscles in frogs has shown that not all muscles will operate at V/V_{max} ratios close to those that yield peak power output *in vitro* (Marsh, 1994).

1.1.4 *In vivo* muscle mechanical performance

The force- velocity relationship is derived under simple isometric, isovelocity or isotonic conditions when muscles are maximally activated, and does not faithfully replicate how most muscles operate *in vivo*. During locomotion muscles typically undergo cyclical contractions, experiencing a range of length trajectories and activation patterns (Girgenrath and Marsh, 1997; Roberts et al., 1997), all of which affect muscle performance.

Numerous studies have looked to determine muscle performance *in vivo*. Muscle mechanical function *in vivo* can be determined by measuring the muscle's length trajectory and pattern of force generation. Force can be determined either directly (e.g. via strain gauges attached to bony tendons or bones; Roberts et al., 1997; Biewener et al., 1992) or indirectly (e.g. in vitro by measuring force under simulated patterns of lengthening and activation). Electromyography (EMG) is used to determine the electrical activity of the muscle, whilst sonomicrometry allows for the accurate measurement of muscle length change during locomotion. Electromyography measures the local potential difference across a muscle membrane as it depolarises in response to an action potential. This gives a measure of the muscle activation pattern in relation to an associated muscle contraction. Sonomicrometry involves the insertion of signal generating piezoelectric crystals into the muscle, the distance between crystals is then calculated based on the speed of the acoustic signal through the muscle. Marsh et al. (1992) was amongst the first to use such techniques in order to determine muscle performance in swimming scallops. The method has since been applied to a wide range of species with varying locomotor strategies (Ellerby and Askew, 2007; Roberts et al., 2007). These studies revealed a great deal about how altering muscle length trajectories and activation patterns can affect *in vivo* locomotion, but they do not reveal how *in vivo* muscle mechanical performance is affected by these changes. In order to gain an insight into this, knowledge gained from *in vivo* studies must be combined with *in vitro* techniques of determining muscle mechanical performance.

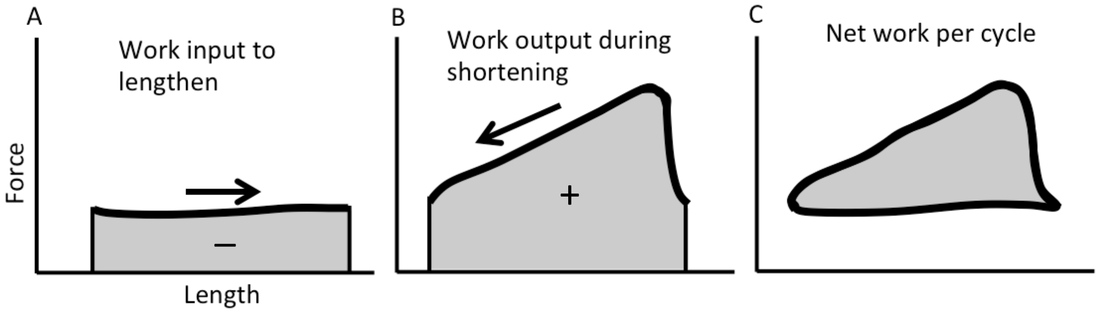

Figure 1.2. Representative work loop. Negative work is done as the muscle is lengthened (A). Positive work is done as the muscle shortens (B). The area enclosed by the loop represents the net work done by the muscle over one cycle. The loop is counter clockwise, representing positive net work. Adapted from Josephson (1985).

1.1.5 The Work Loop Technique

The work loop technique has bridged the gap between *in vivo* muscle function and *in vitro* muscle mechanical performance. Isolated muscle fibres or muscle fibre bundles are subject to length changes and activation patterns that replicate those that the muscle undergoes *in vivo*. Force produced by the muscle during these length changes is measured, allowing for work and power output to be calculated. Work is done on a muscle as it is lengthened, referred to as negative work (fig. 1.2A), whereas a muscle undergoing shortening will produce positive work (fig. 1.2B). The net mechanical work is calculated as positive work minus negative work (fig. 1.2C), the mechanical power output of the muscle is determined as work multiplied by cycle frequency (Pennycuick, 2008).

Several studies have been able to demonstrate the validity of the work loop technique. Early experiments used sinusoidal length changes to simulate *in vivo* conditions (e.g. Josephson, 1985; Josephson and Darrell, 1989). Later experiments used measured *in vivo* length changes to better simulate *in vivo* conditions where sinusoidal length changes were not appropriate. Marsh et al. (1992) obtained power measurements from swimming scallops both *in vivo* and *in vitro* using the work loop technique. *In vivo* power measurements were obtained by measuring pressure within the mantle cavity of the scallop as well as the rate of change in volume within the scallop during swimming. Marsh and Olson (1994) were then able to use the data gathered on the *in vivo* phase of activation and the length cycle changes in the adductor muscle of scallops to design an *in vitro* contractile system that was able to accurately recreate the natural cycle of the muscle. Average performance was quantitatively compared in *in vivo* and *in vitro* conditions through calculations including average work and peak power output. It was found that the power determined *in vitro* was not significantly different from that measured *in vivo*, confirming that the magnitude and profile of power generation determined using the work loop technique replicates muscle performance *in vivo*. Other works have since gone on to reveal even more about the *in vivo* mechanical performance of muscles using the work loop technique (Askew and Marsh, 1997; Askew and Marsh, 1998), allowing us to gain a more detailed understanding of how changes in activation patterns and length changes can effect muscle performance, and allow for the impact of these changes to *in vivo* locomotor performance to be explored.

1.2 The scaling of muscle power output

Escape behaviour in animals is under strong selective pressure due to the importance of such a response to an animal's survival. Muscles produce the power required for this locomotion, with the available power ultimately setting the limits on animal performance. Throughout growth an animal's body size will impose constraints on both the morphological and physiological traits associated with locomotor performance. Maximal performance depends on how power scales with body mass, the performance of escape locomotion associated with predator avoidance is generally thought to decrease with increasing body size (Emerson, 1978; Huey and Hertz, 1982).

1.2.1 Theoretical approaches to the scaling of maximum muscle power output

Hill (1950) was the first to consider scaling relationships for the scaling of muscle power, these early works were theoretical in approach and were based on the intrinsic properties of the muscle and assumptions about the geometric similarity of the animals and the contractile properties of their muscles. In Hill's approach both myofibrillar stress (σ) and muscle strain (ε) were assumed to be constant. Muscle length was predicted to scale with body mass (M_b) as $M_b^{1/3}$, muscle cross sectional area as $M_b^{2/3}$ and muscle mass (M_m) as M_b^1. The frequency at which a muscle contracts is predicted to scale inversely with limb length, as $M_b^{-1/3}$. As muscle strain is predicted to be constant, a muscle's maximum shortening velocity (V_{max}) is proportional to frequency. V_{max} should then scale as $M_b^{-1/3}$, assuming no differences in the shape of the force-velocity relationship. According to Hill's model, muscle mass-specific power is predicted to scale in proportion to a muscle's operating frequency ($M_b^{-1/3}$), resulting in the prediction that larger animals would be producing lower mass-specific power outputs than smaller animals.

McMahon (1973) proposed an alternative model. In his model animals were assumed to have the same elastic deflection of body structures under their own static weight. Similar sized animals would be designed in such a way as to maintain elastic similarity to each other in the sense that their limbs would be under a similar threat of failing due to buckling. Similarly to Hill's model, myofibrillar stress was predicated to be constant; muscle strain however was predicted to scale as $M_b^{-1/8}$. Muscle length was predicted to scale with body mass as $M_b^{1/4}$ and muscle cross sectional area as $M_b^{3/4}$. McMahon's model predicts limb oscillatory frequency to scale as $M_b^{-1/8}$, whilst the limbs of smaller animals are predicted to undergo greater angular excursions, thus predicting muscle mass-specific power to scale as $M_b^{-1/4}$ (Seow and Ford, 1991).

1.2.2 Experimental studies

Hill (1950) theorised that animals that were geometrically similar should move at the same speed regardless of their body size. However, due to the variability in phylogenetic differences amongst species as well as those effects imposed by changes in body size, locomotor performance has been shown to be highly varied in numerous animals (Schmidt-Nielsen, 1984). Marsh (1994) proposed an alternative theory concerning the scaling of jumping performance in anuran frogs. He considered our existing knowledge of muscle contractile properties and allometry in frogs and proposed that jumping distance would scale as $M_b^{0.200}$, rather than being mass independent. The difference in these two models concerns the scaling of intrinsic shortening velocity, which from empirical evidence seems to scale as $M_b^{-0.100}$, closer to the value predicted by McMahon's model ($M_b^{-0.125}$) than to Hill's ($M_b^{-0.333}$). Numerous studies have investigated jumping in frogs, and the available data seem to more closely resemble the model put forward by Marsh (1994) over that of Hill (1950). Interspecifically, jumping distance scales with an average mass exponent of 0.2 (Emerson, 1978; Zug and Altig, 1978), whereas intraspecific studies have produced scaling exponents of between 0.18 and 0.36 (Emerson, 1978; Miller et al., 1993; Rand and Rand, 1966).

The data collected by Marsh (1994) on anuran frog jumping reveals that maximum muscle mass-specific power scales independently with body mass and gives a scaling exponent of 0, suggesting that all animals have the same amount of relative power available regardless of body size. Later work however revealed the relationship between muscle power and jumping power to be complex, with a large discrepancy between the power available from the hind limb muscles and that required during take-off (Peplowski and Marsh, 1997). Subsequent research into the scaling of mass specific jumping power in the striped marsh frog found jumping power to decrease with increased body size, scaling as $M_b^{-0.460}$, whilst jumping distance was found to be independent of body size (Wilson et al., 2000).

1.2.3 The scaling of frequency and mass-specific work

The speed at which muscles contract determines their absolute speed of movement, and as such has a strong influence on organismal performance. As animals get larger the speed at which their muscles contracts generally slows, resulting in smaller animals moving more quickly in relative terms than larger animals. This decrease in frequency seems to work as a means of maintaining muscle performance through ontogeny, as the cycle frequency for maximum output decreases with increasing body size (Altringham and Johnston, 1990). Hill (1950) predicts that frequency should scale inversely with body length as $M_{\mathrm{b}}^{-0.333}$. Experimental studies however have found this not to be the case. In the works of Marsh (1988) frequency scaled as $M_{\mathrm{b}}^{-0.200}$, additionally, in studies on birds in the Phasianidae (Askew et al., 2001) frequency scaled as $M_{\mathrm{b}}^{-0.247}$, and as $M_{\mathrm{m}}^{-0.290}$ in birds in the Corvidae (Jackson and Dial, 2011), whilst in the *Dipsosaurus* stride frequency scaled as $M_{\mathrm{b}}^{-0.238}$ (Johnson et al., 1993).

The assumption that both stress and strain are constant led to the conclusion that muscle mass-specific work was also constant and independent of body mass. However, research on escape performance in Corvidae found muscle strain to increase with increasing muscle size, scaling as $M_{\mathrm{m}}^{0.120}$, but work was still found to be independent of muscle mass (Jackson and Dial, 2011). Additionally, analysis of flight performance in bees and birds found muscle mass-specific power output to be independent of body mass (Askew and Marsh, 2001; Tobalske and Dial, 2000). As such work output was found to scale inversely with wing beat frequency, scaling as $M_{\mathrm{b}}^{0.336}$.

Constancy of stress assumes the same relative proportion of contractile to non-contractile elements in muscle fibres during growth. This however has been shown not to always be true. Research into the scaling properties of the myotomal muscles in Atlantic cod found peak stress to scale as $M_b^{0.080}$ (Anderson and Johnston, 1992), it was demonstrated that mitochondria make up around 20% of the fast muscle in small fish, decreasing to around 1-2% in larger fish, thus allowing for the amount of myofibrils available for contraction to increase with body mass, which may explain the slight positive scaling relationship for stress found here.

Hill's (1950) early works were based on the isotonic force-velocity relationship of muscle. Isotonic contractions give a good insight into the intrinsic contractile properties of muscles and are useful for comparisons across preparations. In reality however, muscles very rarely operate isotonically *in vivo*. During contraction *in vivo*, muscles will generally be working against a constantly changing load, due to the interaction between the morphological structures of the organism, the physiological properties of the muscle and the environment in which they are operating (Marsh, 1999). In addition to these limitations, the lengthening phase of the muscle contraction cycle is often neglected, where work is required in order to re-stretch the muscle. As such, these measurements do not accurately reflect the conditions in which the muscles are operating under *in vivo*.

1.2.4 Scaling of maximum power output determined using the work loop technique

During locomotion muscles tend to go through cyclical movements due to the movement of the limb in relation to the associated muscle. The work loop technique (Josephson, 1985) attempts to replicate that action by submitting muscles to sinusoidal length changes, thus simulating the length changes that a muscle would undergo whilst operating *in vivo*. During these experiments power output is maximised by optimizing strain amplitude, frequency and stimulation pattern. The output of a work loop produces a plot of force against the length change of the muscle, resulting in a plot which forms a loop, the area of which is the net work produced by that muscle during one cyclical contraction. Johnson et al. (1993) used this technique to study the scaling of muscle performance in the iliofibularis muscle of the lizard *Dipsosaurus dorsalis.* It was found that maximum power output was independent of body mass. The optimum frequency for net maximum power output decreased with increasing body mass, resulting in an increase in muscle mass specific work with increasing body mass, scaling as $M_b^{0.238}$.

1.2.5 Whole animal approaches to the scaling of maximum muscle power output

In certain locomotor systems it seems reasonable to assume that all of the power required for a particular behaviour is assigned to one particular muscle or group of muscles. This is indeed the case when looking at escape flights in ground dwelling birds, where the major muscular effort is directed to producing mechanical power via the large pectoralis muscles. The power output of several birds within the family Phasianidae during take-off was quantified through aerodynamic analysis of high-speed video recordings (Askew et al., 2001; Tobalske and Dial, 2000). Power during short maximal burst performance was shown not to scale with body mass, although there was a tendency for power to decrease in the largest species, $\alpha\ M_b^{-0.140}$. The scaling of muscle power output during burst escape flights in Corvidae has been investigated using sonomicrometry and force gauges, a slight negative scaling relationship between muscle mass specific power output and muscle size was found, scaling as $M_m^{-0.18}$ (Jackson and Dial, 2011).

Hill's predictions of the scaling of muscle performance were based on assumptions of constancy of stress and strain, leading to the conclusion that work should be independent of body mass and that mass-specific power should scale inversely with increased body size. However, there is a growing body of evidence to suggest that in some locomotor systems, muscle mass-specific power output does not change with body mass. Variations in stress due to differences in muscle fibre composition and decreasing strain as animals increase in mass may explain some of these deviations from Hill's predictions. More research into size-related differences in animal performance will likely help answer the questions of why these discrepancies seem to exist.

1.3 Aquatic Locomotion

In order to propel themselves through water, aquatic organisms must impart momentum to the fluid in which they are in in order to produce thrust. This thrust force overcomes the drag forces acting on the organism, allowing the organism to move. Drag represents the rate at which momentum is lost to the surrounding fluid. In swimming animals drag has two main components. The first of these is friction drag, which in swimming animals occurs due to the viscosity of the fluid interacting the surface of the organism. The second of these forces is pressure drag, which occurs due to pressure differences that arise across the surface of an organism as it moves and interacts with the surrounding fluid. Analysing movement within a fluid is complicated due the fact that forces applied to the fluid cause the fluid itself to move. In order to better understand the fluid dynamics of underwater propulsive systems, several factors need to be considered and quantified.

Several locomotor strategies exist amongst organisms that travel within a fluid. The smallest of these are the microorganisms such the ciliates and the flagellates. Ciliates travel via the beating of cilia that line their bodies, whilst flagellates have a rotating tail driven by a molecular motor. Fish and marine mammals swim by undulating their bodies or oscillating their fins. Amongst invertebrates, numerous methods of travel exist. Shrimp swim by paddling their legs and daphnia swim by beating their antennae. Some molluscs, such as sea slugs, swim by flapping fin like structures, whilst scallops and cephalopods employ jet propulsion. As animals swim they create a wake in the water, these wakes vary in structure and size and differ from species to species. A key feature of swimming animal wakes is the production of vortex rings. These are spinning masses of toroidal fluid and have been identified in the wakes of numerous swimming animals (Bartol et al., 2008; Dabiri et al., 2005; Gemmell et al., 2014; Sutherland and Madin, 2010). They can vary in size, shape, velocity and vorticity, with each of these variables having an impact on the hydrodynamic efficiency with which a species swims.

1.3.1 Visualising the flow: particle image velocimetry

In order to better understand the hydrodynamic performance of organisms as they swim through a fluid, it is necessary to be able to visualise the flow of the fluid and for it to be quantified. This is made possible through a technique known as particle image velocimetry (PIV). This method involves seeding the water with tracer particles that will faithfully follow the flow dynamics of the liquid, these particles are then illuminated using a laser and the particles traced using a high-speed camera.

PIV works on the premise of comparing two images, and tracking the particle displacement between them. A pulsed laser is typically used to illuminate the particles, allowing for the easy control of pulse frequency and duration to gather individual images in which the particles appear frozen in time. Alternatively a continuous laser can be used, with the capture rate of the camera being used to control the time difference between images.

Image pairs are compared to determine the displacement of particles between the two frames. The images are divided into small interrogation windows, generally around 32 x 32 pixels, and displacement of the particles is measured using a cross correlation technique across the image pairs in order to find the mean displacement that gives the maximum correlation. A Guassian or similar function is then fitted to the tallest correlation, giving an estimate of the mean particle displacement of the particles within the interrogation window.

Numerous tracer particles have been used in liquid based PIV systems, with the important attributes of the particle being that it is large enough to scatter light, but small to follow the flow of the fluid accurately (Melling, 1997). Particles used in liquid based PIV systems are generally between 5-50 µm in diameter, and range from conifer pollen (Westergaard and Buchhave, 1993) to glass microspheres (Graham and Soria, 1994).

1.3.2 Hydrodynamic efficiency

Swimming animals produce thrust by driving water backwards, forming a wake; the thrust is equal to the rate at which momentum is added to the wake. During locomotion some of the energy that is imparted to the wake is useful and results in a force that propels the animal, but some of the energy is lost due to non-uniform wake velocities. This can be summarised using the Froude efficiency (η_F), which considers the power that an organism has to exert to overcome the drag on its body, as well as the additional power that is imparted as kinetic energy to the water that is being driven backwards as the organism is being propelled. This efficiency is the ratio of useful power to the total power input and can be defined as:

$$\eta_{\mathrm{F}}=\frac{v}{v+\frac{1}{2}\,v_{\mathrm{wake}}} \qquad [1.2]$$

where v is the velocity of the swimming animal and v_{wake} is the acceleration of the mass of water being driven backwards in unit time from rest to velocity. From this equation, it is shown that for efficient propulsion, v_{wake} should be made as low as possible, i.e. it is more beneficial to accelerate a large mass of water to low velocity than a smaller mass of water to a high velocity. The equation for Froude efficiency can be adapted to better suit specific aquatic propulsion systems. Alexander (2003) developed a version of the Froude efficiency equation that could be applied to jet propelling animals as:

$$\eta_{\mathrm{p}}=\frac{2\bar{U}\bar{u}_{\mathrm{j}}}{(\bar{U}+\bar{u}_{\mathrm{j}})^{2}} \qquad [1.3]$$

Where $\bar{U}$ is time averaged body velocity and $\bar{u}_j$ is the time averaged fluid velocity of the jet. This equation provides information on the basic hydrodynamic efficiency of animals that swim via jet propulsion and can be used to compare swimming mechanics across different species.

1.3.3 Jets as a means of propulsion

Jet propulsion is found in numerous animals, including squid (Anderson and Demont, 2000), jellyfish (Dabiri et al., 2005) and scallops (Cheng and DeMont, 1996b), and all do so by compressing a cavity to produce a pressure difference between the ambient water and the cavity that results in fluid flow out of the cavity. The flow of fluid during jet propulsion generally happens in one of two ways. Water can be both drawn in and expelled at the rear of the organism, this may involve the same orifice such as jellyfish, or may be portioned into separate refill and expelling orifices as seen in cephalopods such as squids and cuttlefish. Alternatively water may be drawn in from the front of the animal and ejected at the rear, as seen in salps and scallops. The mechanics of refilling and expelling water in this way leads to periods of acceleration during the ejection of water and deceleration during the refill phase, resulting in fluctuations in velocity as a jetting organism moves through the fluid. Jet propulsion has often been considered a poorly efficient means of aquatic locomotion, particular when compared to undulatory swimming (O'Dor, 1982). Recently however, this notion has been challenged through research with both mechanically generated jets and exploratory studies into the efficiency by which jet propelled organisms travel (Bartol et al., 2008; Gemmell et al., 2014; Krueger and Gharib, 2003). A key aspect of the benefits of swimming via jet propulsion is centred on the formation of vortex rings during the production of the jet. The formation of vortex rings has been suggested as a means of increasing swimming efficiency in animals. The potential for vortex rings to improve swimming performance is due to the increase in entrainment that is created in the wake during locomotion. The circulation of the vortex ring causes additional water to be entrained from the surrounding fluid, increasing the amount of fluid that is driven backwards in the wake of the jet (Krueger and Gharib, 2003). Thrust is the product of the velocity of water expelled backwards and the water mass (per unit time), so any additional ambient fluid that is accelerated through associations with vortex rings has the potential to increase the thrust being produced. Recent research suggests that the pulsed nature of jet propulsion allows for the manipulation of parameters such as nozzle exit diameter and jet velocity profile that can result in an optimum in vortex ring production, resulting in a form of jet propulsion with increased thrust and hydrodynamic efficiency (Krueger and Gharib, 2003; Dabiri et al., 2006). Mechanically generated jets using a piston cylinder mechanism are most often used in the study of the vortex rings produced through jet propulsion. The production of a vortex rings comes about through the formation of a boundary layer of vorticity on the inner cylinder wall as the piston moves inside the cylinder. Upon reaching the end of the cylinder, the boundary layer separates from the mechanism and rolls up into a vortex ring that propagates downstream and away from the generator. Vortex rings formed in this way can be characterised by the length of the column of fluid that is being ejected, *L*, and the diameter of the orifice of the cylinder, *D*.

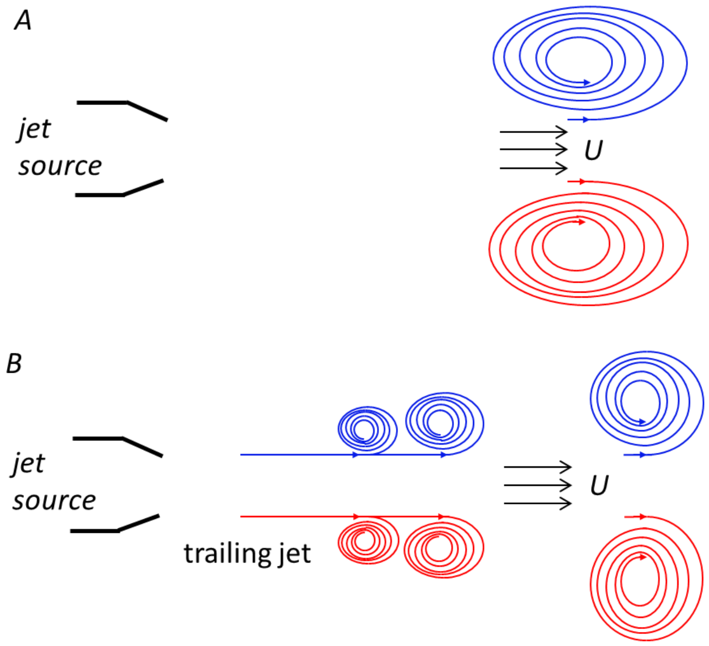

Figure 1.3. Cross sectional schematic of two jet forms. An isolated vortex ring (A) and a jet in which the leading edge has pinched off, with the remaining fluid forming a trailing jet (B). Jet flow is from left to right. Red and blue regions denote clockwise and counter clockwise rotation, respectively. Adapted from Dabiri and Gharib (2005).

1.3.4 Optimal Vortex Formation

Much of the early work on vortex ring formation focussed on the evolution of vortex ring size and circulation as it moves away from the vortex generator (Didden, 1979; Maxworthy, 1977), in jets with low *L*/*D* ratios (less than around 4). Gharib et al. (1998) was the first to explore vortex ring formation at higher *L*/*D* ratios, representing the vortex formation process for longer periods of time as *L* increased in relation to *D*. Gharib et al. were able to identify a limit in the maximum growth of vortex rings produced via the piston cylinder, beyond which the vortex ring can no longer increase in size and instead 'pinches off' from the main jet (fig. 1.3). This phenomenon was attributed to the fact that there is a limit to the amount of energy that may enter a vortex ring during jetting, when this limit is reached the vortex ring ceases to grow in strength and instead pinches off from the jet, any remaining fluid from the jet is then ejected as a trailing jet. The ratio of *L*/*D* at which of vortex ring can no longer accept vorticity flux from the vortex generator has come to be known as the 'formation number', *F*, and represents a dimensionless time scale for the formation of isolated vortex rings.

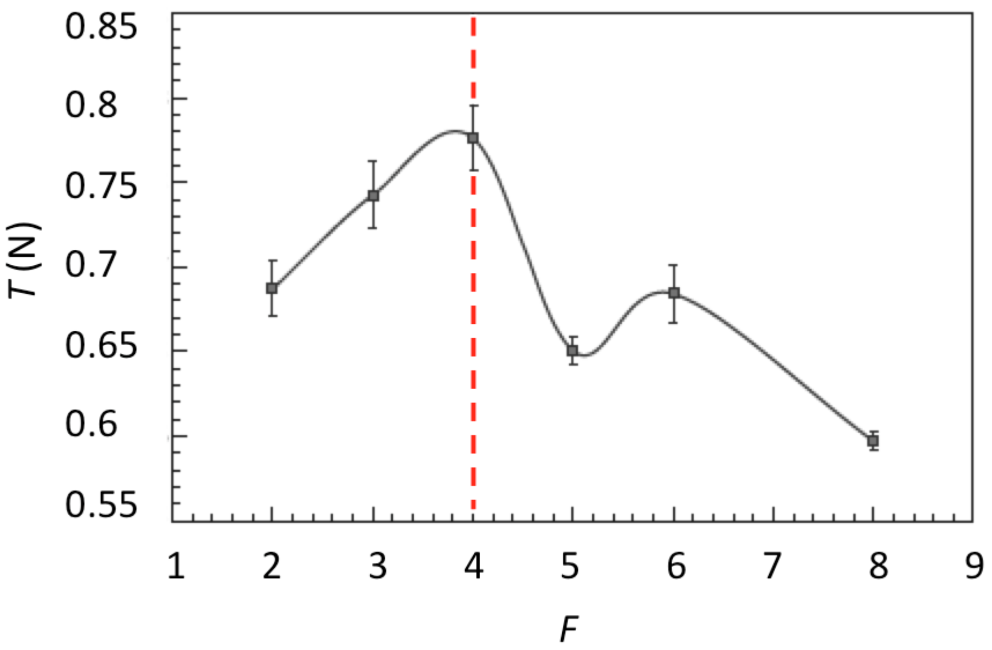

Figure 1.4. Normalised time-averaged thrust (*T*) per pulse as a function of formation number (*F*). Figure adapted from Krueger and Gharib (2003).

Krueger (2001) studied how vortex ring properties scale with vortex size using mechanically generated jets. He found that time-averaged thrust per jet pulse reached its maximum just before the vortex ring limiting formation number was reached (fig. 1.4). Further work demonstrated that the impulses created from isolated vortex rings were significantly larger than those that would be expected from jet velocity alone and proportionally larger than jets which have pinched off and formed a trailing jet (Krueger and Gharib, 2003). Through these experiments Krueger and Gharib showed that it might be possible to optimize the efficiency of momentum transport by maximising the size of the vortex rings formed during jetting.

1.3.5 Mechanically Generated Jet Pulses

The potential for an optimum in pulsed averaged thrust in jet-propelled system is intriguing. It begs the question of whether the formation number of vortex ring formation is a universal principle in jet propelling systems or can be manipulated?

Numerical simulations of a piston-cylinder vortex generator have demonstrated that formation number could be reduced by up 75% or increased by 35% through the manipulation of the fluid velocity out of the cylinder (Rosenfeld et al., 1998). It has also been suggested that pinch off could be delayed by accelerating the trailing jet relative to the leading vortex ring, resulting in the trailing jet being entrained within the leading vortex ring and increasing its energy (Mohseni et al., 2001).

Pinch off was delayed by around 10% by creating vortex rings with the piston cylinder mechanism immersed within a uniform bulk counterflow (Dabiri and Gharib, 2004a). Krueger et al. (2006) experimented with the opposite effect, with the piston cylinder immersed in a bulk uniform co-flow, this resulted in a reduction in formation number, with the onset of pinch off occurring also immediately following the formation of the vortex ring, at formation numbers of around 0.5.

Temporal manipulation of the orifice diameter of the cylinder during the ejection of fluid during jet production resulted in isolated vortex rings being produced at formation numbers of around 8 (Dabiri and Gharib, 2005).

1.4 Vortex rings in Biological Propulsion Systems

Numerous studies have characterised the structure of the vortices produced by swimming animals in water and the implications that this has on their movement (Bartol et al., 2009a; Dabiri et al., 2005; Sutherland and Madin, 2010). Much research has been done on vortex rings structure, specifically how species can utilise their size and shape to increase the efficiency of their locomotion.

1.4.1 Jet propulsion in salps and jellyfish

Organisms such as salps and jellyfish pump water from their body cavities via a rhythmic muscular action. In salps water intake is achieved at the front of their bodies through pressure reduction in the body cavity, this is followed by muscular expulsion of water as a jet from the back of the organism. Work on jet propulsion in several species of salp found via PIV experiments that different species produced various vortex structures during forward motion (Sutherland and Madin, 2010). It was demonstrated that species that produced discrete vortex rings were more efficient than those that produced trailing jets, with the slow swimming species *Pegea confoederata* producing the highest propulsive efficiency ($\eta_F = 0.67$) of the species tested. Dabiri et al. (2006) identified a species of jellyfish as producing isolated vortex rings. They calculated that isolated ring formation persisted up to formation numbers of around 8, whilst pinch off did not occur at all. They attributed this to the kinematic effect of the velum of the jellyfish, which acts to reduce the orifice area during the jetting phase of the swim cycle. The motion resulted in shear layer kinematics that delayed the pinch off process, increasing the formation number to at least 8. This result is consistent with mechanically generated jet pulses (Dabiri and Gharib, 2005), in which time-dependent shear layer kinematics were investigated to ascertain their effect on the vortex ring formation process.

1.4.2 Jet propulsion in squid

In contrast to salps that have developed a means of pulsed jet propulsion that allows them to swim at a steady rate, many other species use a jet propulsion system in order to achieve short burst of rapid acceleration followed by a period of gliding. Primary examples of species that propel themselves in this way are the cephalopods, a group that includes the octopus, squid and nautilus (Wells and O'Dor, 1991).

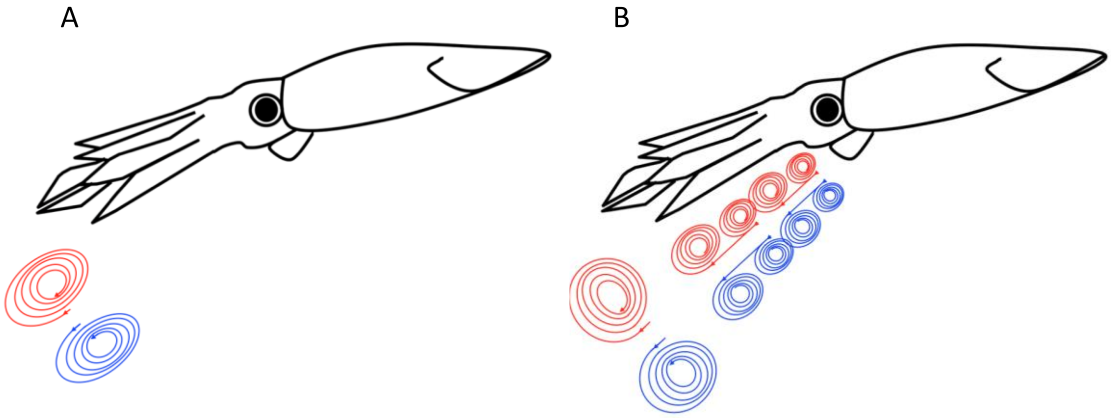

Figure 1.5. Squid shown are producing both isolated vortex rings i.e. Jet Mode 1 (A) and leading vortex rings that pinch off i.e. Jet Mode 2 (B). Arrow represents swimming direction. Blue regions denote clockwise rotation, red regions denote anticlockwise rotation. Figure adapted from Bartol et al. (2009).

With the advantages that the formation of vortex rings brings, it might be assumed that all species that use jet propulsion as a means of locomotion would exploit them. This however, does not seem to be the case. Studies into the wakes of jetting adult long finned brief squid *Doryteus pealeii* using PIV revealed no discernible formation of vortex rings, either individually or as leading structures in elongated jets (Anderson and Grosenbaugh, 2005). It was shown that these particular squid were instead emitting steady prolonged jets of fluid that displayed an elongated core of high-speed flow, resulting in a wake structure that might be more similar to those seen in a steady jet. Bartol et al. (2009a) did similar experiments on *D. paeleii*, but instead focused on the early life stages of the species, i.e. paralarvae. These studies revealed that at this stage in life the squid were producing a range of jet structures, from the formation of full vortex rings to the more elongated vortex structures commonly seen in adults. These results suggest that the structures of the wakes that are being produced by this particular squid species change significantly throughout their life. Additionally, there is evidence of similar vortex ring structures being formed by the paralarvae of the Atlantic brief squid *Lolligincula brevis*. The initial data were qualitative as it was collected via dye injection and observations only (Bartol et al., 2001). Further research in to the vortex structures produced by *L. brevis* enabled them to be quantitatively analysed using PIV techniques and they too revealed that a range of jet structures were produced, as had been seen in the paralarvae of *D. pealeii* (Bartol et al., 2008). Squid were swam at a variety of different ages, covering their entire life history cycle, allowing for a comprehensive set of data to be gathered on the dynamics of jet flow and wake structure during ontogeny in *L. brevis*. They concluded that the range of jet structures and flows observed in *L. brevis* could be classified into 2 jet modes. The first, jet mode 1, describes the process whereby the ejected fluid rolls up into individual, isolated vortex rings. The second, jet mode 2, describes a long trailing jet, in which a leading vortex ring may form before being pinched off from the jet (fig. 1.5). It was found that jet mode 2 was the most frequently used, producing greater time averaged thrust and lift forces. Jet mode 1 on the other hand was shown to have higher propulsive efficiency, with a Froude efficiency (η_F) calculated to be up to 0.81 in some individuals, which is a similar value to those that have previously been demonstrated in undulatory swimming fish (Webb, 1971).

Whilst swimming using jet mode 1, it was shown that *L. brevis* was able to produce jets near the value of *F* for optimum pulse-average thrust generation that were previously described (Krueger and Gharib, 2003), suggesting that *L. brevis* could indeed take advantage of this thrust augmentation benefit, by producing short jets of high efficiency thrust rather than less efficient longer jet pulses.

Evolution has likely acted on the physiology and morphology of animal locomotor systems to be as efficient as possible. Studying jet propulsion in marine invertebrates will give us an insight into their unique locomotor strategies and give us clues as to how the way they move might affect their life history. The potential for optimal vortex formation has been identified in a number of biological systems, however the effect that this can have on overall animal performance has only been measured definitively in a few cases. A better understanding of optimal vortex formation within biological systems may give engineers inspiration in the design of more efficient aquatic propulsion technologies.

1.5 Summary

This thesis explores both the muscle mechanics and hydrodynamics of marine invertebrates during jet propulsion swimming. The scaling of whole animal muscle mass-specific power was examined (Chapter 2). The scaling of several mechanical properties that influence muscle power output was quantified, including stress, strain, duty cycle and cycle frequency. The physiological properties that influence the scaling of cycle frequency were also studied *in vitro*, several intrinsic muscle properties that relate to the rate at which a muscle contracts were measured and their scaling relationships related back to *in vivo* muscle performance (Chapter 3).

The hydrodynamics of three invertebrates that swim via jet propulsion were quantified (Chapters 4,5,6). Jet structures were described for each species and the impact they had on animal swimming performance studied. The mechanics of vortex ring formation were examined in each species and the potential for biometic design explored.

Chapter 2 investigates how changes in body mass affect the scaling of muscle mass-specific power output. Theoretical models predict muscle mass-specific power-output will decrease with increasing body mass, scaling as $M_b^{-0.333}$ according to Hill's classic geometric similarity model. However, empirical evidence suggests that muscle power output scales negatively with a scaling exponent less than this (Altshuler et al., 2010; Jackson and Dial, 2011), or that muscle mass-specific power output should be independent of body size (Askew et al., 2001). Much of this previous work has been based on *in vitro* measurements of isolated muscle performance or power calculated from aerodynamic analysis. In this chapter muscle power output is measured *in vivo* during escape swimming in scallops covering a wide range of body masses, with the aim of quantifying how muscle power output, and how the underlying factors influencing power, scale with body mass.

Chapter 3 looks to characterise the contractile properties of the scallop adductor muscle and link these to the scaling of *in vivo* muscle performance. The intrinsic properties of muscles can have major influences of how a muscle functions *in vivo*, however, the scaling of these properties has only been partially explored (Marsh, 1990; Marsh, 1994). This chapter aims to link the contractile characteristics to the scaling of *in vivo* muscle power, assessing the extent to which the scaling of the intrinsic properties of the muscle influence muscle performance.

In chapter 4 swimming performance and wake structure is analysed during jet propulsion swimming in king scallops. Aquatic locomotion *via* pulsed jet propulsion is thought to bring benefits to thrust production through the production of isolated vortex rings (Dabiri et al., 2006; Krueger, 2001). It is thought that animals that swim using jet propulsion may have evolved to take advantage of these potential benefits. This chapter looks to characterise the wake structure of king scallops to assess whether the vortices they produce during swimming exhibit any thrust or efficiency augmentation. The hydrodynamic work that the scallop produces will be compared to the muscular work from the previous chapters *in vivo* measurements in order to quantify the efficiency of this part of the locomotor system.

Chapter 5 investigates locomotor performance during jet propulsion swimming in *Nautilus*. *Nautilus* are able to swim both posterior first and anterior first due to a flexible funnel, which can direct water in numerous directions. Previous work has demonstrated that at low swimming speeds, *Nautilus* have a lower cost of transport than squid and fish (O'Dor et al., 1990). However, the hydrodynamic reasons for this have not been explored. In this chapter the swimming efficiency of *Nautilus* is measured in order to determine how important hydrodynamics are to achieve this low cost of transport, and the effect of swimming orientation quantified.

In chapter 6 swimming kinematics and wake structure in a species of Rhizostomeae jellyfish is measured. Jellyfish are considered the most economical travellers amongst all animals (Gemmell et al., 2013), their flexible bodies have been shown to be able to manipulate vortex rings in such a way to enhance their forward propulsion. Rhizostomeae jellyfish differ from species previously studied, in that they have large oral feeding arms at the centre of their bell. The impact of this unique body morphology on the wake structure and swimming kinematics of the jellyfish is explored.

Chapter 2

The scaling of muscle mass specific muscle power output during escape swimming in scallops

2.1 Abstract

The scaling of muscle power output is crucial to understanding size-related differences in animal locomotion. It has been hypothesised that muscle mass-specific power output should scale negatively with body mass according to either geometric or elastic similarity (as $M_b^{-0.333}$ or $M_b^{-0.250}$, respectively). To test these hypotheses, muscle mass-specific power output was determined *in vivo* during escape swimming in scallops covering a 96-fold range in body mass. *In vivo* power output was quantified by measuring the pressure and inter-valve volume change during swimming (power = pressure x flow rate). Peak and average muscle mass-specific power was found to decrease with increasing body mass, scaling as $\sim M_b^{-0.220}$ and $\sim M_b^{-0.227}$. Work output and mean stress difference were found to be independent of body mass. Contraction frequency was the primary determinant on the scaling of muscle power, but scaled as $\sim M_b^{-0.124}$, suggesting that trends in strain and proportion of the cycle spent shortening to decrease with increasing body mass also influence the scaling of muscle power output in scallops. Large confidence intervals make definitive conclusions about how power output scales with body mass difficult, but the scaling of contraction frequency is consistent with scaling in accordance to elastic rather than geometric similarity.

2.2 Introduction

The ability of an animal to move is often essential for its survival, for example, finding food, a mate or escaping a predator. There are two aspects of locomotory performance that are under selective pressure. The first of these is muscle mechanical performance, which dictates locomotor performance in terms of imparting energy to the animal’s centre of mass. The second is metabolic energy expenditure, which determines how long a given fuel supply will last, and how much energy is left over that an animal can use for other behaviours, such as reproduction and growth. There may be a trade-off between muscle mechanical performance and endurance as adaptations that favour sustained locomotion (such as increased mitochondrial volume) may have a detrimental effect on muscle mechanical power. It is the trade-off between these different selective pressures that has shaped the design of locomotory systems. As animals grow the performance of the locomotor muscles differs, with the available power from the muscles ultimately setting the limit on the activities that an animal is capable of. Understanding the limitations bought about by animal size is crucial to understanding size-related differences in animal performance (Weis-Fogh and Alexander, 1977).

The scaling of muscle mass-specific power output (Π^*) is crucial to understanding size-related differences in animal locomotion. If animals are geometrically similar, muscle mass-specific power is predicted to scale in accordance to muscle operating frequency as $M_b^{-1/3}$ (Hill, 1950; Pennycuick and Rezende, 1984). This relationship is built on the underlying assumption that muscle stress and strain are constant; that a muscles’ operating frequency is proportional to its maximum shortening velocity; and that muscles operate at the same relative shortening velocity and generate the same relative stress. However, an alternate model argues that animals should scale with elastic similarity rather than geometric similarity, in order to keep elastic deformations constant under similar loads. According to elastic similarity, a muscles’ operating frequency is predicted to scale as $M_b^{-1/8}$, whilst angular excursion of limbs is predicted to be greater in smaller animals, yielding the prediction that muscle mass-specific power should scale in proportion to body mass as $M_b^{-1/4}$.

One approach to quantifying the scaling of maximum muscle mass-specific power output (Π^*) in animals is to study whole organism performance. In order for this approach to be appropriate, it is assumed the power required for the movement of the animal can be assigned to a particular group of muscles that are generating maximal power. Escape responses are such movements in which it can be assumed that the muscles are operating at or near to their maximum. Using a combination of wing kinematic measurements and aerodynamic analysis, Π^* was found to be independent of body mass within the family Phasianidae, although there was a tendency for Π^* to decrease in the largest species, with $\Pi^* \propto M_b^{-0.070}$ (Askew et al., 2001 using data published in Tobalske and Dial, 2000). Escape flights in Corvidae were analysed using strain gauges to measure force during take-off (Jackson and Dial, 2011), Π^* was found to decrease with increasing muscle mass (M_m), scaling as $M_m^{-0.180}$. Strain increased with body size whereas mean stress was found to be independent of body mass (Jackson and Dial, 2011) .

2.2.1 Scallops as a model

Scallops (family: Pectinidae) swim by jet propulsion, a mode of locomotion that has evolved as the animal's main defence against predators (Stephens and Boyle, 1978). Jet propulsion swimming is accomplished through a succession of alternate opening (abduction) and closing (adduction) of the valves. Valve adduction compresses the mantle cavity, expelling a jet of water through two vents located adjacent to the hinge, propelling the animal through the water (Olson and Marsh, 1993). Contraction of the large adductor muscle provides the mechanical power required for valve adduction, the power is used primarily to impart momentum to the water and provide propulsion to overcome hydrodynamic drag via the jets; however, a small amount of energy is used to compress the hinge ligament (Trueman, 1953) that is subsequently released to abduct the valves.

The simplicity of scallop locomotion makes it an ideal system in which to gain further insights into the scaling of the physiological and mechanical performance parameters that would be more challenging to tease out in more complex locomotory systems. The large adductor muscle of the scallop is parallel fibred and cross striated, and shares many functional and structural similarities to vertebrate skeletal muscle (Millman, 1967). As swimming in scallops is an escape response, it is reasonable to assume that the muscles are generating their maximal power output.

The adductor muscle produces all of the power required to produce movement in scallops, meaning that whole animal performance can be quantified. Marsh et al. (1992) developed an approach that allowed muscle mechanical performance to be quantified *in vivo* during swimming. This was achieved through a set of measurements of the mechanical performance of the adductor muscle during jet propelled swimming. Two scallop species were used in their investigations, the Atlantic bay scallop, *Argopecten irradians* (mean body mass = 27.2 ± 4.0g) and the spiny scallop, *Chlamys hastate* (mean body mass = 17.0 ± 1.7g). They measured pressure within the mantle cavity during adduction as well as the rate of change in volume within the scallop during jetting, thus allowing them to quantify instantaneous power during locomotion (Power output = pressure x flow rate). Π^* was ~160 W kg^{-1} in *A. irradians* and ~223 W kg^{-1}, in *C. hastate*. Average power output $\left(\overline{\Pi}^*\right)$ was ~28 W kg^{-1} in *A. irradians* and ~53 W kg^{-1}, in *C. hastate*. Although the difference in body mass is only around 63% across the two species, the results indicate that their may be a size related difference in Π^* amongst scallops.

In these experiments, escape swimming in three species of scallops was studied, bay scallops (*Argopecten irradians*), queen scallops (*Aequipecten opercularis*) and king scallops (*Pecten maximus*) as a means of determining how *in vivo* muscle power output scaled intra-specifically. Scallops can increase in size 100- fold throughout ontogeny, whilst remaining morphologically similar, allowing scaling relationships to be accurately quantified within a species and related back to theoretical models. Using the technique developed by Marsh et al. (1992), muscle mass-specific power output was determined *in vivo* during escape swimming in scallops that covered of range of body masses by measuring the pressure pulses and the change in inter-valve volume during swimming. It was hypothesized that muscle mass-specific power output would scale in accordance to geometric similarity (Hill, 1950), in which muscle power output is predicted to scale with cycle frequency, $\alpha\ M_b^{-0.333}$.

2.3 Materials and methods

2.3.1 Animals

Queen scallops (*Argopecten opercularis*, Linnaeus 1758) (body mass 3.84 – 38.11g, *n* = 18) were collected via otter trawl in the Irish Sea in October 2013. The animals were held in tanks of recirculating seawater at Bangor for a week before being transported to the University of Leeds, UK, where they were maintained in artificial seawater (Instant Ocean, Aquarium Systems, Mentor, OH) at a temperature of 12^{o}C and a salinity of 34ppt. Hand dived king scallops (*Pecten maximus*, Linnaeus 1758) (body mass 3.9 – 373.45g, *n* = 22) were collected from Loch Fyne, Scotland (between August 2008 and July 2009) and from The Ethical Shellfish Company, Mull, Scotland in November 2015; they were transported to the University of Leeds, UK, where they were maintained in artificial seawater (Instant Ocean, Aquarium Systems, Mentor, OH) at a temperature of 10^{o}C and a salinity of 34ppt. Bay scallops (*Argopecten irradians*, Lamarck 1819) (body mass 5.54 – 80.62g, *n* = 23) were obtained from The Marine Resources Center of the Marine Biological Laboratory, Woods Hole, MA, USA from Nantucket Sound off the southern coast of Cape Cod from the Atlantic Ocean in July 2015, before being transported to Wellesley College, USA where they were kept in artificial seawater at 15 ^{o}C and a salinity of 34ppt. The scallops were housed in conditions that corresponded to the conditions at the time and in the locations from which the scallops were collected. Scallops were allowed to acclimatise to the laboratory conditions for at 2 days before experiments took place. The temperature at which swimming experiments were performed differed between the species due to our efforts to match the temperature in our experiments with that of the environment in which the animals were collected. This will not affect intra-specific scaling relationships; inter-specific scaling relationships may be affected by temperature effects on muscle performance and were not considered.

2.3.2 Measurement of inter-mantle pressure and volume changes

Pressure inside the mantle cavity was measured using a fibre optic pressure sensor (FOBPS, World Precision Instruments, Inc, Sarasota, USA) inserted into the mantle cavity through a 1mm hole drilled in the left valve using a Dremel (Dremel Multipro cutting tool, Dremel, Racine, Wisconsin). Sonomicrometry crystals (1 or 2 mm diameter, Sonometrics Corporation, London, Ontario, Canada) were attached to the valves overlying two 1 or 2mm holes (depending on the size of the scallop and crystal used) drilled in each valve next to the ventral edge of the adductor muscle. The pressure sensor and sonomicrometry crystals were secured to the shells using a combination of modelling clay and cyanoacrylate glue (Vetbond; 3M, St. Paul, MN and Gorilla Glue, the Gorilla Glue Co., Cincinnati, OH). The holes in the shell were drilled in chilled shallow seawater at least 24 hours before the experiments. The sonomicrometry crystals and pressure sensor were secured to the shell while the animal was out of the water due to the need for a dry shell for better adherence of the clay; this process took approximately 2 minutes. Scallops were allowed at least one hour to recover from fixing the sonomicrometry crystals and pressure sensor, until the animals had re-opened their valves and extended their tentacles.

2.3.3 Escape swimming

Instrumented swims were performed in tanks in which the water temperature and salinity were identical to that in the holding tanks – i.e. salinity of 34ppt and temperatures of 15°C for the bay scallops, 12°C for the queen scallops and 10°C for the king scallops. Escape swimming was elicited by touching the sensory tentacles near their dorsal edge with a common predator, which was either a common starfish *(Asterias rubens*, *Linnaeus* 1758), a dog whelk (*Nucella lapillus*, *Linnaeus* 1758) or an oyster drill (*Urosalpinx cinerea*, *Say* 1822). Swimming was induced between 2 and 4 times, scallops were allowed a time of approximately 5 minutes between each swim in order to return to a steady state following stimulation. The movements of the valves during swimming were recorded at a sample frequency of 677.5 Hz using the acquisition software SonoLab (Sonometrics Corporation, London, Ontario, Canada) *via* a data acquisition system (PowerLab, ADInstruments, Colorado Springs, CO, USA) and the acquisition software Chart (Version 7, ADInstruments, Colorado Springs, CO, USA). The pressure within the mantle cavity was simultaneously measured with the valve movements using a fibre optic pressure sensor system (FOBPS, World Precision Instruments Inc., Sarasota, USA) at a frequency of 10 kHz *via* a PowerLab (ADInstruments, Colorado Springs, CO, USA) and Chart (Version 7, ADInstruments, Colorado Springs, CO, USA). Following the swim animals were weighed and dissected and the blotted whole muscle mass recorded.

2.3.4 Mechanical power during swimming

The mechanical power output during swimming was calculated from the flow rate of water expelled through the jets during swimming and the mantle cavity pressure (Marsh et al., 1992).

At the end of the experiments, for each scallop, the relationship between the inter-valve distance, measured using sonomicrometry, and the angle of opening between the valves (β_{hi}), was determined.

$$\beta_{\mathrm{hi}} = 2 \sin\left(\frac{0.5L_{\mathrm{ve}}}{a}\right) \tag{2.1}$$

where L_{ve} is the distance between the valve edges at the sonomicrometry crystal location and a is the parallel distance from the hinge to the sonomicrometry crystal. L_{ve} is given by:

$$L_{\mathrm{ve}} = L_{\mathrm{v}} - L_{\mathrm{cl}} \tag{2.2}$$

Where L_{cl} is the closed length of the muscle taken from the sonomicrometry recording, and and L_{v} is the distance between the outer surfaces of the valves according to the sonomicrometry data. This relationship allowed the opening angle of the valves to be calculated from the sonomicrometry recording throughout the escape swims.

For each scallop, the total area of the left valve (A_v) and the co-ordinates of the centroid of the valve determined relative to the hinge (x_c, y_c) using ImageJ (ImageJ, Bethesda, Maryland, USA). The inter-valve volume (V_v) was calculated as:

$$V_v = 2\, A_v x_c \sin\left(\frac{\beta_{hi}}{2}\right) \tag{2.3}$$

The expellable water volume (V_{exp}) was calculated as the difference between the inter-valve volume (V_v) and the proportion of the inter-valve volume taken up by the volume of the adductor muscle (V_{iv}).

$$V_{exp} = V_V - V_{iv} \tag{2.4}$$

where, V_{iv} is given by:

$$V_{iv} = \frac{M_m L_{iv}}{\rho_M L_v} \tag{2.5}$$

where M_m is muscle mass, L_{iv} is inter-valve distance , ρ_M is muscle density [taken as 1060 kg m^{-3}; (Alexander, 1983)]. L_{iv} is given by:

$$L_{iv} = 2_a\, tan\frac{\beta_{hi}}{2} \tag{2.6}$$

The flow rate ($\dot{V}_{exp}$) of water into and out of the mantle cavity was determined by differentiating V_{exp} with respect to time (Igor Pro version 6.37, WaveMetrics Inc., Portland, OR, USA).

Muscle mass-specific swimming power (Π^*) was calculated as the product of instantaneous mantle cavity pressure (P^{o}) and flow rate ($\dot{V}_{\mathrm{exp}}$) expressed relative to adductor muscle mass (M_{m}):

$$\Pi^* = \frac{\dot{V}_{\mathrm{exp}} P^{\mathrm{o}}}{M_{\mathrm{m}}} \qquad [2.7]$$

Net muscle mass-specific swimming power ($\overline{\Pi}^*$) was calculated as Π^* averaged over 3 consecutive swimming cycles. A swimming cycle was defined as the period between the first drop in volume (beginning of the cycle) to the next drop in volume (end of the cycle).

Mean stress difference ($\bar{\sigma}$) was calculated as:

$$\bar{\sigma} = \frac{\overline{\Pi}^* 1060\, \tau}{f\epsilon \times 10 \times 50} \qquad [2.8]$$

where τ is the proportion of the cycle spent shortening, f is cycle frequency and ε is muscle strain.

In the bay scallops the amount of power stored and released by the hinge was able to be estimated from the velocity of shortening and the force required to compress the hinge (Marsh, unpublished results). Hinge power was calculated as

$$\overline{\Pi}^*_{\mathrm{hi}} = V_{\beta} M_{\mathrm{hi}} \qquad [2.9]$$

Where V_β is the angular velocity of the valves obtained from differentiating β_{hi} and M_{hi} is the hinge moment calculated as:

$$M_{hi} = \frac{B_1(1 - \beta_{hi}/\beta_0)}{A_1 - \beta_{hi}/\beta_0} \qquad [2.10]$$

where β_0 and A_1 are constants with the values 0.75 and 0.45 and B_1 is calculated from the allometric relationship of the dorso-ventral length of the valve as:

$$B_1 = (2.12)L_{dv}^{3.3} \qquad [2.11]$$

where L_{dv} is the dorso-ventral length of the valve. The scaling of muscle mass-specific power was plotted as a function of body mass and is the main focus of discussion in this chapter. Variables were also plotted against muscle mass for comparison. As Hill's (1950) model predicts the scaling of muscle mass-specific power to scale with the same scaling exponent of cycle frequency (-0.333), muscle power and its associated variables were also plotted against cycle frequency to explore how changes in cycle frequency affected the scaling of these measurements.

2.3.5 Statistical analysis

Statistical analysis was carried out using Igor Pro (Version 6.37, WaveMetrics, Lake Oswego, OR). Statistical significance was accepted at the 0.05 level. Scaling relationships were analysed using ordinary-least squares regressions, which allowed for any statistically significant relationships between two variables to be determined (*F*-test).

2.4 Results

Table 2.1. Allometric relationships ($y = aM_b^b$; M_b in g) of body and muscle morphology in *A. irradians* (*n* = 23), *A. opercularis* (*n* = 18) and *P.maximus* (*n* = 23).

y	units	species	r^2	*a*	*b* (±95%CI)	*P*
		A. irradians	0.98	15.83	0.383 (±0.030)	<0.001
L_{ap}	mm	*A. opercularis*	0.99	18.51	0.324 (±0.043)	<0.001
		P.maximus	0.99	22.46	0.323 (±0.016)	<0.001
		A. irradians	0.97	16.56	0.355 (±0.029)	<0.001
L_{dv}	mm	*A. opercularis*	0.98	19.50	0.306 (±0.028)	<0.001
		P.maximus	0.99	21.94	0.306 (±0.014)	<0.001
		A. irradians	0.95	5.97	0.407 (±0.054)	<0.001
L_{sh}	mm	*A. opercularis*	0.98	5.45	0.367 (0.043)	<0.001
		P.maximus	0.99	4.74	0.358 (±0.066)	<0.001
		A. irradians	0.94	0.05	1.058 (±0.298)	<0.001
M_m	g	*A. opercularis*	0.97	0.03	1.459 (±0.334)	<0.001
		P.maximus	0.99	0.06	1.148 (±0.090)	<0.001
		A. irradians	0.95	6.74	0.433 (±0.062)	<0.001
L_{max}	mm	*A. opercularis*	0.9	6.97	0.377 (±0.068)	<0.001
		P.maximus	0.99	7.17	0.326 (±0.018)	<0.001
		A. irradians	0.96	0.19	1.658 (±0.155)	<0.001
A_m	mm^2	*A. opercularis*	0.97	0.18	1.852 (±0.236)	<0.001
		P.maximus	0.99	0.67	1.374 (±0.040)	<0.001

L_{ap}, anterior-posterior shell length.

L_{dv}, dorsal ventral shell length.

L_{sh}, shell height.

M_m, muscle mass.

L_{max}, maximum muscle length during swimming.

A_m, muscle cross sectional area

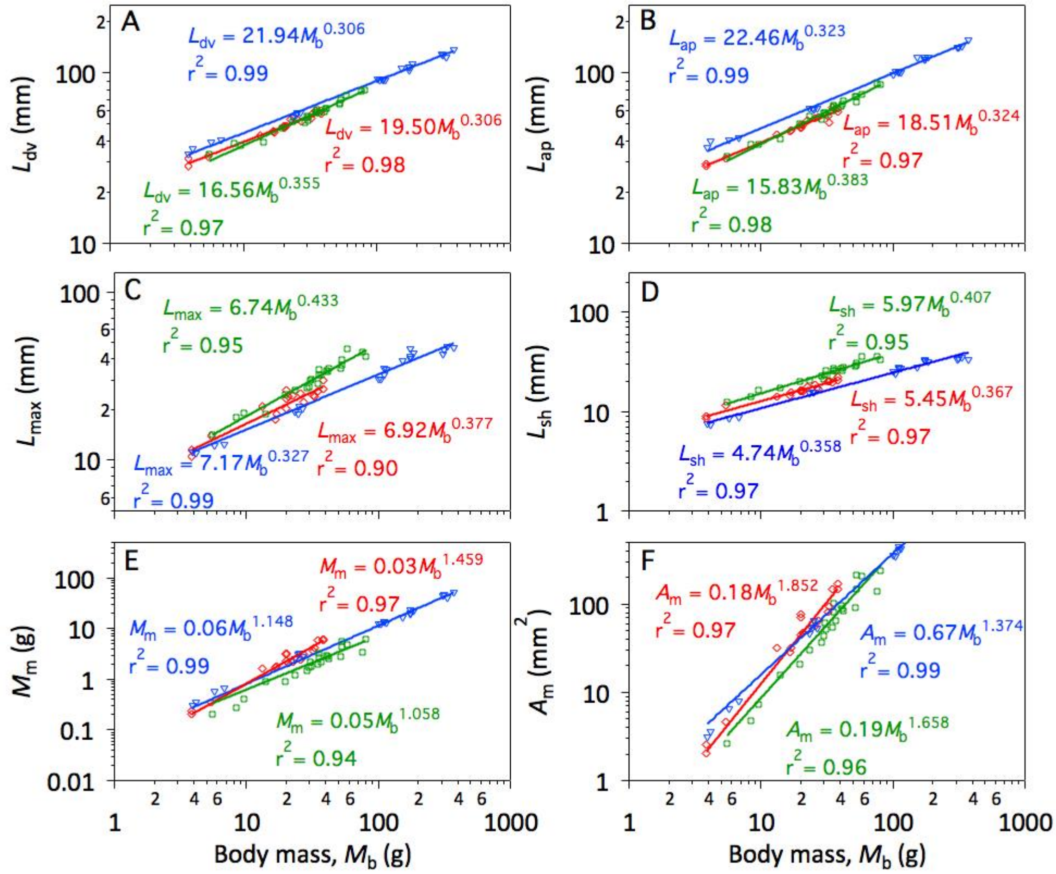

Figure 2.1. The scaling of morphology with body size in scallops. In *A. irradians*, (green squares), *A. opercularis* (red diamonds) and *P. maximus* (blue triangles). The scaling of shell anterior-posterior length (A), shell dorsal ventral length (B), maximum muscle length (C), shell height (D), muscle mass (E) and muscle cross sectional area (F) as a function of body size.

2.4.1 Scaling of morphology

Body mass covered a 15-fold range in bay scallops (5.54-80.62g), a 10-fold range in queen scallops (3.85-38.11g), and a 96-fold range in king scallops (3.90-373.45g). The scaling of morphological variables for the three species of scallops are summarised in Table 2.1 and figure 2.1. Muscle mass increased with increasing body mass in all three species of scallops, with larger scallops having relatively heavier muscles than smaller scallops (bay scallops α $M_b^{1.058}$, queen scallops α $M_b^{1.459}$, king scallops α $M_b^{1.148}$; fig. 2.1E). The muscle of larger scallops also had proportionally larger cross sectional areas than smaller scallops, indicated by the scaling exponents exceeding 0.667 (fig. 2.1F).

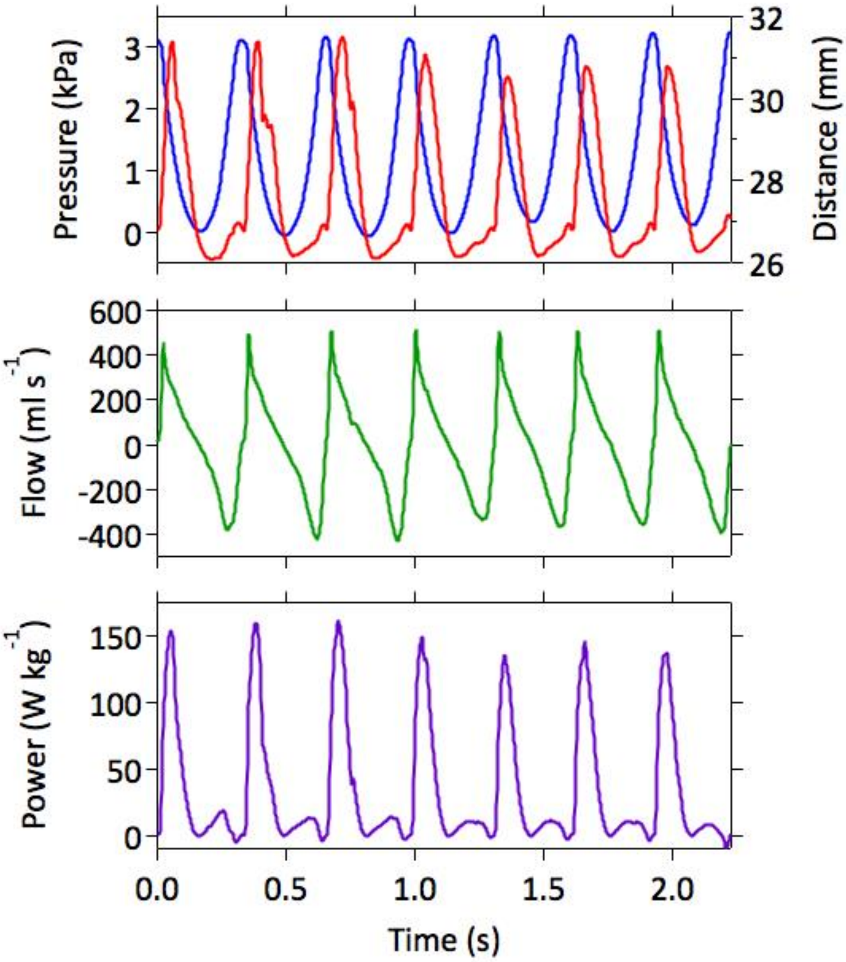

Figure 2.2. Instantaneous recording of length change (mm; red line), pressure (kPa; blue line), water flow (ml s^{-1}; green line) and calculated muscle mass-specific power out (W kg^{-1}; purple line) in a bay scallop performing an escape swim.

2.4.2 Escape swimming

Swimming mechanics were fundamentally similar across the three species of scallop. Upon the start of valve adduction, mantle pressure and flow rate increased sharply as the valves were pulled together as water was forced out from the pallial cavity through the jets formed by the mantle (Chapter 4; fig. 2.2). Pressure fell to ambient levels and flow rate reached zero once the valves became fully closed and the muscle reached its shortest length. Upon valve abduction, the mantle pressure became negative, and flow rate increased as water entered the mantle cavity through the opening ventral gape. There was a slight increase in mantle pressure approximately mid-way through valve abduction prior to the subsequent adduction.

Table 2.2. Allometric relationships ($y = aM_b^b$; M_b in g) between i*n vivo* muscle performance in three species of scallops in relation to body mass.

Parameter, *y*	units	species	r^2	*a*	*b* (±95%CI)	*P*
Peak power	W kg^{-1}	*A. irradians*	0.24	456.02	-0.203 (±0.129)	<0.05
		A. opercularis	0.5	443.61	-0.313 (±0.167)	<0.01
		P.maximus	0.49	245.46	-0.145 (±0.071)	<0.001
Average power	W kg^{-1}	*A. irradians*	0.23	132.40	-0.266 (±0.159)	<0.01
		A. opercularis	0.34	89.29	-0.266 (±0.159)	<0.01
		P.maximus	0.71	60.92	-0.150 (±0.079)	<0.01
Work	J kg^{-1}	*A. irradians*	0.07			NS
		A. opercularis	0.14			NS
		P.maximus	0.08			NS
Mean stress	kN m^{-2}	*A. irradians*	0.03			NS
		A. opercularis	0.02			NS
		P.maximus	0.04			NS
Frequency	Hz	*A. irradians*	0.31	4.15	-0.117 (±0.082)	<0.01
		A. opercularis	0.71	5.72	-0.122 (±0.039)	<0.001
		P.maximus	0.75	4.24	-0.134 (±0.029)	<0.001
Strain		*A. irradians*	0.13			NS
		A. opercularis	0.12			NS
		P.maximus	0.35	0.36	-0.052 (±0.033)	<0.01
Proportion of the cycle spent shortening		*A. irradians*	0.33	0.61	-0.050 (0.032)	<0.01
		A. opercularis	0.11			NS
		P.maximus	0.4	0.62	-0.031 (±0.018)	<0.01
Shortening velocity	L s^{-1}	*A. irradians*	0.28	1.79	-0.149 (±0.055)	<0.01
		A. opercularis	0.29	2.95	-0.144 (±0.056)	<0.05
		P.maximus	0.77	2.43	-0.153 (±0.065)	<0.001
Shortening duration	ms	*A. irradians*	0.19	0.13	0.097 (±0.041)	<0.05
		A. opercularis	0.30	0.11	0.080 (±0.031)	<0.05
		P.maximus	0.59	0.16	0.087 (±0.020)	<0.001

Table 2.3. Allometric relationships ($y = aM_m^b$; M_m in g) between i*n vivo* muscle performance in three species of scallops in relation to muscle mass.

Parameter, *y*	units	species	r^2	*a*	*b* (±95%CI)	*P*
Peak power	W kg^{-1}	*A. irradians*	0.34	252.59	-0.171 (±0.086)	<0.01
		A. opercularis	0.59	216.67	-0.253 (±0.082)	<0.001
		P.maximus	0.50	174.63	-0.132 (±0.062)	<0.01
Average power	W kg^{-1}	*A. irradians*	0.33	60.86	-0.218 (±0.110)	<0.01
		A. opercularis	0.41	47.18	-0.194 (±0.100)	<0.01
		P.maximus	0.50	42.79	-0.136 (±0.070)	<0.01
Work	J kg^{-1}	*A. irradians*	0.17			NS
		A. opercularis	0.09			NS
		P.maximus	0.20			NS
Mean stress	kN m^{-2}	*A. irradians*	0.09			NS
		A. opercularis	0.04			NS
		P.maximus	0.04			NS
Frequency	Hz	*A. irradians*	0.22	2.92	-0.078 (±0.066)	<0.05
		A. opercularis	0.55	4.26	-0.086 (±0.027)	<0.001
		P.maximus	0.75	3.11	-0.123 (±0.026)	<0.001
Strain		*A. irradians*	0.13			NS
		A. opercularis	0.09			NS
		P.maximus	0.32	0.32	-0.046 (±0.031)	<0.01
Proportion of the cycle spent shortening		*A. irradians*	0.31	0.52	-0.036 (±0.024)	<0.01
		A. opercularis	0.10			NS
		P.maximus	0.41	0.58	-0.029 (±0.016)	<0.01
Shortening velocity	L s^{-1}	*A. irradians*	0.24	1.14	-0.122 (±0.055)	<0.05
		A. opercularis	0.28	2.08	-0.098 (±0.085)	<0.05
		P.maximus	0.74	1.70	-0.138 (±0.031)	<0.001
Shortening duration	ms	*A. irradians*	0.11	0.13		NS
		A. opercularis	0.33	0.13	0.058 (±0.043)	<0.05
		P.maximus	0.41	0.19	0.088 (±0.035)	<0.001

Table 2.4. Allometric relationships ($y = af^b$; f in Hz) between i*n vivo* muscle performance in three species of scallops in relation to cycle frequency.

Parameter, *y*	units	species	r^2	*a*	*b* (±95%CI)	*P*
Peak power	W kg^{-1}	*A. irradians*	0.10			NS
		A. opercularis	0.36	62.28	0.873 (±0.546)	<0.01
		P.maximus	0.31	14.10	1.843 (±0.610)	<0.01
Average power	W kg^{-1}	*A. irradians*	0.15			NS
		A. opercularis	0.37	2.52	2.012 (±1.290)	<0.01
		P.maximus	0.33	14.19	0.943 (±0.587)	<0.01
Work	J kg^{-1}	*A. irradians*	0.01			NS
		A. opercularis	0.11			NS
		P.maximus	0.01			NS
Mean stress	kN m^{-2}	*A. irradians*	0.01			NS
		A. opercularis	0.02			NS
		P.maximus	0.01			NS
Strain		*A. irradians*	0.01			NS
		A. opercularis	0.08			NS
		P.maximus	0.35	0.34	0.209 (±0.267)	<0.01
Proportion of the cycle spent shortening		*A. irradians*	0.36	0.39	0.259 (±0.123)	<0.01
		A. opercularis	0.08			NS
		P.maximus	0.36	0.45	0.214 (±0.135)	<0.01
Shortening velocity	L s^{-1}	*A. irradians*	0.26	0.55	0.663 (±0.267)	<0.05
		A. opercularis	0.31	0.28	1.394 (±0.454)	<0.05
		P.maximus	0.75	0.53	1.004 (±0.121)	<0.001
Shortening duration	ms	*A. irradians*	0.88	0.40	-0.764 (±0.053)	<0.01
		A. opercularis	0.48	0.31	-0.575 (±0.070)	<0.05
		P.maximus	0.37	0.44	-0.762 (±0.072)	<0.05

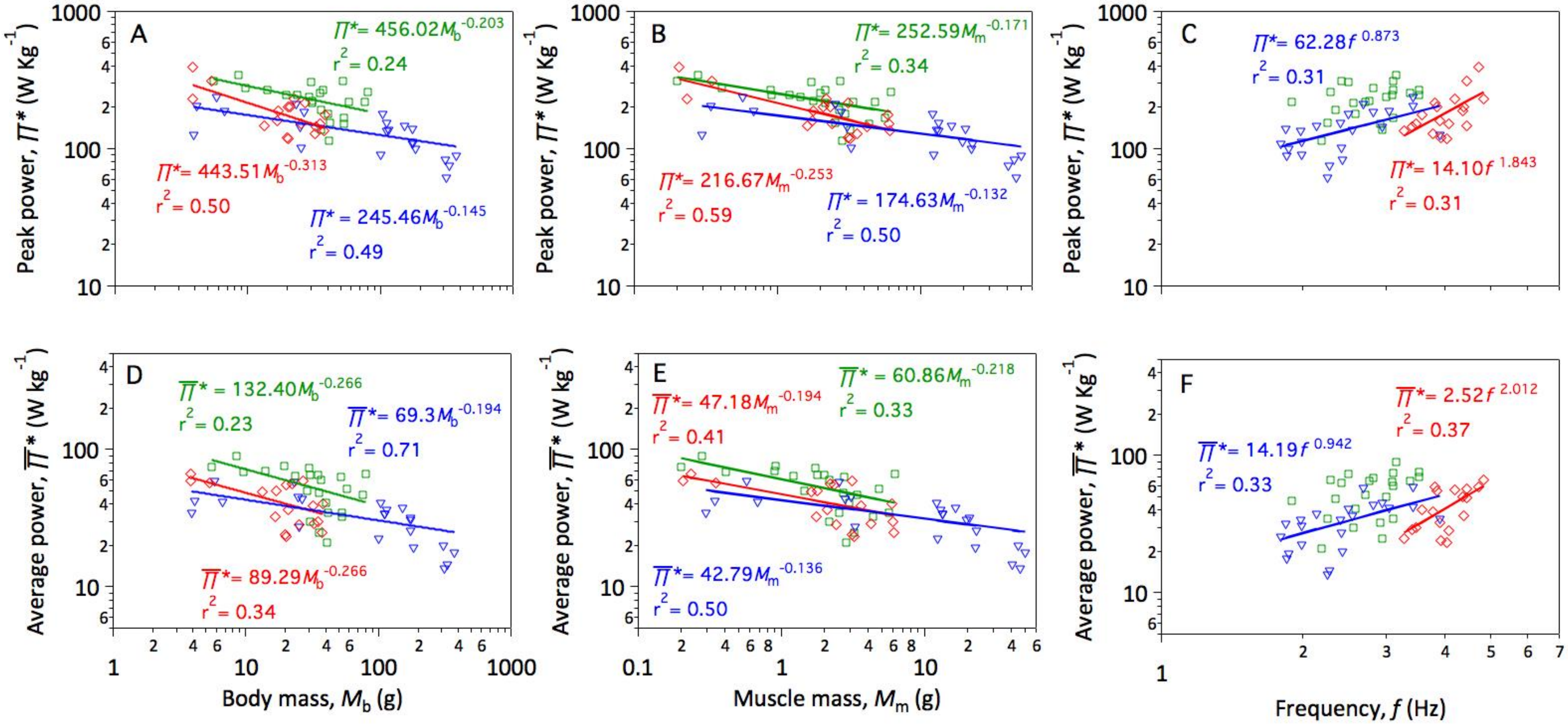

Figure 2.3. The scaling of peak power output (W kg^{-1}) and average power output (W kg^{-1}) in bay scallops, (green squares), queen scallops (red diamonds) and king scallops (blue triangles). Scaling as function of bod0y mass (A,D), muscle mass (B,E) and cycle frequency (C,F).

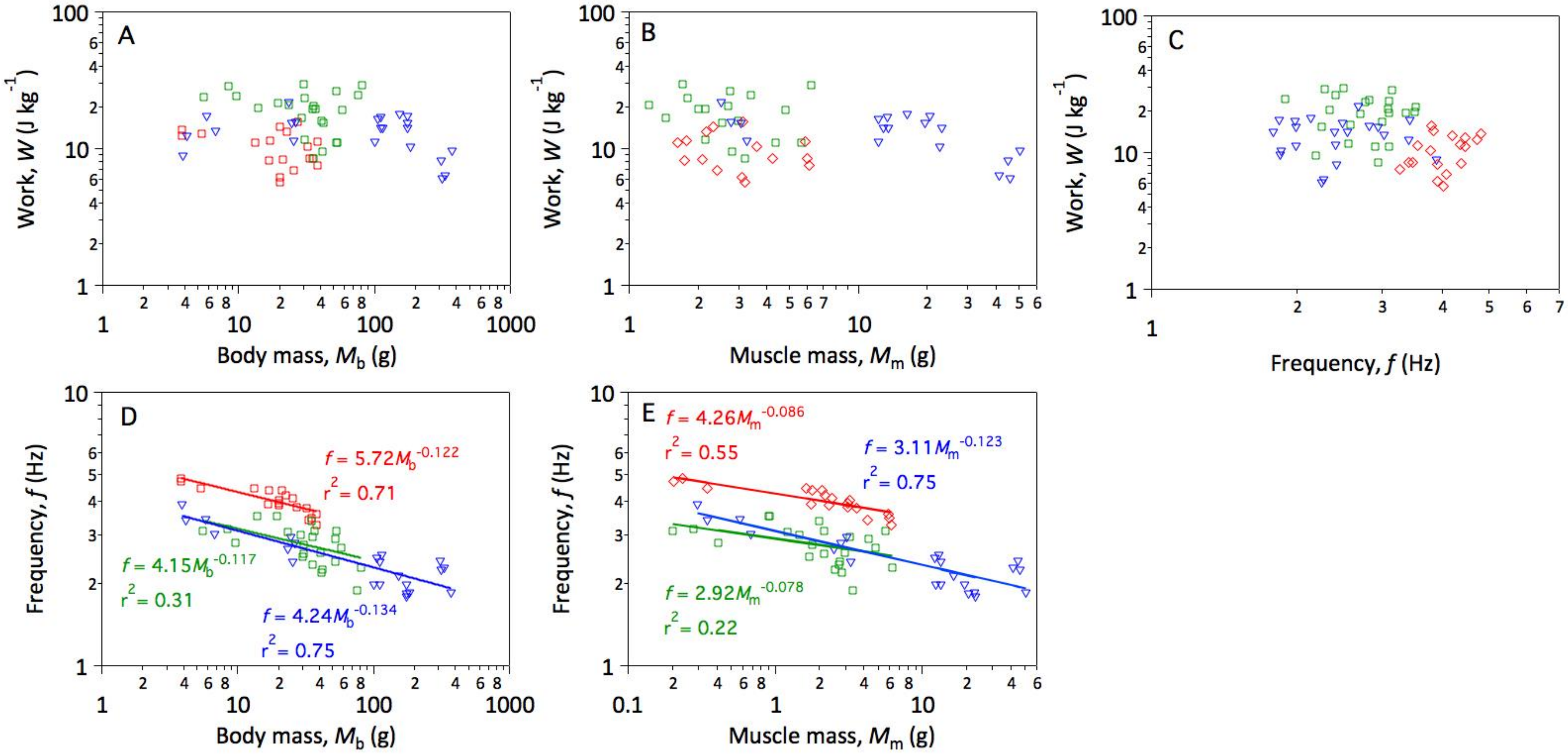

Figure 2.4. The scaling of work (J kg^{-1}) and cycle frequency (Hz) in bay scallops, (green squares), queen scallops (red diamonds) and king scallops (blue triangles). The scaling of work as a function of body mass (A), muscle mass (B) and cycle frequency (C). The scaling of cycle frequency as a function of body mass (D) and muscle mass (E).

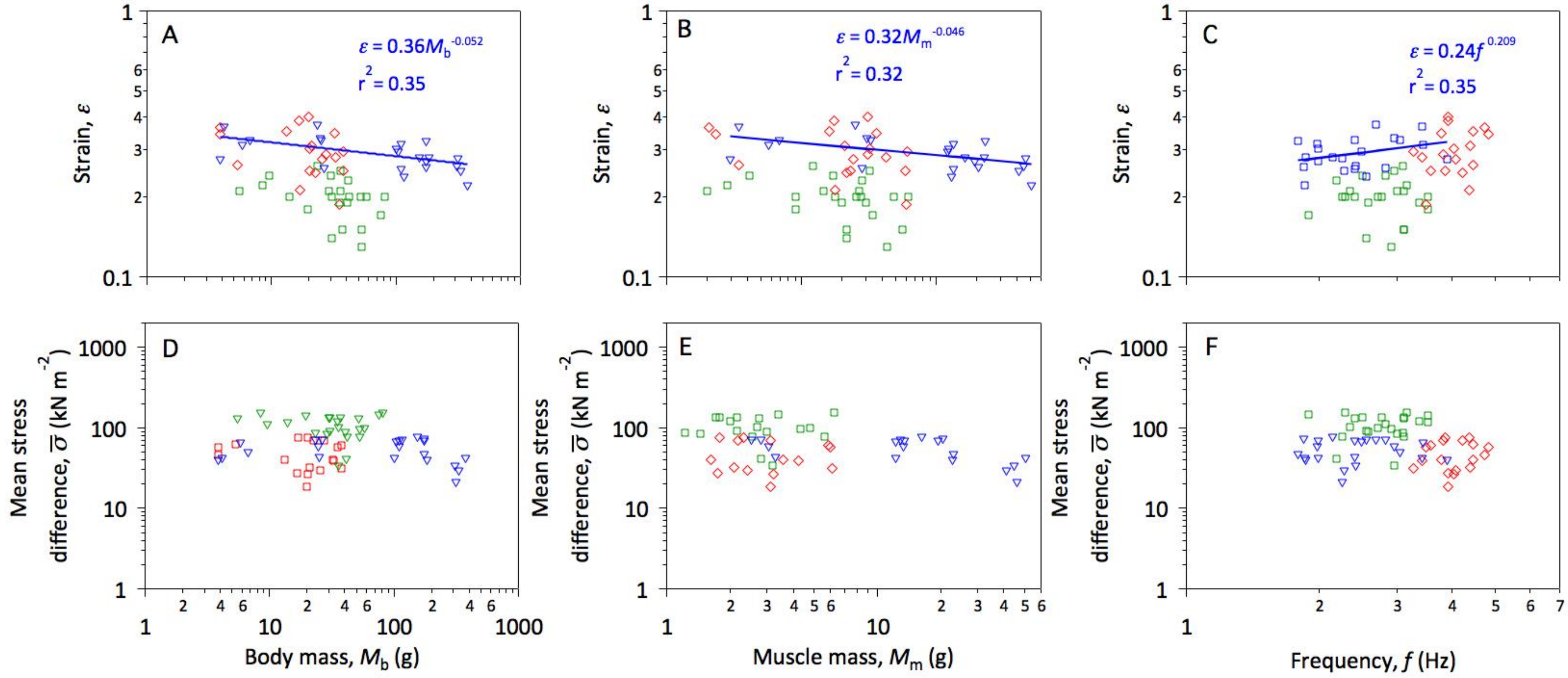

Figure 2.5. The scaling of strain and mean stress difference (kN m^{-2}) in bay scallops, (green squares), queen scallops (red diamonds) and king scallops (blue triangles). The scaling of strain as a function of body mass (A), muscle mass (B) and cycle frequency (C). The scaling of mean stress difference as a function of body mass (D), muscle mass (E) and cycle frequency (F).

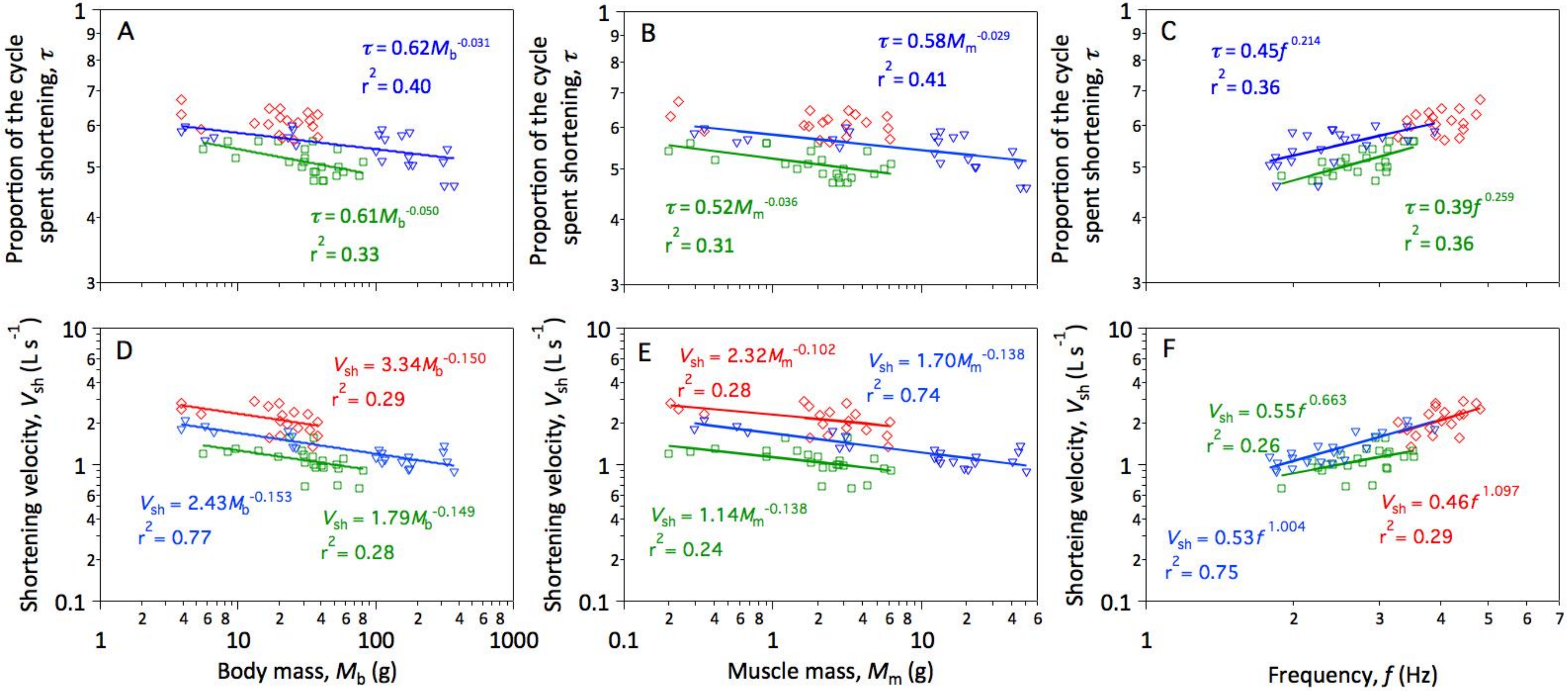

Figure 2.6. The scaling of the proportion of the cycle spent shortening and shortening velocity (L s⁻¹) in bay scallops, (green squares), queen scallops (red diamonds) and king scallops (blue triangles). The scaling of the proportion of the cycle spent shortening as a function of body mass (A), muscle mass (B) and cycle frequency (C). The scaling of shortening velocity as a function of body mass (D), muscle mass (E) and cycle frequency (F).

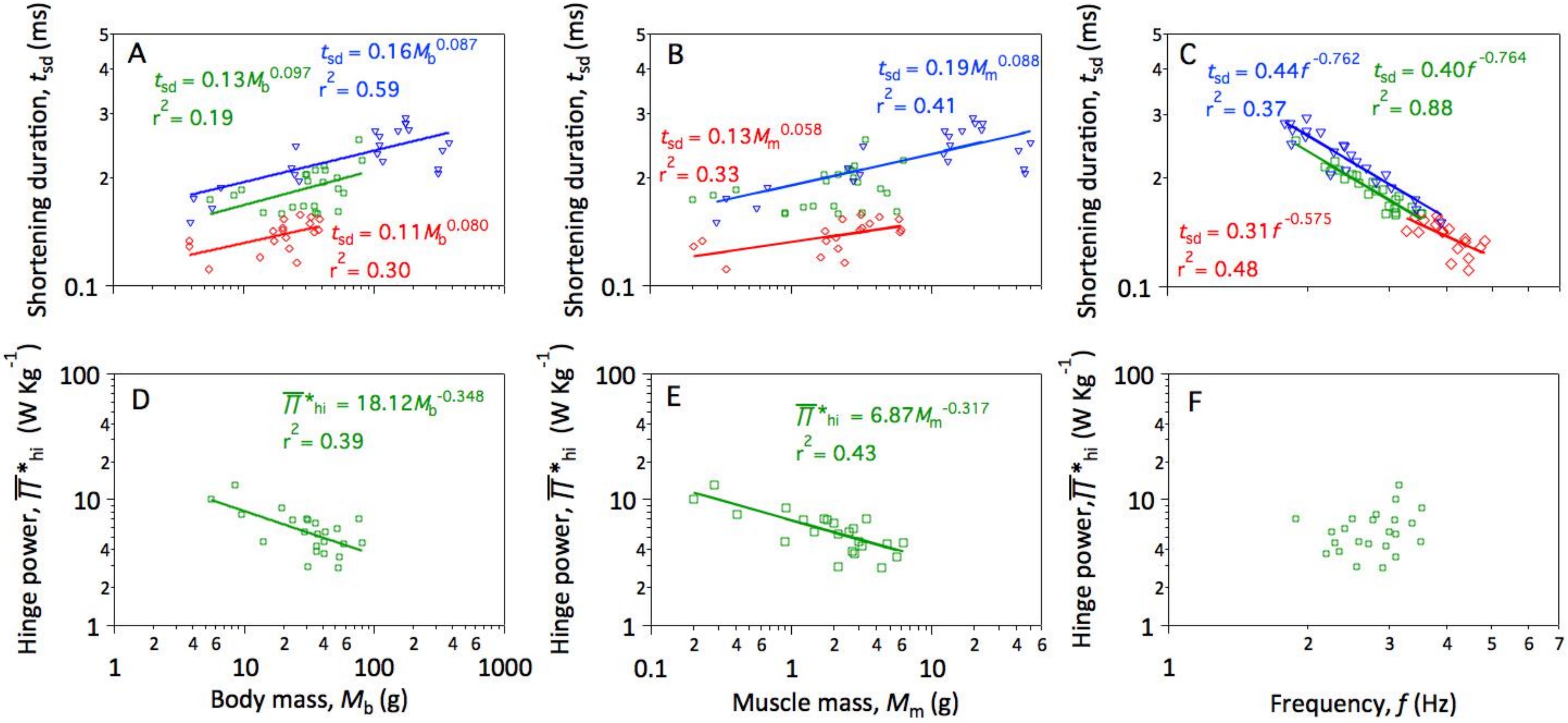

Figure 2.7 The scaling of shortening duration (ms) and hinge power (W kg^{-1}) in bay scallops, (green squares), queen scallops (red diamonds) and king scallops (blue triangles). Scaling of shortening velocity as a function of body mass (A), muscle mass (B) and cycle frequency (C). Scaling of estimated hinge power in bay scallops as a function of body mass (D), muscle mass (E) and cycle frequency (F).

2.4.3 Scaling of *in vivo* muscle performance with mass and frequency

Muscle mass-specific peak power output decreased with increasing body mass in all three scallop species, scaling α $M_b^{-0.203}$ in bay scallops, α $M_b^{-0.313}$ in queen scallops and α $M_b^{-0.145}$ in king scallops (fig. 2.3A). Muscle mass-specific peak power output decreased with increasing muscle mass, scaling as $M_m^{-0.171}$ in bay scallops, $M_m^{-0.253}$ in queen scallops and $M_m^{-0.132}$ in king scallops (fig. 2.3B). Muscle mass-specific peak power output was independent of cycle frequency in bay scallops, but increased with increasing cycle frequency in queen scallops (α $f^{0.873}$) and king scallops (α $f^{1.843}$; fig. 2.3C). Muscle mass-specific average power output scaled as $M_b^{-0.266}$ in bay scallops, $M_b^{-0.266}$ in queen scallops and $M_b^{-0.150}$ king scallops (fig. 2.3D). Mass-specific average power output scaled with muscle mass as $M_m^{-0.218}$ in bay scallops, $M_m^{-0.194}$ in queens and $M_b^{-0.136}$ king scallops (fig. 2.3E). Muscle mass-specific average power output was independent cycle frequency in bay scallops, but scaled as $f^{2.012}$ in queen scallops and $f^{0.943}$ in king scallops (fig. 2.3F). There was no scaling relationship between muscle mass-specific work done by the adductor muscle and body mass, muscle mass or cycle frequency, with a mean value of 19.57 ±1.31 J kg^{-1} (bay scallops), 10.34 ±0.7 J kg^{-1} (queen scallops) and 13.57 ±0.86 J kg^{-1} (king scallops; fig. 2.4A, 2.4B, 2.4C). Cycle frequency scaled negatively with increasing body mass in all three species, scaling as $M_b^{-0.117}$ in bay scallops, $M_b^{-0.122}$ in queen scallops and $M_b^{-0.134}$ in king scallops (fig. 2.4D). Cycle frequency also scaled negatively with increasing muscle mass in all three species, scaling as $M_m^{-0.078}$ in bay scallops, $M_b^{-0.086}$ in queens and $M_b^{-0.123}$ in king scallops (fig. 2.4E).

Strain was independent of body mass, muscle mass and frequency in both bay (mean = 0.2±0.01) and queen (mean = 0.3±0.01) scallops, but decreased with increasing body mass, (α $M_b^{-0.054}$) muscle mass (α $M_m^{-0.046}$) and increased with increasing frequency (α $f^{0.209}$) in king scallops (range = 0.22-0.37; fig 2.5A, 2.5B, 2.5C). Mean stress difference was independent of body mass, muscle mass and cycle frequency in all three species, with mean values of 108.36 ±6.9 kN m^{-2} (bay scallops), 47.57 ±4.36 kN m^{-2} (queen scallops) and 53.99 ±3.52 kN m^{-2} (king scallops; fig. 2.5D, 2.5E, 2.5F).

The proportion of the cycle spent shortening, decreased with increasing body mass in bay scallops ($\alpha\ M_b^{-0.050}$) and in king scallops as ($\alpha\ M_b^{-0.031}$), but was independent of body mass in queen scallops (mean proportion of cycle spent shortening 0.61±0.01; fig. 2.6A). Similarly, the proportion of the cycle spent shortening, decreased with increasing muscle mass in bay scallops ($\alpha\ M_m^{-0.036}$) and in king scallops ($\alpha\ M_b^{-0.029}$), but was independent of body mass in queen scallops (fig. 2.6B). The proportion of the cycle spent shortening, increased with increasing frequency in bay scallops ($\alpha\ f^{0.259}$) and in king scallops as ($\alpha\ f^{0.259}$), but was independent of body mass in queen scallops (fig. 2.6C). In the majority of swims, the proportion of the cycle spent shortening exceeded 50%. Shortening velocity decreased with increasing body and muscle mass in all three species, scaling as $M_b^{-0.149}$ in bay scallops, $M_b^{-0.144}$ in queen scallops and $M_b^{-0.128}$ in king scallops (fig. 2.6D), and as $M_m^{-0.138}$ in bay scallops, $M_m^{-0.098}$ in queen scallops and $M_b^{-0.153}$ in king scallops (fig. 2.6E). Shortening velocity increased with increasing cycle frequency in all three species, scaling as $M_b^{0.663}$ in bay scallops, $M_b^{1.394}$ in queen scallops and $M_b^{1.004}$ in king scallops (fig. 2.6F). Shortening duration increased with increasing body mass in all three species, scaling $\alpha\ M_b^{0.097}$ in bay scallops, $M_b^{0.080}$ in queen scallops and $M_b^{0.087}$ in king scallops (fig. 2.7A). Shortening duration also increased with increasing muscle mass in queen scallops ($\alpha\ M_m^{0.058}$) and king scallops ($\alpha\ M_m^{0.088}$), but was independent of muscle mass in bay scallops (mean shortening duration 0.17±0.01ms; fig. 2.7B). Shortening duration decreased with increased cycle frequency in all three species, scaling $\alpha\ M_b^{-0.764}$ in bay scallops, $M_b^{-0.575}$ in queen scallops and $M_b^{-0.762}$ in king scallops (fig. 2.7C).

Estimated hinge power scaled negatively with increasing body mass, scaling as $M_b^{-0.348}$ (fig. 2.7D), and with increasing muscle mass, as $M_m^{-0.348}$ (fig. 2.7E). There was no scaling of estimated hinge power with cycle frequency (fig. 2.7F).

2.5 Discussion

Scallop swimming is powered by the contraction of a single adductor muscle, and is carried out primarily as a means of escaping predation; swimming performance is therefore likely to be under selective pressure in favour of a high average power output. Here we used escape swimming performance in scallops covering a 96-fold range in body mass to investigate how muscle performance scales with body mass and contractile frequency. The empirically derived scaling relationships were compared to theoretical scaling relationships expected if scaling is in accordance with geometric (α $M_b^{-0.333}$, Hill, 1950) or elastic (α $M_b^{-0.250}$, McMahon) similarity.

2.5.1 Morphological scaling during growth

Hill's (1950) oft cited predications on the scaling effect of body size on animal locomotor performance are based on numerous assumptions on the scaling of an animals' dimensions and the scaling of intrinsic contractile properties of muscle. One of Hill's assumptions was that as animals grow they would do so in a geometrically similar way, the consequences of this were that muscle lengths should scale as $M_b^{0.333}$ and muscle masses should scale with body mass with a scaling exponent of 1, whilst muscle cross sectional area should scale as $M_b^{0.667}$. In queen and king scallops, the dimensions of the shell and length of the muscle all scaled with scaling exponents close to that expected of geometric similarity. Bay scallops however were found to deviate from this predicted scaling relationship, with shell height as $M_b^{0.407}$ and muscle length scaling as $M_b^{0.433}$, meaning muscles were relatively longer in larger scallops than would be predicted if the animals were scaling geometrically. Muscle mass and cross sectional area were also found not to scale according to Hill's predictions across all 3 species, with muscle mass scaling as $M_b^{1.058}$, $M_b^{1.459}$ and $M_b^{1.148}$, whilst muscle cross sectional area scaled as $M_b^{1.658}$, $M_b^{1.852}$ and $M_b^{1.374}$ (table 2.1), suggesting that muscles get relatively larger and have a larger cross sectional area as they grow than they would do if they increasing in size geometrically. The scaling exponents predicted from McMahon's elastic similarity model do not fit with the scaling relationships found within scallop muscles either, with McMahon predicting muscle length to scale as $M_b^{0.250}$, and muscle cross sectional area to scale as $M_b^{0.750}$. Morphologically speaking at least, scallops do not fit entirely within either the geometric of elastic similarity models proposed for the scaling of animals during growth.

2.5.2 Scaling of mass specific muscle power output

Average muscle-mass specific power output was found to decrease with increasing body mass in all three scallop species studied ($\alpha M_b^{-0.266}$ in bay scallops, $\alpha M_b^{-0.266}$ in queen scallops and $\alpha M_b^{-0.150}$ in king scallops). Peak instantaneous muscle mass-specific power output scaled as $\alpha M_b^{-0.203}$ in bay scallops, $\alpha M_b^{-0.313}$ in queen scallops and $\alpha M_b^{-0.145}$ in king scallops (fig. 2.3). Similarly, average muscle-mass specific power output decreased with increasing muscle mass in all three scallop species ($\alpha M_m^{-0.218}$ in bay scallops, $\alpha M_m^{-0.194}$ in queen scallops and $\alpha M_m^{-0.136}$ in king scallops). Peak instantaneous muscle mass-specific power output scaled as $\alpha M_m^{-0.171}$ in bay scallops, $\alpha M_b^{-0.253}$ in queen scallops and $\propto M_b^{-0.132}$ in king scallops (fig. 2.3). The difference in scaling exponents between body mass and muscle mass is not surprising given that muscle mass did not scale isometrically. Previous studies investigating the scaling of maximum muscle mass-specific power output during escape responses are limited and consist of studies investigating take-off flight in birds and studies of frog jumping. Jackson and Dial (2011) measured the power output of Corvidae pectoralis muscles during escape flight using sonomicrometry to determine muscle length change and strain gauges attached to the delto-pectoral crest (DPC) of the humerus to estimate pectoralis muscle force. In the Corvidae, muscle mass-specific power was found to scale negatively with pectoralis muscle mass, scaling as $M_m^{-0.180}$. The technique used by Jackson and Dial (2011) has also been attempted on birds in the Phasianidae but was unsuccessful due to the morphology of the DPC in these birds (Tobalske and Dial, 2000). Instead, an aerodynamic analysis has been performed using kinematic and morphological data to estimate the total aerodynamic power during escape take-off (Askew et al., 2001). Muscle mass-specific power output in birds in the Phasianidae was found to be approximately constant across an approximately 100-fold range in body mass. Maximum muscle mass-specific power determined from maximum load-lifting capability in hummingbirds has been estimated using an aerodynamic analysis and scales negatively with muscle mass with an exponent ranging from -0.160 to -0.250, depending upon the altitude from which the hummingbirds were derived (Altshuler et al., 2010). However, during similar maximal loading in bumblebees, the relationship between the muscle mass-specific power output and muscle mass is not significant (Buchwald and Dudley, 2010). In frogs, the scaling of jumping power has also been determined, both inter- (Marsh, 1994) and intra-specifically (Wilson et al., 2000). Body mass-specific power scales in striped marsh frog as $M_b^{-0.460}$ (Wilson et al., 2000) and across several species of frog covering a 1000-fold range in body mass is independent of body mass (Marsh, 1994).

In making comparisons between studies, differences and limitations should be highlighted. First, in all studies (including our study on scallops) it is assumed that animals are performing maximally. It has been demonstrated that previous laboratory studies on frog jumping that it may be difficult to elicited maximal performance in laboratory experiments (Astley et al., 2013) and that this difficulty may be heightened by the use of captive-bred animals (Jackson and Dial, 2011). Second, some estimates of the scaling of take-off performance use aerodynamic models which have a degree of uncertainty in the calculation of the different power components. For example, the use of profile drag coefficients determined under steady state conditions is inappropriate as they fail to take account of the increased drag resulting from the presence of a leading edge vortex (Askew et al., 2010; Ellington, 1999) that is present in insects and hummingbirds (Bomphrey et al., 2005; Ellington et al., 1996; Warrick et al., 2009). Third, there may be differences in the scaling of power output with body mass between species of different size (inter-specifically) and between individuals of the same species of different size (intra-specifically, e.g. during ontogeny). Fourth, there may be differences in the way in which power scales with body mass in activities powered by muscles with different fibre types. Swimming in scallops, frog jumping and take-off in phasianids is powered by muscles composed of fast glycolytic fibres whereas flight in insects and hummingbirds is driven by aerobic muscle fibres (asynchronous insect flight muscle in bumblebees and fast oxidative glycolytic fibres in hummingbirds).

The scaling of maximal muscle power output with body mass has been investigated *in vitro*, using either the work loop technique (Josephson, 1985) or isotonic contractions (Marsh, 1988). An advantage of isolated muscle physiology experiments is that they overcome the issues associated with variable levels of motivation in locomotor studies. Using the work loop technique, maximum muscle mass-specific power has been found to be independent of body mass in *Dipsosaurus* iliofibularis muscle (Johnson et al., 1993) and in two hind limb muscles in *Xenopus* (Altringham et al., 1996). However, strain was not optimised in these experiments, meaning that power may not have been maximal and power may therefore not reflect maximal *in vivo* performance; this could affect the scaling of mass-specific power with body mass. The power output of abdominal myotomal muscle from Atlantic cod undergoing cyclical contractions in which strain was optimised for maximum power, decreased with increasing body mass ($\alpha\ M_b^{-0.100}$; Anderson and Johnston, 1992). During isotonic contractions, muscle mass-specific power output was found to be independent of body mass in *Dipsosaurus* iliofibularis muscle (Marsh, 1988). Using the same technique, maximal muscle power output was found to decrease with increasing body mass in bay ($\alpha\ M_b^{-0.334}$) queen ($\alpha\ M_b^{-0.430}$) and king ($\alpha\ M_b^{-0.929}$) scallops (Chapter 3). The power generated during an isotonic contraction may be a good estimate of the peak instantaneous power, but far exceeds the power that can be generated during a cyclical contraction and may scale differently with body mass.

To summarise, the intra-specific decrease of power with increasing body mass in scallops is similar (though less steep) to the negative intra-specific scaling of power estimated from frog jumping (Wilson et al., 2000). However, the mismatch between jump power and muscle power (Peplowski and Marsh, 1997; Roberts et al., 2011) means that the scaling in frogs may not reflect the scaling of maximum muscle power output. Interspecifically, power is either independent (phasianids: Tobalske and Dial, 2000; Askew et al., 2001; frogs: Marsh, 1994) or decreases with increasing body mass (corvids: Jackson and Dial, 2011; hummingbirds: Altshuler et al., 2010).

2.5.3 Scaling of muscle mass-specific work

Power is the rate of doing work and is therefore the product of work and cycle frequency. To gain insight into the scaling of power requires knowledge of how work and frequency, together with the scaling of the determinants of work, i.e. stress and strain, scale with body mass.

Muscle mass-specific work was found to be independent of body mass in all three species of scallop, with mean values of 19.57 ±1.31 J kg^{-1}, 13.43 ±0.86 J kg^{-1} and 10.34 ±0.7 J kg^{-1} in bay, king and queen scallops, respectively (fig. 2.4A). During escape flight in birds in the Corvidae and Phasianidae, muscle mass-specific work was also independent of body mass (Tobalske and Dial, 2000; Askew et al., 2001; Jackson and Dial's, 2011). The scaling of muscle mass-specific work with muscle mass can be estimated from the data reported in maximally loaded hummingbirds (Altshuler et al., 2010). At the lower altitudes (low to highland), muscle mass-specific work is approximately independent of muscle mass; in alpine birds muscle mass-specific work scales as $M_{\mathrm{m}}^{-0.110}$. The absence of scaling of muscle mass-specific work with body mass dictates that the scaling of muscle mass-specific power is dependent on the scaling of frequency with mass. Frequency decreased with increasing body mass in all three species of scallop (α $M_{\mathrm{b}}^{-0.117}$ in bay scallops, α $M_{\mathrm{b}}^{-0.122}$ in queen scallops and α $M_{\mathrm{b}}^{-0.134}$ king scallops; fig. 2.4C). During escape take-off flights, wing beat cycle frequency scaled as $M_{\mathrm{b}}^{-0.249}$ and $M_{\mathrm{b}}^{-0.260}$ in Phasianidae birds (Tobalske and Dial, 2000; Askew et al., 2001) and as $M_{\mathrm{m}}^{-0.290}$ in Corvidae (Jackson and Dial, 2011). In maximally loaded hovering, hummingbird wing beat frequency scaled as $M_{\mathrm{b}}^{-0.410}$ to $M_{\mathrm{b}}^{-0.480}$, depending on elevation (Altshuler et al., 2010).

The scaling exponents for intraspecific scaling in scallops are similar to those predicted for elastic similarity ($M_{\mathrm{b}}^{-0.125}$). During flight, inter-specific scaling of wing beat frequency with body mass is similar to the exponent predicted for elastic similarity (phasianids and corvids) or exceeds the exponent predicted for geometric similarity (hummingbirds).

2.5.4 Scaling of stress, strain and the proportion of the cycle spent shortening

Hill (1950) predicted that muscle mass-specific work would be independent of body mass due to the constancy of muscle stress and strain. The independence of muscle mass-specific work with mass in scallop swimming and in bird flight is consistent with this prediction, however, the scaling of stress and strain must be determined too.

Mean stress difference (the difference in muscle stress during shortening and lengthening; Askew and Marsh, 2002), was independent of body mass in swimming scallops (Fig. 2.5D). Strain was also largely independent of body mass, with the exception of king scallops where strain decreased slightly with increasing body mass ($\propto M_b^{-0.052}$; fig. 2.5A). Mean muscle stress was also independent of body mass in escape flights in corvids, however, pectoralis muscle strain scaled positively with increasing muscle mass ($\alpha\ M_m^{0.12}$; Jackson and Dial, 2011). Within the Phasianidae during escape flights, mean stress difference and strain were independent of body mass (Tobalske and Dial, 2000; Askew et al., 2001). Data are unavailable for muscle strain and mean stress in hummingbirds during maximal hovering.

The proportion of the cycle spent shortening was found to decrease with increasing body mass in both bay and king scallops, showing a slight but significant negative relationship, scaling as $M_b^{0.050}$ and $M_b^{0.033}$. The proportion of the cycle the muscles spent shortening in the present study ranged from 67% in the smallest scallops to 46% in the largest ones (fig. 2.6A). Previous work on scallops has identified them as having an asymmetrical length change cycle, with as much as 65% of the contraction cycle spent shortening in *Chlamys hastata* (Marsh et al., 1992). Muscle power output increases as the proportion of the cycle spent shortening increases as a result of more complete activation of the muscle and an increase in the optimal strain (Askew and Marsh, 1997). Therefore, increasing the proportion of the cycle spent shortening might be expected to increase the mean stress generated during movement. However, this is not the case in scallops - mean stress is independent of body mass. The reasons for the constancy of stress may be related to the scaling the intrinsic contractile properties of the muscle. For instance, the twitch kinetics may become relatively slower (in relation to cycle frequency) in smaller animals. Alternatively or in addition, there may be changes to the curvature of the force velocity relationship with body mass.

Power output is the product of force and velocity. Due to the constancy of stress during shortening and lengthening, the scaling of shortening velocity will likely dictate the scaling of power output in scallops. Shortening velocity decreased with increased body mass in all three species, scaling as $M_b^{-0.149}$ in bay scallops, $M_b^{-0.150}$ in queen scallops and $M_b^{-0.153}$ in king scallops. In king scallops shortening velocity scales with a scaling exponent close to that of the scaling of average power ($M_b^{-0.153}$) suggesting that shortening velocity is a good predictor of the scaling of muscle power output (fig. 2.6D).

2.5.5 Scaling of hinge power

An essential component of the scallop locomotor system is the hinge. The composition of the hinge ligament is different to non-swimming bivalves such as oysters and mussels (Alexander, 1966; DeMont, 1990). In non-swimming bivalves, the central portion of the hinge is calcified. In scallops however, the central portion is not calcified and is instead composed of abductin, an elastic protein (Kelly and Rice, 1967). The scaling exponent for hinge power in the bay scallop was -0.348 (fig. 2.7D), which is a steeper slope than that found for the scaling of average power (-0.266). This indicates that larger scallops are using relatively less power to compress the hinge than smaller ones.

2.5.6 Comparison to theoretical models

Both geometric similarity and elastic similarity models predict that muscle power output will scale negatively with increased body size (scaling as $M_b^{-0.333}$ and $M_b^{-0.250}$, respectively). Average muscle power decreased with increasing body mass in bay scallops, scaling with an exponent of -0.266 (±0.159) and with an exponent of -0.266 (±0.159) in queen scallops. These exponents are close to the exponent expected of elastic similarity. However, the exponents assuming both geometric and elastic similarity fall within the 95% confidence limits of the empirically derived slopes, meaning that it is difficult to exclude either scaling model. The scaling exponent for average muscle power in king scallops is -0.150 (±0.079), which does not encompass the scaling exponent for either the geometric or elastic scaling models. The scaling exponents derived from comparing muscle power output to muscle mass have narrower confidence intervals, with muscle mass-specific power output scaling with an exponent of -0.218 (±0.110) in bay scallops and -0.194 (±0.100) in queen scallops, meaning that the only the exponents of elastic similarity lie within the 95% confidence limits of the empirically derived slopes. Once again however, the king scallops do not lie within either model, with a scaling exponent of -0.136 (±0.070). The differences in scaling between body mass and muscle mass likely reflect the fact that muscles were not found to scale isometrically, as is predicted by both geometric and elastic similarity. The different slopes suggest that larger scallops are further disadvantaged by having relatively larger muscles compared to smaller ones, which is reflected in their progressively worse whole organismal performance as they increase in mass, which is greater than would be expected from a loss in muscle performance alone (fig. 2.3).

Cycle frequency was found to scale with a scaling exponent closer to that expected of elastic similarity ($M_b^{-0.125}$) rather than geometric similarity ($M_b^{-0.333}$), with scaling exponents of -0.117 (±0.082) for bay scallops, -0.122 (±0.039) for queen scallops and -0.134 (±0.029) for king scallops. The scaling of cycle frequency is the primary determinant of the scaling of muscle mass-specific power. Muscle power output as a function of cycle frequency is predicted to scale with an exponent of 1 according to geometric similarity and an exponent of 2 according to elastic similarity. In queen scallops average muscle power output scaled with frequency with a scaling exponent of 2.012 (±1.290), in king scallops the exponent was 0.943 (±0.587). In contrast to this, average muscle power output was found to be independent of cycle frequency in bay scallops, though a trend similar to the scaling relationship observed in king scallops is apparent (fig. 2.3).

Both theoretical models predict that work should be independent of body size. This prediction was supported by all three scallop species studied, and resulted from the independence of mean stress difference and strain with body mass in the bay and queen scallop. Mean stress difference was also size-independent in scallops, but strain was found to decrease slightly with increasing size ($M_b^{-0.052}$).

2.5.7 Summary

The finding that muscle stress and strain were approximately constant and independent of body mass leads to the conclusion that muscle mass-specific work should be constant and therefore muscle mass-specific power should scale in proportion to cycle frequency. This is generally the case, however, trends in the proportion of the cycle spent shortening and strain to decrease with increasing body mass also seem to contribute to the scaling of muscle mass-specific power in scallops.

This study adds to the small number of studies looking at the scaling whole animal maximum muscle power output. The results support the traditional explanation that ontogenetically, muscle mass-specific power output is inversely proportional to body mass. Although no definitive answer can be given as to whether muscle power scales according to either geometric or elastic similarity, it has been shown that cycle frequency scales during ontogeny in scallops with a scaling exponent that is closer to that expected for elastic similarity rather than geometric similarity.

Chapter 3

The physiological determinants of the scaling of muscle power output during escape swimming in scallops

3.1 Abstract

The scaling of muscle power output with changing body size is a major determinant of size-related differences in animal locomotion. Scallops swim primarily to escape from predators and natural selection has likely operated on the structural design of the muscle in favour of a high power output. To investigate how muscle power scales with body mass *in vivo*, escape swimming was studied in three species of scallops. Muscle mass-specific peak power decreased with increasing body mass, scaling as $\sim M_b^{-0.220}$. The primary determinant of the scaling of power output was a decrease in cycle frequency, which scaled as $\sim M_b^{-0.124}$ across the three species studied. In order to gain insight into the physiological determinants of this scaling relationship, the intrinsic contractile properties of the adductor muscle were characterised *in vitro*. Isometric twitch kinetics and isotonic force-velocity relationships were characterised in three species of scallops covering a tenfold range in body size. Twitch contraction time (t_c) was found to increase with increasing body mass, in queen scallops (α $M_b^{0.272}$), but was independent of body size in bay and king scallops. V_{max} scaled with body size in all three species, with smaller animals found to have higher maximal muscle shortening velocities, scaling as $\sim M_b^{0.250}$. Neither of these parameters matched the scaling of cycle frequency however, indicating that the scaling of the intrinsic properties of the muscle are not the sole determinant of the scaling of cycle frequency in scallops.

3.2 Introduction

Body mass has often been cited as one of the major factors determining muscle mass-specific power output (Hill, 1950; McMahon, 1975; Pennycuick, 1975), with the available power from the muscles ultimately setting the limit of performance in animals.

An early theoretical model predicted that muscle power should scale in proportion to the scaling of muscle operating frequency, scaling as $M_b^{-0.333}$ (Hill, 1950). Therefore larger animals should generate less mass-specific power than smaller ones.

3.2.5 Whole animal approaches to the scaling of muscle power output

Escape performance has previously been used as a method of analysing the scaling of muscle mass-specific power output, as in these systems, all of the power required to produce movement can be assigned to a particular muscle or group of muscles. However, this approach is often met with two distinct limiting factors: attempting to elicit maximal performance from the animal being studied and measuring muscle power output directly. Previous work has attempted to use load lifting in insects and birds to elicit maximal flight performance (Altshuler et al., 2010; Chai and Millard, 1997; Marden, 1994), whilst deemed appropriate for hummingbirds due to their superior hovering ability, many species of insects and other birds are simply reluctant to fly with added mass and will not fly unless thoroughly trained. Aerodynamic analysis to quantify power output during escape flights was performed on birds that had been trained in the tests prior to measurement (Tobalske and Dial, 2000; Askew and Marsh, 2001), potentially bringing into question the assumption that maximal performance was elicited. Previous attempts to measure in *vivo* muscle power met with difficulties in attaching strain gauges to the delto-pectoral crest of the humerus in birds (Tobalske and Dial, 2000), however, recent experiments have been more successful with this approach (Jackson and Dial, 2011).

The intrinsic contractile properties of muscles ultimate determine the amount of power that they produce; the isometric stress of a muscle, the force-velocity relationship and muscle activation and deactivation kinetics (Josephson, 1993). These properties can be measured *in vitro* using isolated muscle fibres. The basis of the early models on how muscle power should scale with body mass was the isotonic relationship between muscle force and contraction velocity.

These models were built on several assumptions about muscles and how they operate. These were: (1) a constancy of muscle stress; (2) the geometric scaling of muscle length throughout ontogeny; (3) muscle strain is constant, which in turn predicts that a muscles' shortening velocity is proportional to its cycle frequency; (4) muscle maximal shortening velocity is proportional to cycle frequency; (5) the curvature of the force velocity relationship is constant.

3.2.2 The scaling of muscle architecture

The force that a muscle is able to produce is directly related to its myofibrillar cross-sectional area (McComas, 1996). The ultra structure of a muscle will have profound effects on the stress and mass-specific power that a muscle can produce, and are dependent on the proportion of myofibrils to non-contractile muscle components within the muscle (Pennycuick and Rezende, 1984). The function of a muscle is linked to the relative volume of these components (Lindstedt et al., 1998), non contractile components of a muscle include the sarcoplasmic reticulum and cellular components required for the conversion and supply of energy to the contractile elements. Sarcoplasmic reticulum releases Ca^{2+} that binds to the regulatory proteins of the myofibrils and allows cross-bridge cycling to occur. Muscles that operate at higher contracting frequencies must contract and relax rapidly and as such have a higher proportion of their volume occupied by sarcoplasmic reticulum. This reduces the available space for myofibrils and thus reduces the stress that can be produced. This is detrimental to force production, although a decline in power is not inevitable if there is an increase in strain rate that matches the decline in stress. The ultra structure of a muscle has a predictable and measurable effect on the force-velocity relationship.

3.2.3 Scaling of V_{max} and the force velocity relationship

The mechanical power output of a muscle is a product of its force and velocity. The maximal shortening velocity and maximal force that a muscle can produce are characteristically related, meaning that the peak power output that a muscle can achieve is defined and limited by the force-velocity relationship.

The force velocity relationship of a muscle can give clues about the intrinsic properties of a muscle and interactions between force, velocity and power and can help in teasing out the underlying limitations of locomotion bought about by muscle contraction. The maximum rate at which an unloaded muscle contracts isotonically is represented by it $V_{\max}$. $V_{\max}$ has previously been shown to scale inversely with increasing body size in muscles covering several species. $V_{\max}$ scaled as $M_b^{-0.084}$ in iliofibularis muscle of the lizard *Dipsosaurus* (Marsh, 1988), as $M_b^{-0.130}$ in fast fibres of several mammals (Seow and Ford, 1991) and as $M_b^{-0.084}$ in anuran sartorius muscle (Marsh, 1994). These results suggest that the scaling of $V_{\max}$ has an important impact on the scaling of locomotor performance in animals.

3.2.4 Scaling of deactivation rate

Muscles often contract cyclically during locomotion, the time taken for a muscle to be deactivated at the end of a contraction limits the rate at which a muscle can cycle (Marsh, 1990). The time required for Ca^{2+} to be released from and pumped back into the sarcoplasmic reticulum during a contraction means that muscles cannot activate and relax instantaneously. The result of this is that the net work performed by the muscle is reduced by both a reduction in the positive work generated during shortening (incomplete activation) and an increase in the work required to extend the muscle (due to activation prior to the muscle reaching peak length and incomplete relaxation). In the fast-twitch glycolytic region of the iliofibularis muscle of the lizard *Dipsosaurus* the time to peak twitch force increases with increasing body mass, scaling as $M_b^{0.190}$; stride frequency also scales as $M_b^{0.190}$, suggesting that activation time is matched to cycle frequency (Marsh, 1988).

In the previous chapter, the scaling of power output during escape swimming was quantified in bay scallops (*Argopecten irridians*), queen scallops, (*Argopecten opercularis*) and king scallops (*Pecten maximus*) using an *in vivo* method developed by Marsh (1992), in which water flow and intra-mantle pressure are simultaneously recorded during escape swimming (power = pressure x flow). The results revealed that muscle mass-specific average power decreased with increasing body mass, whilst work is constant as a result of constant stress and strain, whilst contraction frequency decreased with increasing body mass.

The scallop locomotor system is particularly good for determining scaling relationships between body mass and muscle power output, since all the power is produced by one muscle, the adductor muscle, and the ability to quantify its power output *in vivo*. However, uncertainties about eliciting maximal burst performance remain. To overcome this issue, in this Chapter the scaling of muscle power output with body mass was determined by studying the muscle *in vitro*. Using *in vitro* preparations, it is possible to elicit a maximal contraction in a supramaximally activated muscle, allowing for the scaling of contractile characteristics of the muscle that underlie its performance to be determined.

Operating frequency was the primary determinant of muscle power-output *in vivo*, this chapter asks whether the scaling of contractile characteristics matches the scaling of operating frequency. It was hypothesised that; (1) twitch contraction time would be proportional to cycle duration; (2) $V_{\max}$ would be proportional to cycle frequency; (3) the curvature of the force velocity relationship would be independent of body mass; (4) isotonic peak instantaneous power output scales as *in vivo* power output.

3.3 Materials and methods

3.3.1 Animals

Queen scallops (*Aequipecten opercularis*, Linnaeus 1758) were obtained from Loch Fyne, Tarbert, Scotland between January and March 2013 and maintained in artificial seawater (Instant Ocean, Aquarium Systems, Mentor, OH) at a temperature of 12^{o}C and a salinity of 34ppt. Scallops ranged in mass from 13.1 – 80.62g (n = 30). King scallops (*Pecten maximus*, Linnaeus 1758) were obtained from The Ethical Shellfish Company, Mull, Scotland in November 2015 and kept in artificial seawater at a temperature of 10^{o}C and a salinity of 34ppt, with a mass range of 139.25 – 372.45g (n = 19). Bay scallops (*Argopecten irradians*, Lamarck 1819) were obtained from The Marine Resources Center of the Marine Biological Laboratory, Woods Hole, MA from Nantucket Sound off the southern coast of Cape Cod in July 2015, before being transported to Wellesley College, USA where they were kept in artificial seawater at 15 ^{o}C and a salinity of 34ppt, with a mass range of 13.1 – 80.62g *(n* = 21). All scallops were housed at a temperature and salinity that corresponded to the conditions in which the scallops would have been under before collection from their respective habitats. Scallops were allowed to acclimate to the laboratory conditions for at 2 days before experiments took place.

3.3.2 Muscle preparation

Contractile properties were measured on a bundle of muscle fascicles dissected from the central portion of the adductor muscle along its anterior edge. The anterior edges of both valves were cut away (Dremel Multipro cutting tool, Dremel, Racine, Wisconsin, USA), revealing the anterior most part of the adductor muscle and other soft tissues of the animal. The soft parts of the animal were then carefully dissected away leaving only the adductor muscle and the attached valves. The closed length (L_{cl}) of the adductor muscle along its anterior edge was measured using a pair of digital callipers whilst the valves were held closed. The dorsal, ventral and posterior sides of the adductor muscle together with the smooth muscle were dissected away, leaving a bundle of muscle fascicles (approximately 25mm^2) of the striated adductor muscle attached to the valves. The valves were subsequently cut around the bundle, leaving small portions of the shell attached at each end of the muscle that facilitated attachment to the muscle ergometer and the base of the muscle chamber. The scallop was regularly irrigated with chilled (~3°C) artificial seawater during the dissection. Following dissection, the muscle preparation was attached to the bottom of a Perspex chamber using a stainless steel clip on either side of the muscle to secure the lower valve in place. The upper valve was attached to the arm of an ergometer (model 300B-LR, Aurora Scientific, London, Ontario, Canada) via a harness fashioned from a lightweight silver chain. The entire muscle preparation was then suspended in a bath of either temperature-controlled Ringer's solution (440mmoll^{-1} NaCl, 10mmoll^{-1} KCl, 14mmoll^{-1} $MgSO_4$, 30mmoll^{-1} $MgCl_2$, 10mmol l^{-1} $CaCl_2$, 20mmoll^{-1} imidazole, pH7.9; Olson and Marsh 1993), or artificial seawater. In both instances the solutions were saturated with 100% oxygen. Experiments using muscles from queen scallops took place at 12 °C, king scallops at 10°C whilst bay scallop preparations were kept at 15 °C and matched both the temperature at which the animals had previously been housed and the temperature at which the escape swimming experiments had been performed (Chapter 2).

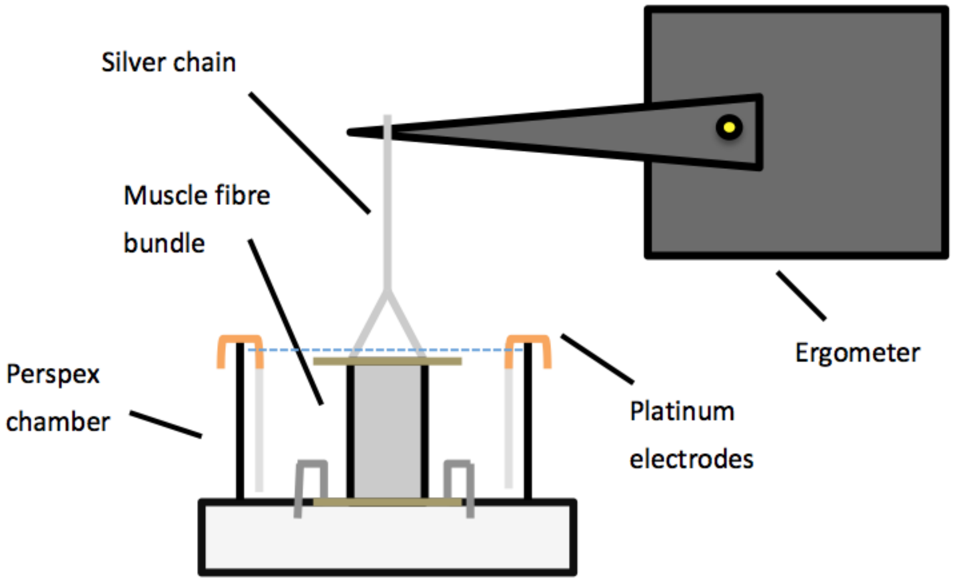

Figure 3.1. Schematic showing dissected scallop adductor muscle within the muscle rig set-up.

Muscles were activated using supramaximal stimuli (0.5 ms pulse width) generated using a stimulator (S48; Grass, West Warwick, RI, USA), amplified using a stimulus isolation unit (UISO model 236; Hugo Sachs Elektronik, March-Hugstetten, Germany) and delivered through field stimulation via parallel platinum plate electrodes running the length of the muscle. Muscle force and muscle length were recorded at 5000 Hz *via* a 12 bit A/D converter (DAS-1801AO; Keithley Metrabyte, Cleveland, OH, USA) using a personal computer.

3.3.3 Isometric contractile properties

Following dissection, the muscle preparation was held at a length of $1.3L_{\mathrm{cl}}$ for a period of 1 hour in order to recover from the dissection process (following Olson and Marsh, 1993). The muscle length was increased to $1.4L_{\mathrm{cl}}$ (L_0) prior to experiments taking place. At $1.4L_{\mathrm{cl}}$ twitch force is maximal (Olson and Marsh, 1993) and this length is also the typical maximum extended relative muscle length at maximum gape during escape swimming (Chapter 2). Maximal stimulus voltage was set to that at which maximal force was obtained during isometric twitch contractions. Isometric tetanic contractions were elicited using a train of stimuli of 200-600ms delivered at a stimulation frequency of 50 Hz. A period of approximately 5 minutes was allowed between all twitch and tetanic contractions to allow some recovery. Peak twitch force (P_{tw}), time to peak force (*t*Ptw), and time to 50% relaxation (*t*0.5r) were recorded for each isometric twitch. Peak isometric tetanic force (P_0) was also recorded for each isometric tetanus.

3.3.4 Isotonic contractile properties

To determine the force-velocity relationship, muscle fascicle bundles were subjected to a series of after-loaded isotonic contractions using a stimulation frequency of 50 Hz. Force and length were recorded as previously described. Force was expressed relative to P_0, with the length change being differentiated with respect to time to determine velocity. To assess any decline in the preparation, a control isometric contraction was performed after every three isotonic contractions. A linear decline was assumed between control contractions and used to estimate P_0 corresponding to each isotonic contraction. The control contraction differed between the different species of scallops. In queen scallops, an isometric tetanic contraction was used as the control. In king and bay scallops an isometric twitch was used as the control because it was frequently found in initial experiments that the muscle fascicle bundle tore during tetanic contractions. In these species an isometric twitch and an isometric tetanus were performed at the end of the experiment and the twitch:tetanus ratio from these contractions used to estimate P_0 at the start of the experiment.

Following the contractile measurements, the two remaining pieces of shell and any damaged fascicles not running between the two valves were dissected away and the blotted mass of the muscle preparation was obtained.

3.3.5 Statistical analysis

Statistical analysis was carried out using Igor Pro (Version 6.37, WaveMetrics, Lake Oswego, OR). Statistical significance was accepted at the 0.05 level. Scaling relationships were analysed using ordinary-least squares regressions, which allowed for any statistically significant relationships between two variables to be determined (*F*-test).

The force velocity data were described by fitting the three-parameter hyperbolic-linear equation of Marsh and Bennett (1986):

$$V = [B(1 - P/P_0)/(A+P/P_0)]+C(1 - P/P_0) \qquad [3.1]$$

where V is the velocity of shortening in muscle lengths per second ($L_0\ s^{-1}$) and P/P_0 is the relative force generated. B and C are constants and have the dimension of velocity and A is dimensionless constant. Curves were fitted using the non-linear curve fitting procedure in Igor Pro (Version 6.37, WaveMetrics, Lake Oswego, OR).

The scaling of isotonic and isometric contractile properties were plotted as a function of body mass and are the main focus in this chapter. Variables were also plotted against muscle mass for comparison. Due to *in vivo* and *in vitro* measurements being taken from the same animals in bay scallops isotonic and isometric contractile characteristics were also plotted against *in vivo* cycle frequency to explore how changes in cycle frequency affected the scaling of these measurements.

3.4 Results

Table 3.1. Allometric relationships ($y = aM_b^b$; M_b in g) of body and muscle morphology in *A. irradians* (n = 21), *A. opercularis* (n = 30) and *P.maximus* (n = 19).

y	units	species	r^2	*a*	*b (±95%CI)*	*P*
L_{ap}	mm	*A. irradians*	0.96	14.52	0.407 (±0.018)	<0.001
		A. opercularis	0.96	18.20	0.337 (±0.026)	<0.001
		P.maximus	0.95	18.80	0.351 (±0.018)	<0.001
L_{dv}	mm	*A. irradians*	0.96	15.49	0.371 (±0.029)	<0.001
		A. opercularis	0.97	19.03	0.321 (±0.013)	<0.001
		P.maximus	0.93	16.74	0.349 (±0.021)	<0.001
L_{sh}	mm	*A. irradians*	0.95	6.34	0.389 (±0.026)	<0.001
		A. opercularis	0.94	5.22	0.396 (±0.023)	<0.001
		P.maximus	0.81	4.82	0.346 (±0.075)	<0.001
M_m	g	*A. irradians*	0.85	0.07	0.990 (±0.114)	<0.001
		A. opercularis	0.75	0.03	1.008 (±0.334)	<0.001
		P.maximus	0.91	0.02	1.389 (±0.197)	<0.001
L_0	mm	*A. irradians*	0.89	7.10	0.416 (±0.066)	<0.001
		A. opercularis	0.92	6.50	0.391 (±0.045)	<0.001
		P.maximus	0.86	4.05	0.426 (±0.077)	<0.001
A_m	mm^2	*A. irradians*	0.90	0.66	1.312(±0.122)	<0.001
		A. opercularis	0.85	0.43	1.399 (±0.230)	<0.001
		P.maximus	0.94	0.06	1.815 (±0.195)	<0.001

L_{ap}, anterior-posterior shell length.

L_{dv}, dorsal ventral shell length.

L_{sh}, shell height.

M_m, muscle mass.

L_{max}, maximum muscle length during swimming.

A_m, muscle cross sectional area

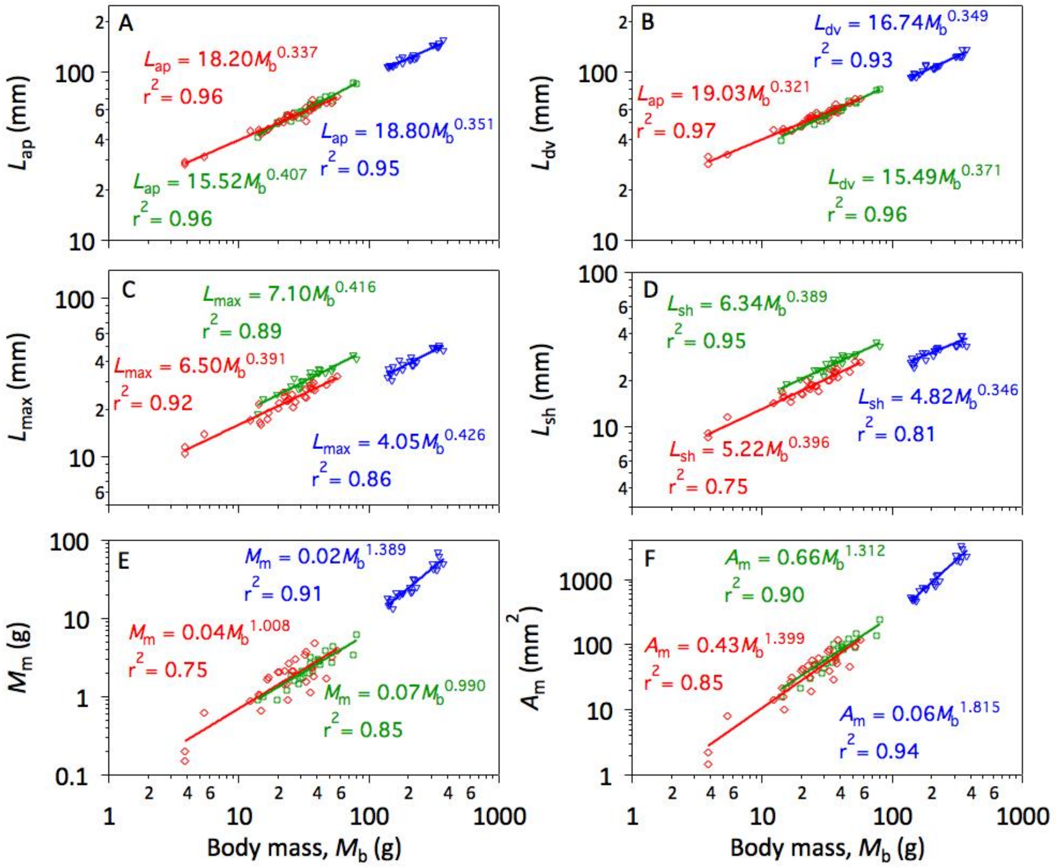

Figure 3.2. The scaling of morphology with body size in scallops. In *A. irradians*, (green squares), *A. opercularis* (red diamonds) and *P. maximus* (blue triangles). The scaling of shell anterior-posterior length (A), shell dorsal ventral length (B), maximum muscle length (C), shell height (D), muscle mass (E) and muscle cross sectional area (F) as a function of body size.

3.4.1 Scaling of morphology

Body mass covered a 6-fold range in bay scallops (13.10-80.62g), a 15-fold range in queen scallops (3.85-56.83g), and a 3-fold range in king scallops (193.25-373.45g). The scaling of morphological variables for the three species of scallops are presented in Table 3.1 and figure 3.2. The scaling exponents were broadly similar to those measured in chapter 2. Muscle mass scaled approximately isometrically in bay scallops and queen scallops, but was found not to scale isometrically in king scallops, with larger king scallops having relatively larger adductor muscles (fig. 3.1E). Larger scallops also had proportionally larger muscle cross sectional areas than smaller ones, scaling with body mass with an exponent ranging from 1.3 (bay scallops) to 1.8 (king scallops) (fig. 3.1F).

Table 3.2. Allometric relationships ($y = aM_b^b$; M_b in g) of isometric contractile properties and body mass in *A. irradians*, *A. opercularis* and *P.maximus*.

y	units	species	r^2	*a*	*b* (±95%CI)	*P*
P_0	kN m^{-2}	*A. irradians*	0.003			NS
		A. opercularis	0.02			NS
		P.maximus	0.08			NS
P_{tw}: P_0		*A. irradians*	0.29	1.33	-0.192 (±0.071)	<0.01
		A. opercularis	0.02			NS
		P.maximus	0.15			NS
*t*Ptw	ms	*A. irradians*	0.004			NS
		A. opercularis	0.26	27.49	0.274 (±0.010)	<0.01
		P.maximus	0.19	39.60	0.113 (±0.054)	<0.05
*t*0.5r	ms	*A. irradians*	0.12			NS
		A. opercularis	0.24	30.32	0.273 (±0.094)	<0.01
		P.maximus	0.03			NS
t_c	ms	*A. irradians*	0.06			NS
		A. opercularis	0.29	59.39	0.274 (0.093)	<0.01
		P.maximus	0.15			NS

P_0, maximal isometric tetanic force.

P_{tw}: P_0, twitch-tetanus ratio.

*t*Ptw, time from onset to peak tension during twitch.

*t*0.5r, time from peak tension during twitch to 50% relaxation.

t_c, twitch contraction time (*t*Ptw + *t*0.5r).

Table 3.3. Allometric relationships ($y = aM_m^b$; M_m in g) of isometric contractile properties and muscle mass in *A. irradians*, *A. opercularis* and *P.maximus*.

y	units	species	r^2	*a*	*b* (±95%CI)	*P*
P_0	kN m^{-2}	*A. irradians*	0.02			NS
		A. opercularis	0.01			NS
		P.maximus	0.12			NS
P_{tw}: P_0		*A. irradians*	0.11			NS
		A. opercularis	0.11			NS
		P.maximus	0.22	1.23	-0.268 (±0.237)	<0.05
*t*Ptw	ms	*A. irradians*	0.09			NS
		A. opercularis	0.10			NS
		P.maximus	0.34	48.79	0.128 (±0.085)	<0.01
*t*0.5r	ms	*A. irradians*	0.01			NS
		A. opercularis	0.02			NS
		P.maximus	0.03			NS
t_c	ms	*A. irradians*	0.02			NS
		A. opercularis	0.11			NS
		P.maximus	0.19			NS

P_0, maximal isometric tetanic force.

P_{tw}: P_0, twitch-tetanus ratio.

*t*Ptw , time from onset to peak tension during twitch.

*t*0.5r, time from peak tension during twitch to 50% relaxation.

t_c, twitch contraction time (*t*Ptw + *t*0.5r).

Table 3.4. Allometric relationships ($y = aM_b^b$; M_b in g) of isotonic contractile properties and body mass in *A. irradians*, *A. opercularis* and *P.maximus*.

y	units	species	r^2	a	b (±95%CI)	P
V_{max}	L_0 s^{-1}	*A. irradians*	0.41	11.90	-0.160(±0.046)	<0.01
		A. opercularis	0.46	10.53	-0.226 (±0.062)	<0.01
		P.maximus	0.76	43.20	-0.364 (±0.186)	<0.01
R_{Π}		*A. irradians*	0.22	0.25	-0.202 (±0.097)	<0.01
		A. opercularis	0.27	0.22	-0.119 (±0.044)	<0.05
		P.maximus	0.03			NS
Π_{max}	W kg^{-1}	*A. irradians*	0.46	546.57	-0.334 (±0.081)	<0.001
		A. opercularis	0.27	281.19	-0.43 (±0.210)	<0.05
		P.maximus	0.80	15173	-0.929 (±0.507)	<0.01
Force at Π_{max}	P/P_0	*A. irradians*	0.05			NS
		A. opercularis	0.01			NS
		P.maximus	0.06			NS
V/V_{max}	L_0 s^{-1}	*A. irradians*	0.21	0.52	-0.161 (±0.068)	<0.05
		A. opercularis	0.29	0.51	-0.146 (±0.053)	<0.05
		P.maximus	0.01			NS

V_{max}, maximum shortening velocity against zero load.

R_{Π}, power ratio calculated as $\Pi_{max} / V_{max}\, P_0$.

Π_{max}, maximum isotonic power.

V/V_{max}, optimal shortening velocity for Π_{max}.

Table 3.5. Allometric relationships ($y = aM_m^b$; M_m in g) of isotonic contractile properties and muscle mass in *A. irradians*, *A. opercularis* and *P.maximus*.

y	units	species	r^2	*a*	*b* (±95%CI)	*P*
V_{max}	L_0 s^{-1}	*A. irradians*	0.27	7.43	-0.115(±0.089)	<0.05
		A. opercularis	0.34	5.72	-0.166 (±0.108)	<0.01
		P.maximus	0.68	12.68	-0.222 (±0.141)	<0.05
Power Ratio		*A. irradians*	0.13			NS
		A. opercularis	0.24	0.16	-0.087 (±0.076)	<0.05
		P.maximus	0.02			NS
Π_{max}	W kg^{-1}	*A. irradians*	0.49	192.08	-0.301 (±0.0147)	<0.001
		A. opercularis	0.17			NS
		P.maximus	0.82	818.06	-0.630 (±0.308)	<0.05
Force at Π_{max}	P/P_0	*A. irradians*	0.01			NS
		A. opercularis	0.01			NS
		P.maximus	0.03			NS
V/V_{max}	L_0 s^{-1}	*A. irradians*	0.20	0.33	-0.128 (±0.123)	<0.05
		A. opercularis	0.16			NS
		P.maximus	0.01			NS

V_{max}, maximum shortening velocity against zero load.

R_{Π}, power ratio calculated as $\Pi_{max} / V_{max} P_0$.

Π_{max}, maximum isotonic power.

V/V_{max}, optimal shortening velocity for Π_{max}.

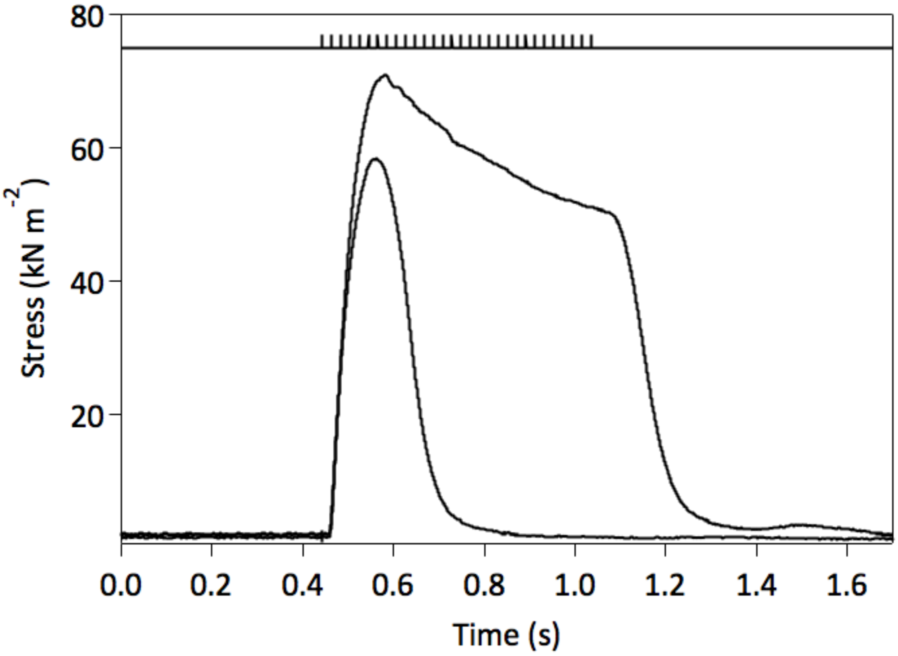

Figure 3.3. Representative twitch and tetanic contractions obtained from the adductor muscle of *Aequipecten opercularis*. Stimulation occurs at 0.442 seconds. A single stimulus elicits a twitch whereas repeated stimuli at a frequency of 50 Hz were used to produce a tetanic contraction. In this instance the tetanic contraction was achieved via stimulation lasting 600ms, represented by the hatched line.

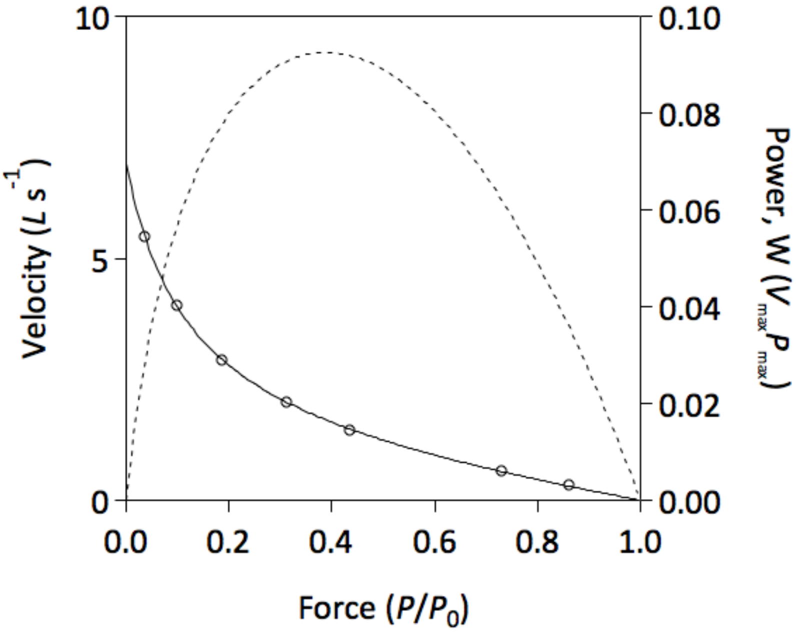

Figure 3.4. Representative force-velocity (solid line) and force-power (dotted line) relationship obtained from the adductor muscle of the scallop *A. opercularis*. Data were obtained from a preparation of isolated muscle fibres at 12°C and fitter to the HYP-LIN equation.

3.4.2 Isometric contractile properties

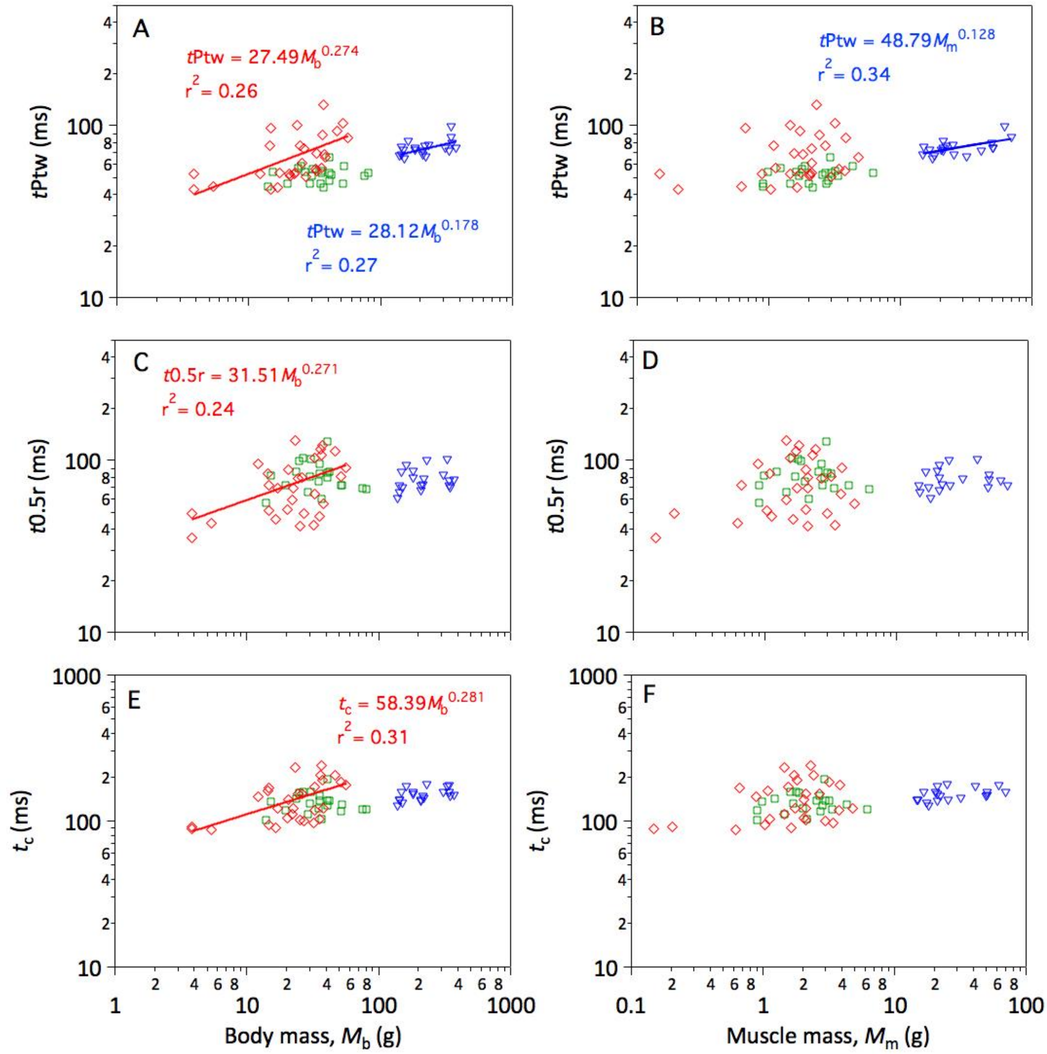

Figure 3.5. Relationship between time dependent properties of twitch contractions and body and muscle mass in scallops. *A. irradians*, (green squares), *A. opercularis* (red diamonds) and *P. maximus* (blue triangles). The time from onset to peak twitch tension (A); time from peak twitch tension to half relaxation time (B); twitch contraction time (C).

Twitch rise time (*t*Ptw) increased with increasing body mass in both queen and king scallops, scaling as $M_b^{0.274}$ (queen scallops, *n*=30) and $M_b^{0.112}$ (king scallops, *n*=19) (fig. 3.5A). However, there was no scaling relationship between twitch rise time and body mass in bay scallops (*n*=21) (*t*Ptw = 51.01±1.15ms). Twitch rise time increased with increasing muscle mass in king scallops (α $M_m^{0.112}$), but was independent of muscle mass in bay and queen scallops (queen, *t*Ptw = 67.07±4.04ms; fig. 3.5B). Time from peak twitch force to 50% relaxation (*t*0.5r) increased with increasing body mass in queen scallops, scaling as $M_b^{0.273}$, but did not in either bay scallops (*t*0.5r 87.97±5.78ms) or king scallops (*t*0.5r 79.85±2.24ms) (fig. 3.5C). Time from peak twitch force to 50% relaxation was independent of muscle mass in all three species (queen t0.5r = 73.59±5.00ms; fig 3.5D). Twitch contraction time (t_c) scaled as $M_b^{0.274}$ in queen scallops, but was not found to scale with body mass in bay scallops (t_c 96.99±3.57ms) or king scallops (t_c 152.32±2.63ms) (fig. 3.5E). Twitch contraction time was independent of muscle mass in all three species (queen t_c = 140.67±8.28ms; fig. 3.5F).

During isometric tetanic contractions the adductor muscles of the scallops did not maintain a force plateau (as has previously been observed in scallop adductor muscle; Rall, 1981; Olson and Marsh, 1993). Isometric tetanic stress was found not to scale with body mass or muscle mass in any of the species studied. Mean stresses were 198.46 ±8.6 kN m^{-2} in bay scallops, 101.93 ±10.17 kN m^{-2} in queen scallops and 116.26 ±7.73 kN m^{-2} in king scallops (Table 3.2). In bay scallops, the twitch tetanus ratio decreased with increasing body mass, scaling as $M_b^{-0.192}$, however, in queen and king scallops the twitch:tetanus ratio was constant (queen scallops 0.68±0.03; king scallops 0.51±0.03; Table 3.2). In king scallops, the twitch tetanus ratio decreased with increasing muscle mass, scaling as $M_m^{-0.268}$, however, in bay and queen scallops the twitch:tetanus ratio as a function of muscle mass was constant (bay scallops 0.68±0.02, Table 3.3)

3.4.3 Isotonic contractile properties

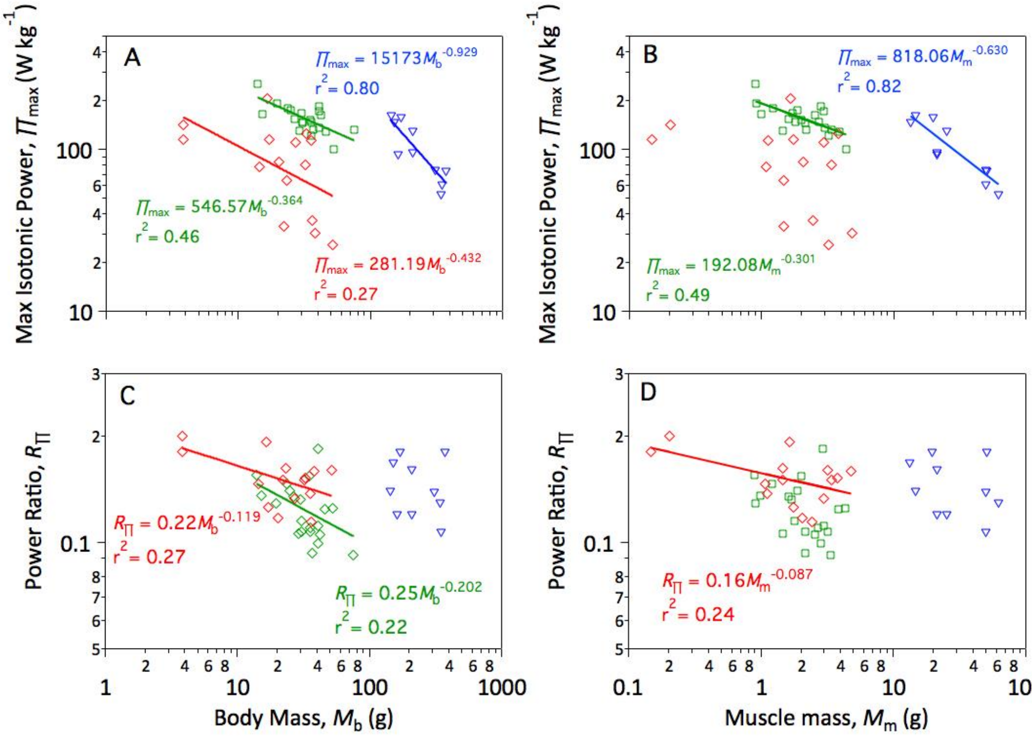

Figure 3.6. Isotonic contractile properties as a function of body and muscle mass in scallops. Maximal isotonic power (A, B) and power ratio (C,D) as a function of body and muscle mass in *A. irradians*, (green squares), *A. opercularis* (red diamonds) and *P. maximus* (blue triangles).

Force-velocity relationships were determined for all three species of scallops: king scallops (*n*=10), queen scallops (*n*=15) and bay scallops (*n*=21). Maximum isotonic power decreased with increasing body mass in all three species studied, scaling as $M_b^{-0.364}$ in bay scallops, $M_b^{-0.432}$ in queen scallops and $M_b^{-0.929}$ in king scallops (fig. 3.6A). Maximum isotonic power decreased with increasing muscle mass in bay scallops (α $M_m^{-0.301}$) and in king scallops (α $M_m^{-0.630}$), but was independent of muscle mass in queen scallops (Π^* = 90.42±12.74 W kg^{-1}; fig. 3.6B). The power ratio, which describes the degree of curvature of the force velocity relationship (Marsh and Bennett, 1985), scaled with body mass in the bay scallops and queen scallops. The power ratio decreased (force-velocity relationship more curved) as body mass increased in bay scallops and queen scallops, scaling as $M_b^{-0.202}$ (bay scallops) and $M_b^{-0.119}$ (queen scallops). However, the power ratio in king scallops did not scale with body mass (R_Π = 0.16±0.01; fig. 3.6C). The power ratio decreased with increasing muscle mass in queen scallops (α $M_m^{-0.087}$), but did not scale with body mass in king or bay scallops (bay scallops, R_{Π} = 0.12±0.01; fig. 3.6D).

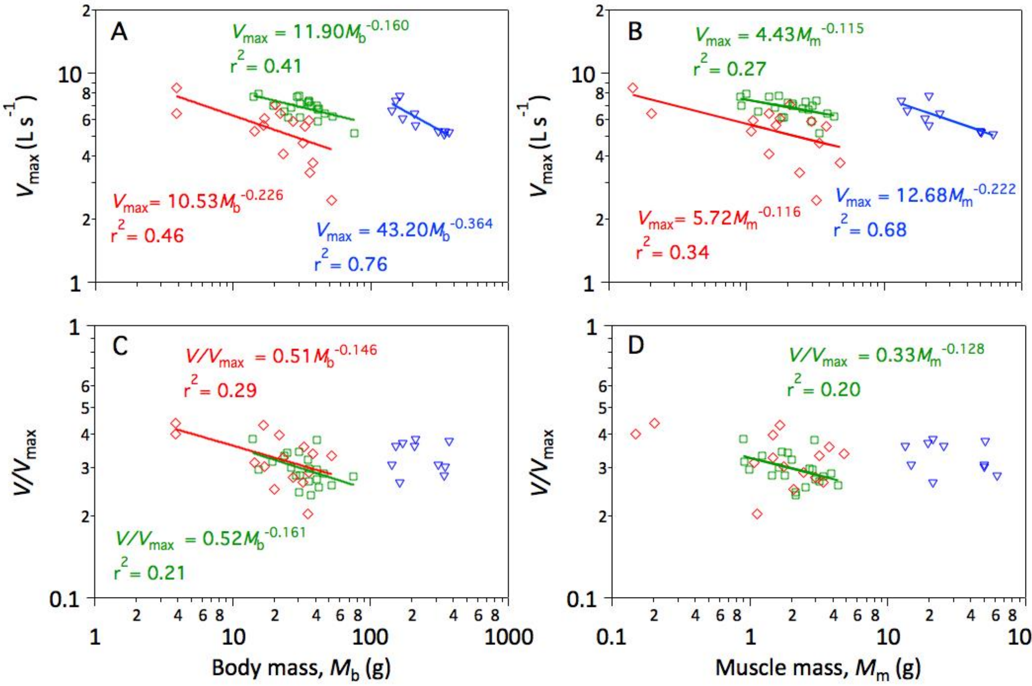

Figure 3.7. Isotonic contractile properties as a function of body and muscle mass in scallops. V_{max} (A,B) and relative shortening velocity (C,D) as a function of body and muscle mass in *A. irradians*, (green squares), *A. opercularis* (red diamonds) and *P. maximus* (blue triangles).

V_{max} decreased with increasing body mass in bay, queen and king scallops, scaling as $M_b^{-0.160}$, $M_b^{-0.226}$ and $M_b^{-0.364}$ respectively (fig. 3.7A). Similarly, V_{max} decreased with increasing muscle mass in bay (α $M_m^{-0.115}$), queen (α $M_m^{-0.116}$) and king scallops (α $M_m^{-0.222}$; fig. 3.7B). The relative force (P/P_0) at which maximum power was produced was independent of both body and muscle mass in all three species of scallop (0.42±0.01 in bay scallops; 0.45±0.01 in queen scallops and 0.46±0.01 in king scallops; Table 3.4, 3.5). The relative shortening velocity (V/V_{max}) at which muscles produced maximal power decreased with increasing body mass in bay scallops and queen scallops (bay scallops $M_b^{-0.161}$ and queen scallops $M_b^{-0.146}$), but did not scale with body mass in king scallops, (V/V_{max} = 0.35±0.02) (fig. 3.7C). Relative shortening velocity decreased with increasing muscle mass in bay scallops (α $M_m^{-0.128}$), but was independent of muscle mass in king scallops and queen scallops (queen scallops, V/V_{max} = 0.33±0.02).

Table.3.6 Allometric relationships ($y = af^b$; f in Hz) between i*n vitro* contractile characteristics in bay scallops in relation to cycle frequency.

y	units	r^2	a	b (±95%CI)	P
P_0	kN m^{-2}	0.09			NS
P_{tw}: P_0		0.61	1.41	-0.211 (±0.15)	<0.001
tP_{tw}	ms	0.01			NS
*t*0.5r	ms	0.10			NS
t_c	ms	0.07			NS
V_{max}	L_0 s^{-1}	0.25	11.90	-0.160(±0.046)	<0.05
Power Ratio		0.43	0.25	-0.202 (±0.097)	<0.01
P_{max}	W kg^{-1}	0.05			NS
Force at P_{max}	P/P_0	0.31	0.31	0.287 (±0.133)	<0.05
V/V_{max}	L_0 s^{-1}	0.01			NS

In eighteen of the bay scallops, both cycle frequency during swimming and *in vitro* contractile characteristics were obtained from the same animal. In these individuals, isometric force, twitch rise, half relaxation and contraction time were independent of cycle frequency. The twitch:tetanus ratio decreased with increased cycle frequency, scaling as $f^{-0.211}$. V_{max} decreased with increased cycle frequency, scaling as $f^{-0.160}$, whilst the power ratio also decreased with increased cycle frequency, scaling as $f^{-0.202}$. Maximum isotonic power and V/V_{max} were found to be independent of cycle frequency. The relative force at maximum power output increased with increased cycle frequency, scaling as $f^{0.287}$ (table 3.6).

3.5 Discussion

During escape swimming in scallops, muscle mass-specific power decreased with increasing body mass (Chapter 2). The aim of these experiments was to determine whether this scaling relationship reflects limitations of the muscle power underlying the locomotion and scaling of the muscle's contractile characteristics.

3.5.1 Scaling of muscle mass-specific power *in vitro*

Maximal isotonic power decreased with increased body mass in all three scallop species, scaling as $M_b^{-0.364}$ (bay scallops), $M_b^{-0.432}$ (queen scallops) and $M_b^{-0.929}$ (king scallops). However, the scaling exponents for maximum isotonic power output with body mass were steeper than and did not lie within the 95% confidence limits of the exponents for both average and peak instantaneous power output during *in vivo* swimming (average muscle mass-specific power α $M_b^{-0.266}$ in bay scallops, α $M_b^{-0.266}$ in queen scallops and α $M_b^{-0.150}$ in king scallops; peak instantaneous muscle mass-specific power α $M_b^{-0.203}$ in bay scallops, α $M_b^{-0.313}$ in queen scallops and α $M_b^{-0.145}$ in king scallops; Chapter 2). Maximum isotonic muscle power output in the hindlimb muscles of anurans (interspecific) and lizard iliofibularis muscle (intraspecific) also decreases with increasing body mass, scaling α $M_b^{-0.100}$ in anurans (Marsh, 1994) and α $M_b^{-0.070}$ in lizards (Marsh, 1988). The interspecific scaling of maximum isotonic power measured in frogs compares with a body-mass independence of *in vivo* power estimated from jump distance (Marsh, 1994). Therefore it appears that the scaling of power during locomotion is only partially explained by the scaling of maximum isotonic power; larger scallops and frogs generate relatively more power *in vivo* than their smaller counterparts based on the scaling expected from their maximum isotonic power. The difference between the scaling of *in vivo* and *in vitro* power found in scallops may be because the isotonic contractions that the muscles undergo during the force velocity experiments do not accurately replicate the types of load that the muscles experience during locomotion, nor do they simulate the periods of incomplete muscle activation that occur *in vivo* as the muscle is activated and relaxes. Perhaps the scaling of a different contractile characteristic may provide an explanation.

3.5.2 Maximum shortening velocity and cycle frequency

Hill (1950) proposed that natural selection would have resulted in muscles possessing contractile properties that would best suit the functions that the muscle would be undergoing *in vivo*. As such, during natural movements, muscles would be operating at a shortening rate optimised for maximum power output and efficiency. Hill's model predicts that V_{max} will be directly proportional to the frequency of contraction. Hill assumed geometric similarity, resulting in the predication that V_{max} will be proportional to $M_{\mathrm{b}}^{-0.333}$ (Hill, 1950), whereas McMahon's elastic similarity predicts V_{max} will scale as $\mathrm{M}_{\mathrm{b}}^{-0.125}$ (McMahon, 1973). V_{max} scaled negatively with increasing body size in bay, queen and king scallops, scaling as $M_{\mathrm{b}}^{-0.160}$, $M_{\mathrm{b}}^{-0.226}$ and $M_{\mathrm{b}}^{-0.364}$, respectively. V_{max} scaled with a scaling exponent greater than that of cycle frequency (approximately $\alpha M_{\mathrm{b}}^{-0.125}$) in these animals (Fig. 2.4; Chapter 2), suggesting that the scaling of V_{max} was not the sole determinant of the scaling cycle frequency in these animals. Previous studies on the scaling of V_{max} in similarly fast-muscles have demonstrated that inter-specifically V_{max} scales as $\mathrm{M}_{\mathrm{b}}^{-0.070}$ (based on data from two species covering a 1200-fold mass range; Rome et al., 1990) and ontogenetically as $\mathrm{M}_{\mathrm{b}}^{-0.070}$ (in *Dipsosaurus* iliofibularis muscle; Marsh, 1988). In both studies, the scaling exponent of V_{max} with body mass was lower than the scaling exponent of stride frequency with body mass (stride frequency $\alpha M_{\mathrm{b}}^{-0.150}$ at the trot-gallop transition, Heglund and Taylor, 1988; stride frequency $\alpha M_{\mathrm{b}}^{-0.200}$ in *Dipsosaurus*, Marsh, 1988), indicating that the intrinsic shortening velocity of a muscle is not the sole determinant of stride frequency. This theory is supported by experiments in which temperature was manipulated to determine its effects on contractile properties of skeletal muscles in lizards (Marsh and Bennett, 1985, 1986a, b). During these experiments large changes in temperature affected shortening velocity much more dramatically than stride frequency, revealing a lack of correspondence that would not be present if intrinsic shortening velocity was the sole determinant of frequency. There could be several reasons for the differences in the scaling of V_{max} and frequency with body mass. In bay and queen scallops the power ratio also scaled with body mass. The power ratio represents the shape of the force-velocity relationship, with a value 0.25 representing a straight line. Previous work on the scaling of the power ratio during isotonic contractions in *Dipsosaurus* iliofibularis muscle found little evidence of a relationship between body size and curvature (Marsh, 1988). However, in bay and queen scallops, larger animals were found to have a more curved force-velocity relationship, with the power ratio scaling as $M_{\mathrm{b}}^{-0.202}$ and $M_{\mathrm{b}}^{-0.119}$ (Table 3.4). As a result of the scaling of power ratio, the optimal shortening velocity (V/V_{max}) was also found to scale with body mass, scaling as $\mathrm{M}_{\mathrm{b}}^{-0.161}$ and $\mathrm{M}_{\mathrm{b}}^{-0.146}$ (Fig. 3.7C); these scaling exponents are similar to those for the scaling of clapping frequency with body mass indicating that V/V_{max} may be a better indicator of muscle operating frequency than V_{max}. However, the actual shortening velocity of the adductor muscle was determined *in vivo* during swimming (Chapter 2) enabling swimming V/V_{max} to be calculated. Based on the scaling of *in vivo* shortening velocity and V_{max}, the *in vivo* V/V_{max} can be estimated. In bay scallops the *in vivo* V/V_{max} is approximately constant (0.15 to 0.16) and much lower than that found to be optimal (Fig. 3.7C). Whereas in bay scallops the *in vivo* V/V_{max} increases with body mass (range 0.36 in 40 g animal to 0.50 in 400 g animal), increasing from a value that is optimal *in vitro* in small animals to a value higher than is optimal *in vitro* in larger animals (Fig. 3.7C). In king scallops *in vivo* V/V_{max} also increases with body mass (range 0.08 in 40 g animal to 0.22 in 400 g animal), with values that are consistently below optimal *in vitro* conditions, but get closer to optimal as size increases (Fig. 3.7C). This further indicates that the rather prescribed conditions under which many contractile measurements are made *in vitro* may not reflect *in vivo* performance particularly well. Therefore, while the force-velocity relationship is useful for characterising the contractile properties of muscle in a comparative manner, muscles rarely if ever operate isotonically *in vivo* which may lead to the lack of direct correspondence between V_{max} and stride frequency and between *in vivo* V/V_{max} and *in vitro* optimal V/V_{max}.

In summary, in queen scallops and bay scallops, the negative scaling of maximum isotonic power output with body mass is determined by the combination of a scaling of V_{max} and a scaling of the V/V_{max} for maximum power (determined by the curvature of the force-velocity relationship) with body mass. The maximum isometric force and the P/P_0 for maximum power are constant and have no bearing on the scaling of maximum isotonic power. Similar trends (though non-significant) in king scallops result in a similar negative scaling of maximum isotonic power with body mass (Fig. 3.6A).

3.5.3 Kinetics of isometric twitches and their implications for muscle operating frequency

Muscles that perform cyclical contractions must be alternately activated and deactivated. In order to maximise the work done by the muscle and to minimise the work done on the muscle force must be generated predominantly during shortening and negligibly during lengthening. Therefore perhaps not surprisingly, there is a strong correlation between twitch kinetics and the operating frequency of the muscle; this is observed both intraspecifically (quail pectoralis; Askew and Marsh, 2002) and ontogenetically (lizard iliofibularis, Marsh, 1988). In these experiments the clapping frequency during swimming was only measured in some animals; where data are available (bay scallops; Table 3.6) there was no significant relationship between twitch kinetics and cycle frequency. Twitch kinetics did slow with increasing body mass in queen scallops, however, the scaling relationship was steeper than the relationship between frequency and mass (twitch times α $M_b^{-0.274}$ compared with frequency α $M_b^{-0.122}$, Fig. 2.4). In the other species of scallop there was a similar trend but the relationships were not significant. There are several potential reasons for the absence of a scaling relationship between twitch kinetics and body mass in king and bay scallops. The first is that in king scallops the size range of animals was rather small (193.25-373.45g); however, this was not the case for bay scallops (13.10-80.62g). A second factor could be the scaling of muscle length trajectory with body mass. The proportion of the cycle spent shortening (τ) decreased with increasing body mass (Fig. 2.6) resulting in only a slight scaling of shortening duration with body mass (α $M_b^{0.080}$). It is perhaps this change in muscle length trajectory resulting in relatively small differences in shortening duration that leads to non-significant scaling of twitch kinetics with body mass. Thirdly, the kinetics of activation and deactivation depend on the rates of lengthening and shortening, respectively, with higher rates of activation and deactivation with increasing strain rate (Askew and Marsh, 1998). The relationship between isometric twitch kinetics and the kinetics of activation and deactivation during a dynamic contraction are unknown, and therefore it is unclear whether a strong correlation between isometric twitch kinetics and body mass is expected. Fourth, the mechanical function of the scallop adductor muscle is clear – the muscle must generate mechanical power – however, the mechanical function of the lizard iliofibularis muscle (Marsh, 1988) has not been measured. The scaling of a muscle’s contractile properties may be related to its mechanical function and, therefore, caution is warranted when comparing muscles with differing or unknown mechanical functions.

3.5.4 Summary

This investigation was conducted to characterise the scaling of *in vitro* muscle power output in scallops, and to try to determine the physiological reasons for the scaling of contraction frequency in scallops, and the influence it had on muscle-mass specific power. Muscle mass-specific power output measured *in vitro* scaled negatively with body mass, with scaling exponents greater than those measured *in vivo*. The force-velocity relationship changed with increasing body mass in scallops, with larger scallops typically exhibiting a more curved force-velocity relationship resulting in a higher $V/V_{\max}$ and lower values of $V_{\max}$. The changes in the force-velocity relationship explain the scaling of maximum isotonic power with body mass, however, other factors must also be important since the scaling exponents for *in vivo* and *in vitro* power with body mass differ. Twitch kinetics are clearly important during dynamic contractions but have no bearing on the force-velocity relationship and the measurement of isotonic power. The isometric twitch kinetics did vary with body mass in queen scallops but not in bay or king scallops, however, as noted above the rate of activation and deactivation are influenced by strain rate and how this scales with body mass is unknown. It is clear that the contractile properties of the muscle are tuned to the *in vivo* operating conditions resulting in a constancy of strain and mean stress during swimming. Hill (1950) predicted that muscle stress and strain would be constant with changes in body mass. As demonstrated in scallops during escape swimming (Chapter 2) he was correct. However, the *in vitro* contractile properties of the muscle measured here, suggest that the situation is more complex than he considered with twitch kinetics not relating directly to operating frequency and shifts in the force-velocity relationship with changing body mass.

Chapter 4

Jet wake structure and swimming efficiency in king scallops

4.1 Abstract

Scallops are bivalves that swim by jet propulsion through the adduction of the valves that enclose their mantle cavity. During adduction, two jets are formed at the dorsal edge of the scallop that propel the animal upwards and forward in the water column. Surprisingly little is known about the hydrodynamics of the jet structures involved in this mode of locomotion. In this study jet wake structures were characterised during jet propulsion swimming in free-swimming king scallops (*Pecten maximus*) using particle image velocimetry. Two distinct jet structures were observed which could be classified into two jet modes: (1) jet mode 1, in which all the ejected fluid rolled up into a vortex ring; and (2) jet mode 2, where the leading vortex ring 'pinched off' from the jet and was followed by a trailing jet of ejected fluid. Jets were found to transition at formation numbers of approximately 4. Thrust was found to be greater in jets around this transition point. Swimming efficiency increased with increased swimming speed, with a mean value of η_{wc} = 0.37. Increased efficiencies were associated with shallower jet angles and a reduction in slip. The orifice area of the jet was shown to decrease in area by approximately 89% during the jet period. This suggests that scallops may be able to exploit variable mantle kinematics during swimming to manipulate and enhance vortex production beyond what would be possible with a constant jet orifice area.

4.2 Introduction

Mechanically generated jet pulses, produced using a piston and cylinder mechanism, have demonstrated a limited principle in vortex ring formation: a phenomenon associated with pulsed jets known as 'pinching off' (Krueger and Gharib, 2003). This occurs due to the fact that there is a limit to the amount of energy that may enter a vortex ring during jetting. Once this limit is reached the vortex ring ceases to grow in strength and instead pinches off from the jet, any remaining fluid from the jet is then ejected as a trailing jet (Olcay and Krueger, 2010; Rosenfeld et al., 1998).

Hydrodynamically it is more costly to eject fluid in the form of a vortex ring with a trailing jet compared to fluid transport *via* an isolated vortex ring (Krueger and Gharib, 2003). Consequently, the dynamics behind the pinch off phenomenon have important implications in understanding the energetics of jet propulsion locomotor systems.

It is therefore of general interest to ask whether optimal vortex ring formation is being utilised in the jet propulsion systems of animals as a means of improving hydrodynamic efficiency. One key difference in the vortex rings that have been produced mechanically and those occurring in nature, is the existence of deformable structures in animals, which change the shape and area of jet orifice apertures during swimming. These time dependent kinematics are capable of changing the formation number for optimal ring formation found in constant-diameter jets (Dabiri et al., 2006). Decreasing the nozzle exit diameter during jetting has been found to increase the formation number at which isolated vortex rings cease to grow and pinch off (Dabiri and Gharib, 2005). This occurs for two reasons. A decrease in nozzle exit diameter will increase the velocity of the fluid being ejected from the jet, relative to a constant orifice nozzle exit diameter, enabling the fluid from the jet source to be fed into the forming vortex ring for longer, delaying pinch off (Mohseni et al., 2001; Shusser and Gharib, 2000). Additionally, the decreasing nozzle diameter alters the distribution of the vortex ring vorticity, with vorticity from the trailing jet being forced through the centre of the forming vortex ring due the motion of the nozzle exit (Dabiri and Gharib, 2005). Given that pulsatile jet propulsion occurs in a wide range of fluid transport systems, it is important to understand how this time varying parameter might affect the subsequent structure of vortex ring formation.

Scallops utilise jet propulsion as a means of predator avoidance. By rapidly closing and opening their shells, there are able to swim through the water column. During gape first (forward) swimming, the flexible mantle of the scallop forms a seal along the outer edge of the shell, leaving two open vents at the dorsal side of the animal, adjacent to the hinge ligament. Water is forced out of these vents, forming two jets of high velocity fluid, which provide thrust and propel the animal forward and upwards off the sea bed. Scallop jet propulsion differs from that of other jet propelling organisms as fluid enters the animal at the front and is ejected at the rear, rather than the rear intake seen in cephalopods and medusa (Moore and Trueman, 1971).

Energy transduction describes the transfer of energy from one form to another. In animal locomotion this transfer involves the chemical energy derived from food through to useful energy transferred to the environment to generate propulsion. This energy transduction consists of several steps, all of which need to be analysed in order to determine the overall performance of a particular locomotory system, these are: (1) the production of high energy phosphates (e.g ATP) from chemical substrates; (2) the utilisation of chemical energy from the hydrolysis of ATP to produce mechanical work by the muscles; (3) the transfer of the mechanical energy generated by the muscles to useful energy in the environment. Energy losses occur across all these steps, quantifying these losses would lead to a full understanding of the energetics of a particular locomotory system.

The simplicity of the scallop locomotor system as has attracted much interest from researchers. Numerous mechanical aspects of scallop locomotion have been investigated such as the hydrodynamics of the shells (Anderson et al., 1997) and the properties of the hinge ligament system (DeMont, 1990). Muscle performance has been characterised both *in vivo* and *in vitro* (Marsh et al., 1992; Olson and Marsh, 1993; Marsh and Olson, 1994) in live animals as well as being the subject of mathematical modelling (Cheng et al., 1996). However, the jet wake structure and efficiency with which mechanical energy from the adductor muscle is transferred into useful energy in the environment of swimming scallops is currently unknown.

Previous studies have demonstrated that almost all of the mechanical energy from the contraction of the adductor muscle is used to perform hydrodynamic work for jet production, with the amount used to re-extend the elastic hinge ligament negligible (Cheng et al., 1996; Marsh et al., 1992). Therefore understanding how much of this mechanical energy is transferred to the water and thus propelling the scallop forward is essential in understanding the overall efficiency of this locomotor system.

In this study, the structure of scallop jet wakes was characterised using particle image velocimetry (PIV). It was hypothesised that scallops would be able to increase the formation number at which their jets transitioned from jet mode 1 to jet mode 2 jets by using a variable diameter jet orifice. The aim of this study was to quantify swimming performance in scallops and to gain insight into the hydrodynamic efficiency of this locomotor system. The results will also be combined with previous work on scallop muscle performance to quantify how much of the work done by the adductor muscle is transferred to useful energy in the wake of the animal.

4.3 Materials and methods

4.3.1 Animals

Wild caught king scallops (*Pecten maximus,* Linnaeus 1758) from the Irish Sea were obtained from The Ethical Shellfish Company, Mull, Scotland in November 2015 and maintained in artificial seawater (Instant Ocean, Aquarium Systems, Mentor, OH). Tanks were kept at a temperature of 12°C and a salinity of 34ppt, corresponding to the conditions in the location from which the scallops were collected in the Irish Sea. Scallops were fed twice a day using 'reefphyto' phytoplankton (Reefphyto Ltd, UK). Scallops ranged in body mass from 144g – 373.5g (mean = 265.4 ± 26.6 g, *n* = 9). Scallops were allowed to acclimate to the laboratory for a minimum of one week before experiments took place.

4.3.2 PIV and jet wake visualisation

PIV experiments took place in a 126 litre (610×460×450mm length×width×depth) glass aquarium. The experimental tank was kept under the same conditions in which the scallops had been living in the lab. Scallops were transferred to the experimental tank and allowed to acclimatise for at least 30 minutes. Escape swimming was elicited by touching the scallops with the tube feet of a common starfish *(Asterias rubens,* Linnaeus 1758) adjacent to the hinge of the scallop.

Quantitative analysis of the jet structure of king scallops was obtained using two-dimensional PIV. The swimming area was calibrated in mm by recording an image of a 2D calibrated target (14x14mm square grid with the tank was full of water). The experimental tank was seeded with aluminium oxide (Sigma-Aldrich, Poole, Dorset, UK) with an average particle size of 5μm at a density of 30mg per litre. Particles were illuminated with a 1W continuous 532nm, green laser (Shanghai Dream Lasers Technology Co., Ltd., Shanghai, People's Republic of China) directed through a Powell lens (Thorlabs, Inc., Newton, NJ, USA) creating a 1mm thick, vertically orientated light sheet. The wake of swimming scallops was visualised in a sagittal plane, only swim sequences where the light sheet bisected either the anterior or posterior jet of the scallop were used. The scallops and particle movements were filmed using a Photron FASTCAM SA3 (Photron USA, San Diego, CA, USA) high speed camera recording at 500 frame s^{-1}, shuttered at 1/500 s, recording at 1280 x 1024 pixel resolution.

The positions of the illuminated particles were determined using PIVlab (Thielicke & Stamhuis, 2012), an open source program written in MATLAB (R2012a; The Mathworks, Inc., Natwick, MA, USA). The image sequences were pre-processed with a contrast-limited adaptive histogram equalisation tool to enhance contrast. The body of the king scallop was masked on the images to eliminate edge effects. A cross correlation technique was used with adaptive multi-pass processing to analyse image pairs and to track particle movement between frames. A total of three passes were used to analyse images, with an initial interrogation window of 128 x 128 pixels and a final size of 32 x 32 pixels with a 50% overlap between each pass. A standard deviation filter was used to remove vectors were more than 7 deviations away from the mean flow. 0.51 ±0.02% of the vectors that were found to be erroneous in an 1800 vector frame. Missing velocity vectors were interpolated using a boundary value solver.

4.3.3 Jet properties and swimming efficiency

Jet thrust (T,) the rate at which an animal transfers momentum to the surrounding fluid was calculated as:

$$T= \rho \bar{u}_{j}^{2} \bar{A}_{j} \qquad [4.1]$$

where ρ is seawater density (1025 kg m^{-3}) and $\bar{A}j$ is the average jet orifice area over the course of the jet period (Sutherland and Madin, 2010). Average jet velocity ($\bar{u}_j$) was calculated by taking the average jet core velocity over the course of one jet cycle, where the jet cycle is considered to be from the start of one adduction to the start of the next.

Jet orifice area was calculated using images analysed in ImageJ (ImageJ, Bethesda, Maryland, USA), in which the jet orifice was perpendicular to the lens. However, during escape swims recorded for PIV analysis it was not possible for this measurement to be taken.

In order for jet area to be calculated from these swims, area was calculated using the short diameter of the orifice, assuming an elliptical orifice shape, as in Cheng and DeMont (1996). Calculating actual jet orifice area, using images analysed in ImageJ (ImageJ, Bethesda, Maryland, USA), and comparing them to values using these calculations validated this method. Calculated values were on average 1.92% (± 0.364%, $n = 15$) greater than those values obtained from images in ImageJ. Jet orifice area was therefore calculated as:

$$\frac{3\pi L_s^2}{4} \qquad [4.2]$$

where L_s is the short diameter length of the jet orifice.

During jet propulsion water is accelerated twice, once as it enters the animal ($\bar{u}_r$) and once as it is ejected ($\bar{u}_j$), any method for calculating swimming efficiency must take into account the net change of momentum of this mass of water (m_j). An approach was developed by Alexander (2003), in which account is taken of the acceleration of the water during both the refilling and contraction phases of the swimming cycle. The force propelling an animal forward is equal to the rate of change of momentum, meaning that the rate at which work is being done to overcome hydrodynamic drag is $m_j\bar{U}\bar{u}_{j,}$ where $\bar{U}$ is the time averaged swimming speed of the animal. During jetting, kinetic energy is lost to the water at a rate of ½ $m_j\bar{u}_j^2$, giving a total power requirement of $m_j\bar{U}\bar{u}_j + ½\, m_j\, (\bar{u}_r^2 + \bar{u}_j^2)$. Efficiency is equal to the useful power over total power input, whole cycle efficiency (η_{wc}) is therefore calculated as:

$$\eta_{\mathrm{wc}}=\frac{2\bar{U}\bar{u}_{\mathrm{j}}}{2\bar{U}\bar{u}_{\mathrm{j}}+\bar{u}_{\mathrm{r}}^{2}+\bar{u}_{\mathrm{j}}^{2}} \qquad [4.3]$$

where $\bar{u}_{\mathrm{r}}$ is the refill velocity, i.e. the velocity of the fluid at the intake orifice during the refilling of the mantle. Refill velocities were measured using PIV. Due to the orientation of the light sheet, it was not possible to get simultaneous recordings of both the intake velocity and jet velocity and so these had to be determined in separate swims.

A second method for calculating whole cycle efficiency was also used which assumes that the refilling of the mantle cavity during valve opening occurs passively as a result of the forward motion of the animal (η_{p}):

$$\eta_{\mathrm{p}}=\frac{2\bar{U}\bar{u}_{\mathrm{j}}}{2\bar{U}\bar{u}_{\mathrm{j}}+\bar{u}_{\mathrm{j}}^{2}} \qquad [4.4]$$

due to the fact that no additional momentum is being imparted to the water as it enters the animal, greater efficiencies are theoretically achievable in animals with forward facing jet intakes (Alexander, 2003).

The rate of useful work that was imparted to the water was calculated as $2\bar{U}\bar{u}_{j}$ (Alexander, 2003).

Slip (S), an indicator of the inverse of the propulsive efficiency, was calculated from $\bar{u}_{\mathrm{j}}$ and $\bar{U}$ (Bartol et al., 2009b) as:

$$S = \frac{\bar{u}_\mathrm{j}}{\bar{U}} \qquad [4.5]$$

Formation number was calculated as:

$$F = \frac{L_\mathrm{j}}{D_\mathrm{j}} \qquad [4.6]$$

where L_j is the jet length measured as the extent of the vorticity field along the jet centreline and D_j is the diameter of the vortex ring measured from the two peaks of vorticity that make up the ring (Bartol et al., 2009b).

Jet angle (β) is the angle of the jet relative to the swimming path of the scallop.

4.3.4 Statistical analyses

Statistical analysis was carried out in SPSS for Mac (IBM SPSS Statistics for Mac, Version 21.0. Armonk, NY). All data are reported as mean ± s.e.m. Data were checked for normality using a Shapiro–Wilks test. Data were fitted with linear or polynomial regressions and tested using one-way ANOVA to determine if a significant difference existed between means. If a difference was detected, Tukey's post-hoc tests were used to identify where these differences occurred.

4.4 Results

In total, 32 jet sequences were gathered from 9 free swimming king scallops. Scallops were found to swim at speeds of 0.49 – 3.05 BL s^{-1} at *Re* of ~1.8×10^4.

Table 4.1. Animal morphology and swimming kinematics in king scallops

Body Mass (g)	247.31 ± 23.38
Anterior - Posterior Length (cm)	12.30 ± 0.59
Cycle Frequency (Hz)	2.41 ± 0.04
Swimming Speed (BL s^{-1})	1.46 ± 0.11
Duty Cycle	0.36 ± 0.01

BL s^{-1}, body lengths per second with one body length being the dorsal-ventral length of the animal

Duty cycle, the proportion of the swimming cycle that is made up of the power stroke

4.4.1 Jet wake structure

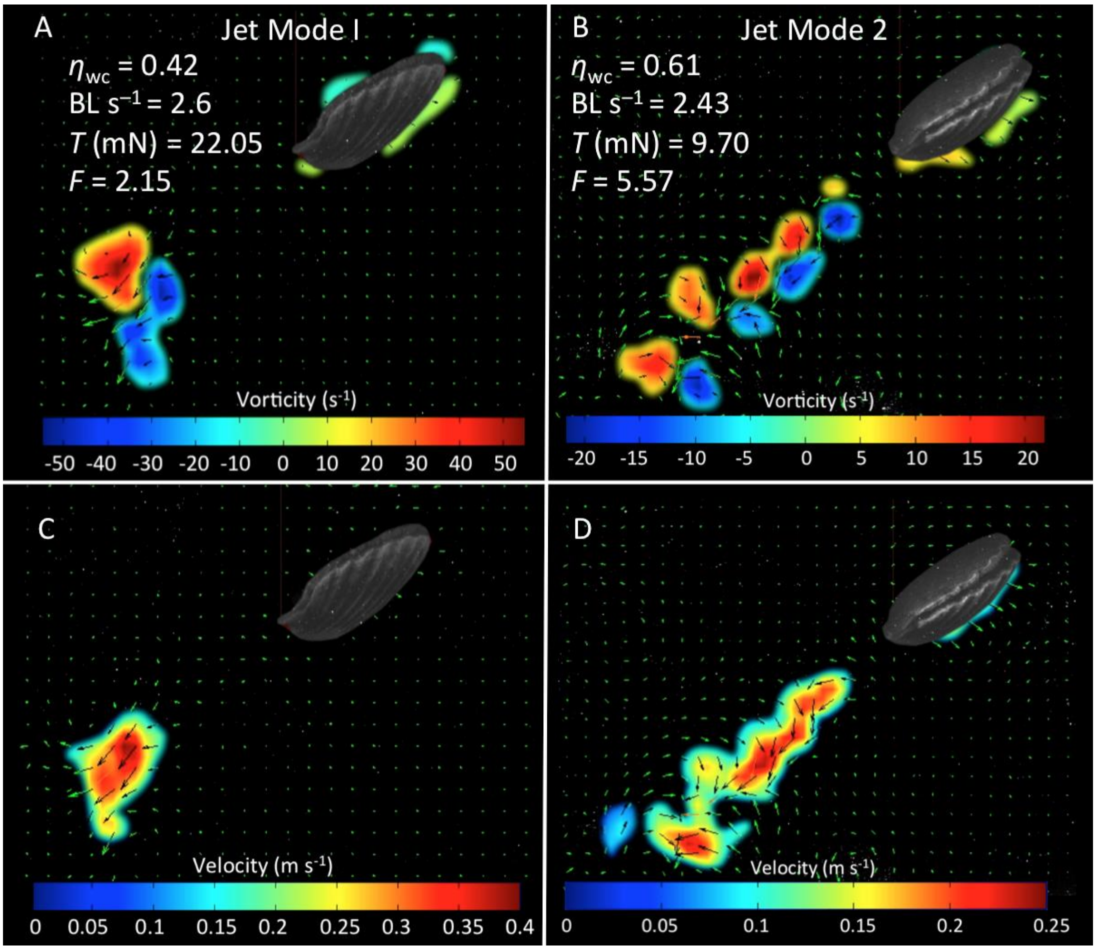

Figure 4.1. Jet wake structure during swimming in king scallops. Vorticity (A,B) and velocity (C,D) fields. Examples of isolated vortex rings (A,C) and trailing jet vortex structures (B,D) identified. On vorticity plots, red and blue regions denote clockwise and counter clockwise rotation, respectively.

Quantitative 2D-analysis of the jet structure in the wake of swimming scallops was determined using PIV. The captured jets were typically the fourth to sixth jet during the swim of the scallop, with the scallop having risen in the water column and swimming at such a height as to avoid boundary effects from the walls and base of the tank (Vogel, 1981). Two distinct jet modes were observed and were characterised as jet mode 1 and jet mode 2 structures, following previous studies (Bartol et al., 2009b). Jet mode 1, in which all the ejected fluid rolls up into an isolated vortex ring, was observed in 69% of the jets (Fig. 4.1A, 4.1C). Jet mode 2 jets, in which the leading vortex ring pinched off and was followed by a trailing jet of fluid was seen in 31% of the jet sequences (fig. 4.1B, 4.2D).

4.4.2. Swimming performance

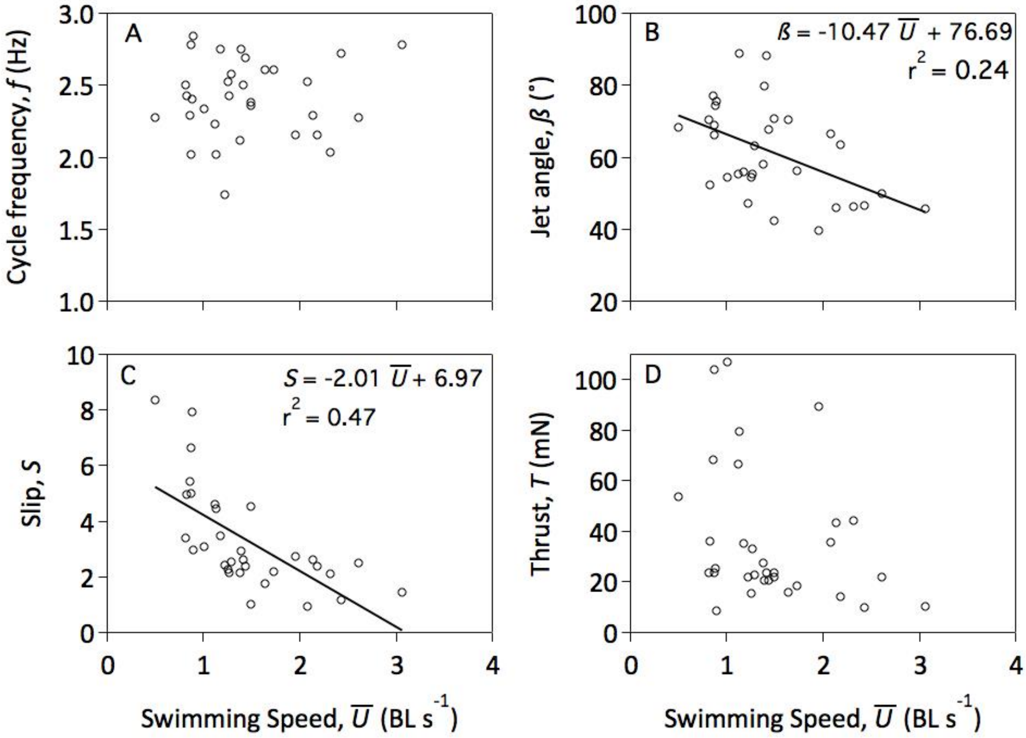

Figure 4.2. Swimming performance as a function of swimming speed in king scallops. Cycle frequency (A). Jet angle (B). Slip (C) and Thrust (D).

Figure 4.2 shows several parameters of scallop jet propulsion in relation to swimming speed. Cycle frequency (fig. 4.2A) was found to be independent of swimming speed ($F_{1,30} = 0.103$, $p = 0.75$), with a mean of 2.41±0.05Hz (range = 1.74 -2.84Hz). Jet angle (fig. 4.2B) decreased with increased swimming speed ($F_{1,30} = 9.316$, $p < 0.01$) and covered a range of 39.7° - 88.88°. Slip (fig.4.2C) decreased with increased swimming speed ($F_{1,30} = 23.043$, $p<0.001$). Average thrust (fig. 4.2D) was also independent of swimming speed ($F_{1,30} = 1.961$, $p = 0.171$), with a mean of 36.43 ± 4.77 mN (range = 8.64-107.09). Additionally, peak jet velocity was found to be independent of swimming speed ($F_{1,30} = 0.474$, $p = 0.496$) with a mean of 84.2±5.1 cm s^{-1} (ranged 37.3 cm s^{-1} - 146.88 cm s^{-1}).

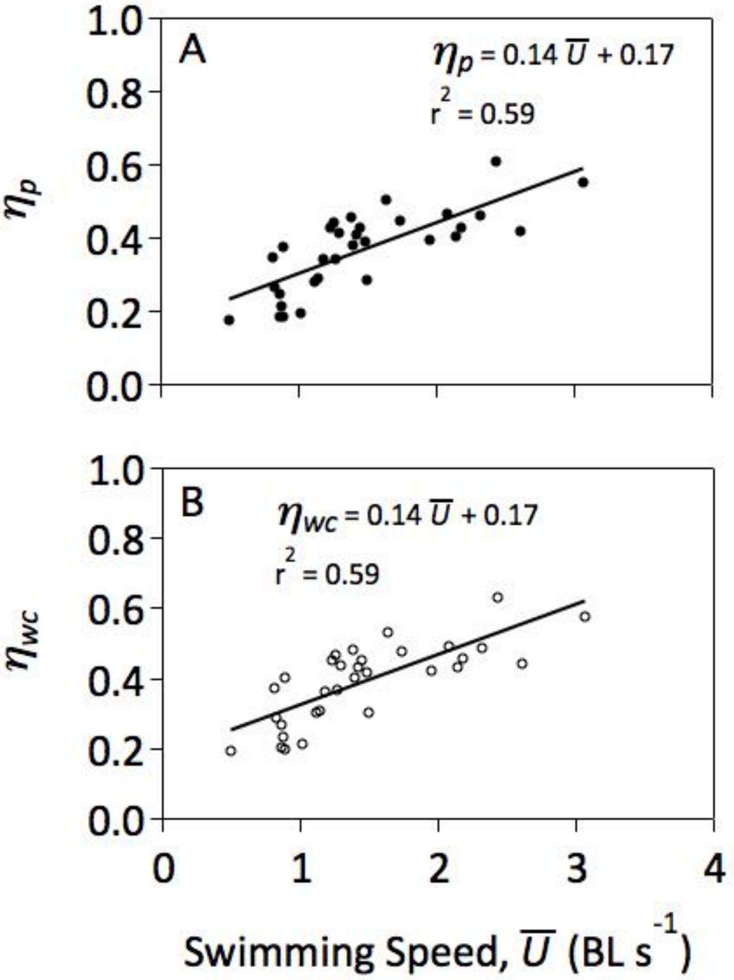

Figure 4.3. Swimming efficiency as a function of swimming speed during jet propulsion swimming in king scallops. Whole cycle efficiency assuming passive refilling (A). Whole cycle efficiency (B).

Whole cycle swimming efficiency increased with swimming speed when calculated either assuming passive refill velocities (η_p; equation 4.4; fig. 4.3A; $F_{1,29}$ = 9.405, $P<0.05$) or when calculated using measured refill velocities (η_{wc}; equation 4.3; fig. 3B; $F_{1,29}$ = 8.583, $P<0.01$). Assuming passive refilling of the mantle, mean swimming efficiency was 0.39±0.02 (range = 0.19 to 0.63) ($F_{1,29}$ = 9.405, $P<0.05$). Mean swimming efficiency using measured refill velocities was 0.37±0.02 (range = 0.18 to 0.61).

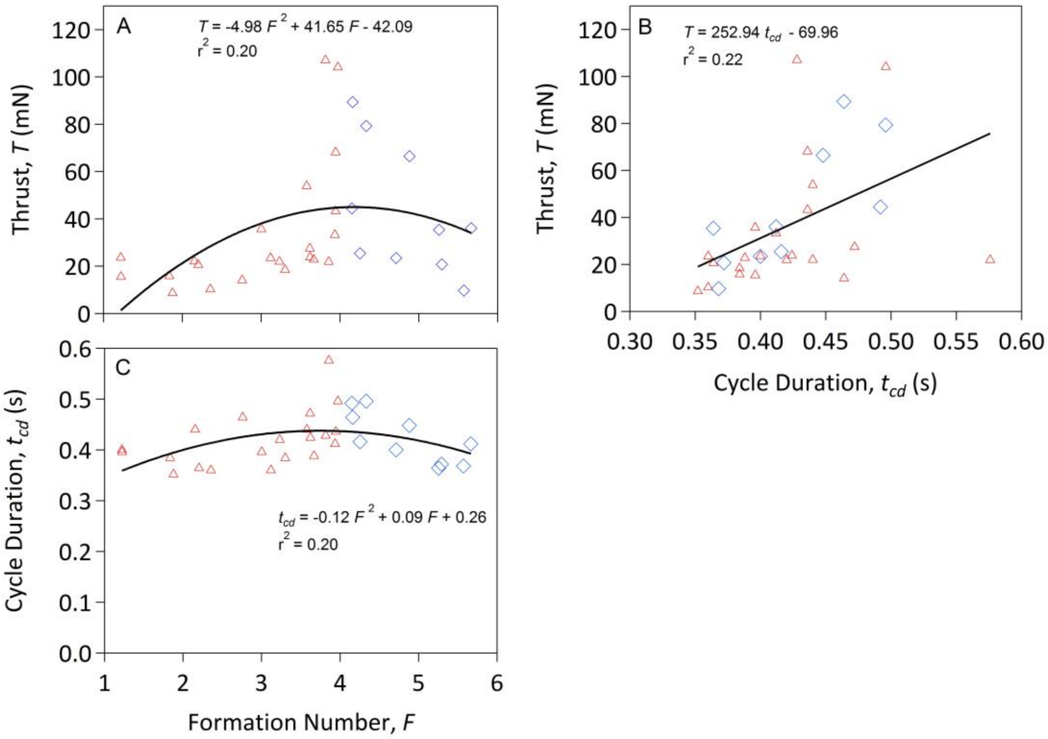

Figure 4.4. Average thrust as a function of formation number (A), and cycle duration (B). Cycle duration as a function of formation number (C). Red triangles represent jet mode 1 jets, blue diamonds represent jet mode 2 jets.

Jets were found to transition between the two identified jet modes at formation numbers of 4. There was no significant difference found between the average thrust produced in jet mode 1 (mean = 32.42±5.72 mN) and that produced in jet mode 2 (mean = 38.07±8.15 mN) ($F_{1,13}$ = 1.113, p = 0.276). Thrust plotted as a function of formation number was fitted with a polynomial regression ($F_{1,29}$ = 3.624, $p<0.05$), with an increase in thrust apparent around formation numbers of 4 (fig. 4.4A). Thrust increased with increasing cycle duration ($F_{1,29}$ = 8.607, $p<0.01$; fig 4.4B). Formation number was found to be independent of average jet orifice size ($F_{1,29}$ = 0.295, p=0.747) and duty cycle ($F_{1,29}$ = 0.837, p=0.443). Formation number plotted as a function of cycle duration was fitted with a polynomial regression ($F_{1,28}$ = 4.552, $p<0.05$; fig. 4.4C).

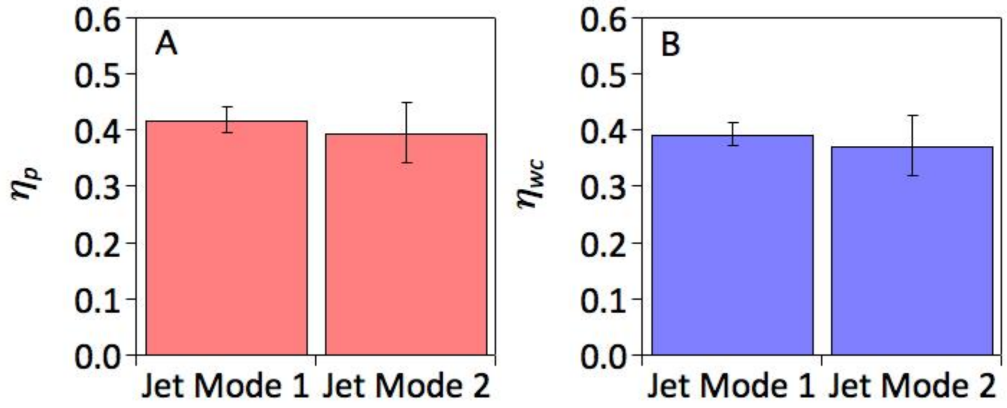

Figure 4.5. Swimming efficiency as a function of jet mode during jet propulsion swimming in king scallops. Whole cycle efficiency assuming passive refilling (A). Whole cycle efficiency (B).

4.3.3 Comparison between swimming performance in swims powered using jet mode 1 and jet mode 2

No differences were found in swimming efficiency between the two jet modes. Whole cycle efficiency assuming passive refilling was 0.42±0.02 in jet mode 1 and 0.40±0.05 in jet mode 2 jets ($F_{1,13} = 0.068$, $p = 0.77$) (fig. 4.5A). Whole cycle efficiency calculated using measured refill velocities were 0.39±0.02 for jet mode 1 and 0.37±0.05 for jet mode 2 ($F_{1,13} = 0.049$, $p = 0.83$) (fig. 4.5B).

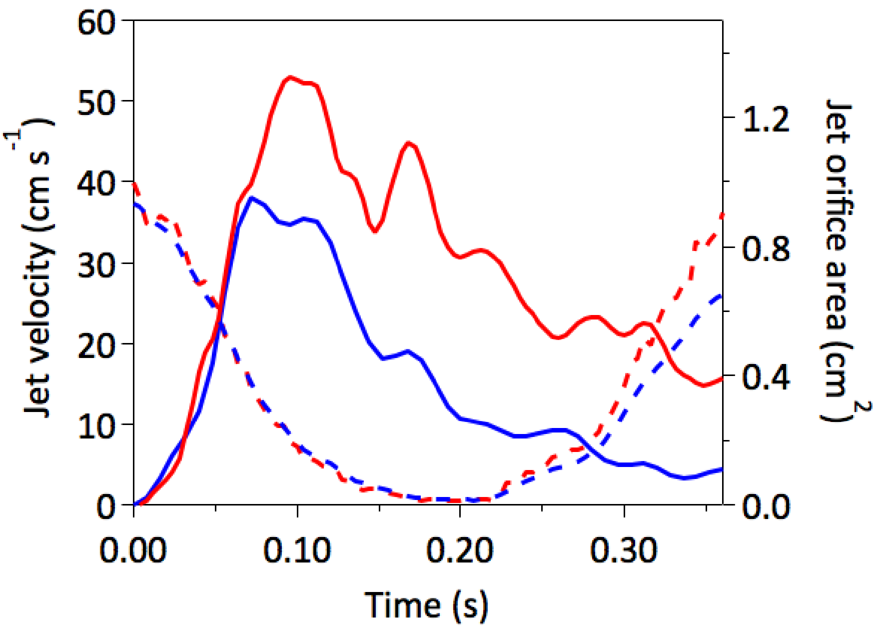

Figure 4.6. Example of the time dependent changes in jet velocity (solid lines) and scallop jet orifice area (dashed lines) during one swimming cycle. Jet velocity profiles and orifice size changes of a jet mode 1 jet (red line) and a jet mode 2 jet (blue line).

The velocity profile of the jets typically consisted of a sharp increase in velocity at the start of the cycle, before decreasing over the course of the jet period. An increase or period of sustained jet velocity was identified towards the end of the jet period. Jet orifice area decreased over the course of the swim cycle (fig. 4.6).

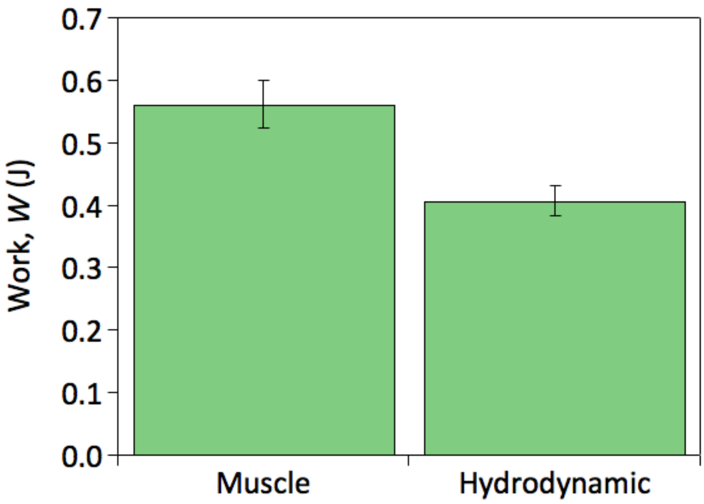

Figure 4.7. Comparison between the work output of king scallop adductor muscle measured *in vivo* with the useful energy transferred to the water calculated from PIV analysis.

In two of the scallops tested, both muscle work and useful hydrodynamic work were determined during swimming (muscle work was determined as explained in Chapter 2). The useful hydrodynamic work that entered the water in the form of the wake was ~73% of the calculated muscle work from the *in vivo* experiments.

4.4 Discussion

Scallops swim by jet propulsion to evade predators, as such it is essential to their survival, however the efficiency of this system has never been directly measured. This study reports the first quantitative analysis of the wake structure and hydrodynamic efficiency measured using PIV in scallops during jet propulsion swimming. Scallops produced two modes of jetting, resulting in a wake comprising of isolated vortex rings or in a wake consisting of leading vortex rings with a trailing jet. These two jet modes have been observed in other jet propelled organisms such as squid, salps and jellyfish (Bartol et al., 2009b; Dabiri et al., 2010; Sutherland and Madin, 2010).

4.4.1 Swimming performance

Neither cycle frequency nor average thrust were correlated with swimming speed (fig. 4.2). Swimming speed was largely determined by jet angle, with shallower jet angles yielding higher swimming speeds (fig. 4.2B), with a concurrent decrease in slip (fig. 4.2C). There was a small difference in swimming efficiencies calculated using the whole cycle efficiency equation using either passive or measured refill velocities. Average refill velocities determined using PIV were slightly higher than those expected assuming a passive refilling of the mantle cavity, in which refill velocity is equal to the forward velocity of the animal. There was an increase in fluid velocity entering the mantle cavity at the beginning of the opening phase of the cycle, this is almost certainly due to a drop in pressure that occurs as the shells reopen (Chapter 2, fig. 2.2; Marsh et al., 1992). The reduction in mantle cavity pressure draws water in at the beginning of the opening phase of the swim cycle, the acceleration and subsequent deceleration of the fluid as it enters the mantle cavity decreases swimming efficiency slightly in scallops. Average whole cycle efficiency was

0.37±0.02 (range = 0.18-0.61), which is comparable to the 0.34 - 0.48 that has previously been measured in squid jet propulsion swimming (Anderson and Demont, 2000). It is reasonable to predict that higher efficiencies might be achievable in other scallop species. The king scallop is a poor swimmer amongst scallops. King scallops swim at speeds between 7-35 cm s^{-1}, which is much slower than the swimming speeds in some species in the genera *Amusium* and *Plactopecten*, which have been found to swim at speeds of 60-160 cm s^{-1} (Caddy, 1968; Morton, 1980). Faster swimming scallops exhibit several morphological adaptations that may enhance their swimming performance. For example, they are flatter, resulting in a relatively smaller frontal area and therefore a lower pressure drag (Hayami, 1991). In addition, the profile of the valves in cross section approaches the optimum shape for an aerofoil for low aspect ratio wings (Hoerner and Borst, 1975), potentially increasing lift, meaning that the more of the energy of the jet can be used to overcome pressure drag. The shells of *Plactopecten magellanicus* are also thought to be particularly good at reducing friction drag along the shell (Anderson et al., 1997) due to the size and arrangement of the riblets that line the shell, which could reduce friction drag by 3%- 8% (Kline et al., 1967; Mullins, 1997). The morphology of the king scallop is far from optimal in a hydrodynamic sense. The top valve is almost flat, whilst the bottom valve is highly concave. This appears to be advantageous when the scallop is settled on the substrate, as it will tend to dig itself a small pit in which to sit in. However, this shape is no doubt detrimental to swimming performance: the curved lower valve acts as an inverted hydrofoil, meaning that king scallops struggle to gain any height in the water column and instead cruise just a few centimetres above the substrate. Additionally, the riblets of the king scallop are comparatively large compared to those of *P. magellanicus*, and therefore the king scallop may not benefit from the same reduction in friction drag that has been predicted for *P. magellanicus*, further limiting its swimming performance. Numerical modelling of scallop swimming using the species *P. magellanicus* predicted whole cycle efficiency to be between 0.3 and 0.5 (Cheng et al., 1996), values that lie within the range measured in the present study (0.18-0.61).

4.4.2 Jet Mode

Neither thrust nor efficiency were affected by the jet mode utilised. However, thrust was maximal at a formation number of approximately 4, the formation number at which there is a transition from a wake comprising isolated vortex rings into a wake consisting of long trailing jets. These results are similar to those found in mechanically produced jets (Krueger, 2001), suggesting that scallops may be able to produce jets that are optimised for producing maximal thrust per unit of expelled fluid via isolated vortex rings. The average jet orifice size and duty cycle were both approximately constant across variations in formation number. The increase in thrust at formation numbers around 4 seems to be matched by an increase in the cycle duration (fig. 4.4B). It seems that scallops are able to produce jets that are optimised for thrust production when they are swimming at a specific frequency. At these frequencies, an increase in thrust is apparent, presumably due to an increase in the contribution of 'over-pressure' during the formation of the jet, which has been shown to be a key factor in enhancing thrust at formation numbers around the transition between jet mode 1 and jet mode 2 (Krueger and Gharib, 2003). Although similar to mechanically generated jet impulses, these results are inconsistent with the wakes produced by other organisms swimming using jet propulsion. For example, in squid it was shown that jet mode 2 was the most frequently used, and resulted in higher time averaged thrust and lift forces. In swimming squid however, jet mode 1 was shown to correspond to a higher propulsive efficiency (Bartol et al., 2009b). Salps also exhibit two distinctive jet modes during swimming (Sutherland and Madin, 2010), but in contrast to squid swimming, the highest thrust was achieved when swimming using jet mode 1, with the slow swimming species *Pegea confoederata* producing the highest propulsive efficiency (η_{wc} = 0.55) of the species tested. A key aspect of the relatively high efficiency of salps is that they swim continuously using a high-volume, low-velocity jet (Alexander, 2003). Scallops, like salps, have forward intake jets. The frontal area of a salp does not change significantly during jetting (Sutherland and Madin, 2010). In scallops however, the refilling period increases drag considerable due to the increase in frontal area resulting from the opening of the valves (Cheng and DeMont, 1996a). This limits the scallop's ability to be able to exploit a jet and cruise style of jet propulsion such as that seen in both squid and salps.

4.4.3 Vortex ring formation in relation to formation number

Several recent studies have tried to quantify the conditions under which optimal vortex ring formation occurs. Previous work using mechanically generated jets have shown that vortex formation is optimised at a jet length-to-diameter ratio (formation number) of 3.6-4.5 (Mohseni and Gharib, 1998). In jets that lie above this optimum range, a phenomenon known as 'pinching off' occurs, in which the leading vortex ring disconnects from the initial jet and is then followed by a plug of ejected fluid, exiting as a trailing jet (Krueger and Gharib, 2005). However, the formation number at which isolated vortex rings are formed during jet propulsion in various organisms can differ from the range found in mechanically generated jets (Dabiri et al., 2006). Additional factors have been identified as influencing vortex formation from experiments using both mechanically generated jets and in other jet propelled organisms. The first of these is the presence of background flow during jetting. Background co-flow has been shown to inhibit (Mohseni and Gharib, 1998) vortex formation by causing leading vortices to pinch off earlier than occurs in the absence of background flow, resulting in elongated jets with weak or absent vortex rings with formations number <1 (Krueger et al., 2006). However, background counter-flow can delay pinch off (Dabiri and Gharib, 2004b). Other factors that have been shown to influence jet formation is a variable diameter of the jet orifice (Dabiri and Gharib, 2005) or changes in jet velocity during the jet period (Mohseni et al., 2001). It has been demonstrated that the jellyfish species *Nemiopsis bachei* exploit velar kinematics during jet propulsion, increasing the formation number at which isolated vortex rings are formed. The variations that occurred in bell diameter during jetting resulted in vortex rings being produced at formation numbers as high as 8, and pinch off was never observed (Dabiri et al., 2006). It therefore seems plausible that certain features of scallop jet propulsion, such as variable jet orifice diameter and changes in the velocity of the fluid during jetting would enhance vortex ring formation and structure (fig. 4.6). Jet orifice area decreased an average of 89% over the course of the jetting period of the swimming cycle through the contraction of their mantle. It is likely that this reduction in jet orifice area results in the increase or to the maintenance of the velocity of the jet that was observed as it is driven out of the mantle cavity at the end of adduction. This results in more fluid being fed into the leading vortex ring, allowing it to grow in size and delaying pinch off. This is demonstrated by the fact that formation numbers where jets transition from jet mode 1 to 2 are approximately 4, despite the presence the background flow, which would otherwise have been expected to reduce the formation number (Krueger et al., 2006).

4.4.4 Energy transduction

It has been shown that the amount of work done on the elastic hinge ligament during adduction is negligible and amounts to less than 1% of the total work done during contraction (Marsh et al., 1992). Comparing the muscular work output of the scallop adductor muscle with the useful work transferred into the wake shows that approximately 73% of the muscular work output is transferred to momentum in the fluid. Energy losses are likely to occur due to ejected fluid being used to produce lift, as well as overcome pressure drag. Other losses may to occur due to the fact that not all of the fluid within the mantle cavity is ejected from the mantle cavity during adduction, meaning that work is being done on the fluid that does not contribute to the forward momentum of the animal. In addition, the deformation of the flexible mantle to produce the jet orifices will also contribute to the energy losses experienced in this particular locomotor system. Presumably together these losses are the difference between the muscular work and the total energy imparted to the water. In swimming jellyfish, it has been shown that only 39-61% of the total mechanical power produced went to producing the jet, whereas 19-32% went to the kinetic energy of the bell and 20-29% to the deformation of the bell (DeMont and Gosline, 1988). Similarly in swimming fish, a significant proportion of the mechanical power goes to deforming body tissues (Cheng et al., 1998).

4.4.5 Summary

In this study the ability of scallops to be able to produce isolated vortex rings has been demonstrated for the first time. It has also been shown that scallops are capable of producing at least one other form of jet, previously described in other species. Evidence was found that suggests scallops are able to produce vortex rings near *F* that are optimised in producing maximum thrust per unit volume of expelled fluid. Hydrodynamic swimming efficiency in scallops was comparable to other species that swim by jet propulsion, with jet angle being the main determinant on swimming performance. Future investigations into jet wake structure in scallops could look to investigate temperature effects on swimming efficiency and wake structure. A temperature change of 10°C decreases cycle duration by 48% in queen scallops (Bailey and Johnston, 2005). It would be interesting to determine whether temperature change affected the formation number at which jets shifted from jet mode 1 to jet mode 2, as not only will the swimming dynamics of the scallop have changed, the physical properties of the water such as viscosity would be altered. During this investigation, scallops were occasionally observed changing swimming direction during escape swims. This suggests that scallops may have some control over the direction in which they swim by altering the amount of fluid that is ejected out of each of its jets. As swimming is an escape response in scallops, the ability to be able to control swimming direction would have big implications on potential survivorship of individuals and is therefore of considerable interest.

Chapter 5

Swimming mechanics and propulsive efficiency in the nautilus (*Nautilus pompilius*)

5.1 Abstract

Nautilus are the last remaining representative of externally shelled cephalopods. The jetting hydrodynamics associated with this unique body structure are not well understood. In this study, particle image velocimetry was used to characterise the wake structures and swimming performance of the chambered nautilus (*Nautilus pompilius*). Two swimming orientations were identified, anterior first and posterior first. Propulsive efficiency increased with increasing swimming speed during posterior first swimming, but decreased with increasing swimming speed during anterior first swimming. Differences is propulsive efficiency were largely dependent on variations in slip between swimming speeds in each swimming orientation. Higher swimming efficiencies during slow anterior first swimming were achieved via a change in swimming mechanics, with these swimming speeds being associated with an increase in duty cycle and jet period. *Nautilus* were shown to produce jets consisting of both isolated vortex rings (jet mode 1) and elongated jets (jet mode 2). There was no apparent preference for jet mode across swimming speed, although jet mode 2 jets did have a trend for producing greater time averaged thrust. The results of this study demonstrate that *Nautilus* have become adept at exploiting the niche in which they exist, being seemingly tuned for life as a slow swimming scavenger, expending as little energy as possible through the use of low power output, efficient swimming.

5.2 Introduction

Often considered a ‘living fossil’, *Nautilus* has likely remained relatively unchanged for the last 200 million years (O’Dor et al., 1990). Along with their close relative the *Allonautilus*, they represent the last remaining externally shelled cephalopod alive today. Their modern coleoid relatives, which include squid, cuttlefish and octopus, have lost their protective hard shells in favour of a fast predatory lifestyle. The external shell provides *Nautilus* with protection from predators and its inter-connected chambers provide a means of buoyancy control, enabling animals to make diurnal, vertical movements in the water column of several hundred metres (Dunstan et al., 2011).

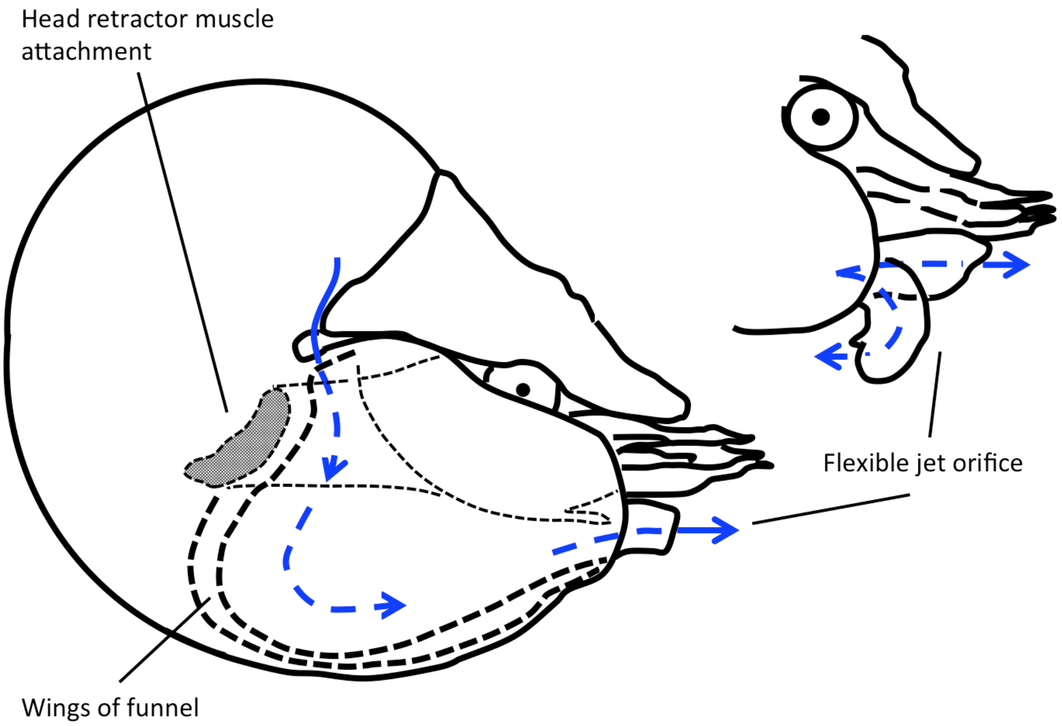

Figure 5.1. Two mechanisms of producing jets during swimming in *Nautilus*.1) By the contraction of the large head retractor muscle, or 2) through the rhythmic contraction of the funnel wings. Inset demonstrates how the flexible jet orifice can move to direct water in multiple directions. Blue lines represent the flow of fluid through the animal which facilitates both oxygen exchange and locomotion. Figure adapted from Packard et al. (1980).

Like their coleoid relatives, *Nautilus* swim by means of jet propulsion. Powerful jetting is produced by the compression of the mantle cavity produced by contraction of the retractor and funnel muscles. Contraction of the pair of retractor muscles causes the entire animal to be drawn into the shell, compressing the mantle cavity (Packard et al., 1980). The funnel muscles (including the funnel wings or crura) contract in concert with the contraction of the retractor muscles additionally contributing to the compression of the mantle cavity. Compression of the mantle cavity results in a pressure difference between the mantle cavity and the ambient water, resulting in water being expelled from the mantle cavity via the siphon (as well as along the top edges of the shell aperture during very powerful contractions;

Packard et al., 1980; Chamberlain, 1990). Slower swimming movements and ventilation are powered by rhythmic, contractions of the funnel flaps that results in a wave of movement that moves anteriorly along the funnel wings, producing unidirectional flow of water across the gills, through the mantle cavity and exiting through the siphon (Wells and Wells, 1985; Chamberlain, 1990). The fluid jet is formed by the funnel wings that extend along either side of the head and overlap along the ventral side of the animal terminating in a manoeuvrable orifice – the funnel. The funnel allows the water to be ejected at a range of angles giving *Nautilus* the ability to swim in all directions (fig. 5.1).

The efficiency of swimming by jet propulsion is lower than swimming by undulation. This has been demonstrated by comparing the oxygen consumption of similarly sized salmon and squid (Webber and O'Dor, 1986). This difference in efficiency originates from the fact that, for a given thrust, jet propulsion swimming involves accelerating a small mass of fluid to a high velocity to achieve propulsion, whereas greater efficiencies are achievable from accelerating a large mass of water at slower velocities, as in an undulatory swimmer (Anderson and Grosenbaugh, 2005). The metabolic energetic cost of jet propulsion swimming in *Nautilus* has been measured directly at slow speeds from oxygen consumption ($\dot{V}_{O_2}$) and estimated from inter-mantle pressure at higher speeds (based on a relationship between mantle cavity pressure and $\dot{V}_{O_2}$ at slow speeds; O'Dor et al., 1990). At its typical swimming speed and below, the metabolic cost of transport in *Nautilus* is low compared to squid and salmon (O'Dor et al., 1990). The reasons for the low cost of jet propulsion swimming in *Nautilus* are unclear, however, knowledge of the wake structure may give some insights.

In swimming squid, two categories of wake structures, consistent with those types produced by mechanical pistons (Gharib et al., 1998), have been observed: jets in which the wake consists of isolated vortex rings (referred to as 'jet mode 1' jets) and jets in which there is a trailing jet present, following vortex ring pinch-off (referred to as 'jet mode 2' jets; Bartol et al., 2009). Jet mode I was shown to have higher propulsive efficiencies, (propulsive hydrodynamic efficiencies of 69% in jet mode 1 swimming and 59% in jet mode 2), but a lower time-averaged thrust (~1 mN), compared to jet mode II jets (~2 mN) (Bartol et al., 2009). The formation number at the transition between the two jet modes occurred was comparable to that found in the mechanically generated jets (Gharib et al., 1998).

The structure of the wake during jet propulsion swimming in *Nautilus* is unknown. The aim of this study was to quantify jet wake structure and to calculate hydrodynamic efficiency in *Nautilus* using particle image velocimetry (PIV) to visualise the flows associated with free swimming *Nautilus*. It was hypothesised that that *Nautilus* would swim with greater hydrodynamic efficiencies than other jet propelling animals due their slow movement and neutral buoyancy, producing jets that were maximised for producing thrust per unit volume of expelled fluid. Understanding wake structure may give insight into the economical jet propulsion swimming exhibited by *Nautilus*.

5.3 Materials and methods

5.3.1 Animals

Chambered nautilus (*Nautilus popilius* Linnaeus, 1758) were obtained from a UK marine livestock supplier (Tropical Marine Centre, Manchester, UK) and housed in a 250 litre aquarium in artificial seawater (Instant Ocean, Aquarium Systems, Mentor, OH). The aquarium was maintained at temperature of 17 °C and a salinity of 34ppt, corresponding to conditions that *Nautilus* experience in their native habitat. *Nautilus* were fed twice weekly with whole shrimp. The *Nautilus* were initially unable to maintain neutral buoyancy in the aquarium, a common problem with captive *Nautilus* (Carlson, 2010), but regained their buoyancy control after 8 weeks in the lab aquarium. Experiments on their swimming took place following this.

5.3.2 Particle Image Velocimetry (PIV)

PIV experiments took place in a 126 litre (610×460×450mm, length×width×height) glass aquarium. The temperature and salinity of the experimental aquarium matched that of the holding tank. *Nautilus* were transferred to the experimental tank and allowed to acclimatise for a minimum of 15 minutes. As *Nautilus* are olfactory foragers (Basil et al., 2000), a shrimp was added to the water to stimulate swimming and this elicited a variety of swimming behaviours, e.g. swimming anteriorly and swimming posteriorly, to be investigated.

Quantitative data of the jet structure of *Nautilus* was obtained using two-dimensional PIV. The swimming area was calibrated in mm by recording an image of a 2D calibrated target (14x14mm square grid with the tank was full of water). The experimental tank was seeded with aluminium oxide (Sigma-Aldrich, Poole ,Dorset, UK) with an average particle size of 5μm at a density of 30mg per litre. Particles were illuminated with a 1W continuous 532nm, green laser (Shanghai Dream Lasers Technology Co., Ltd., Shanghai, People's Republic of China) directed through a Powell lens (Thorlabs, Inc., Newton, NJ, USA) creating a 1mm thick, vertically orientated light sheet. The aim was to visualise the wake of swimming *Nautilus* in the sagittal plane and only those sequences in which the laser bisected the jet orifice and thereby the middle of the vortex structures were used for analysis. The *Nautilus* and particle movements were filmed using a Photron FASTCAM SA3 (Photron USA, San Diego, CA, USA) high speed camera recording at 500 frame s^{-1}, shuttered at 1/500 s, recording at 1280 x 1024 pixel resolution.

The positional data of the illuminated particles were analysed using PIVlab (Thielicke & Stamhuis, 2012), an open source program written in MATLAB (R2012a; The Mathworks, Inc., Natwick, MA, USA). The image sequences were pre-processed with a contrast-limited adaptive histogram equalisation tool to enhance contrast. The body of the *Nautilus* was masked on the images to eliminate edge effects. A cross correlation technique was used with adaptive multi-pass processing to analyse image pairs and to track particle movement between frames. A total of three passes were used to analyse images, with an initial interrogation window of 128 x 128 pixels and a final size of 32 x 32 pixels with a 50% overlap between each pass. A standard deviation filter was used to remove vectors that were more than 7 deviations away from the mean flow. 0.43±0.02% of the vectors were found to be erroneous in an 1800 x 1800 vector frame. Missing velocity vectors were then interpolated using a boundary value solver.

5.3.3 Jet properties and swimming efficiency

Jet thrust (*T*), is the force propelling the animal and equals the rate of change of momentum in the surrounding fluid, and was calculated as:

$$T = \rho \bar{u}_j^2 A_j \qquad [5.1]$$

where ρ is seawater density (1025 kg m^{-3}), $\bar{u}_j$ is the average jet velocity calculated by taking the time average of the average jet core velocity during the jet period and A_j is the cross sectional area of the jet orifice, measured in ImageJ (ImageJ, Bethesda, Maryland, USA) from images taken of each nautilus with the jet orifice perpendicular to the camera (Sutherland and Madin, 2010).

Whole cycle hydrodynamic (η_{wc}) efficiency was calculated following a method developed for jet propulsion swimming, in which account is taken of the acceleration of the water during both the refilling and contraction phases of the swimming cycle (Alexander, 2003). The approach developed by Alexander (2003) to calculate squid whole cycle propulsive efficiency incorporates the losses associated with acceleration of water during the refilling phase of the cycle and is calculated as:

$$\eta_{\mathrm{WC}}=\frac{2\bar{U}\bar{u}_{\mathrm{j}}}{2\bar{U}\bar{u}_{\mathrm{j}}+\bar{u}_{\mathrm{r}}^{2}+\bar{u}_{\mathrm{j}}^{2}} \qquad [5.2]$$

Where $\bar{U}$ is the time averaged velocity of the animal, $\bar{u}_r$ is the refill velocity, i.e. the velocity of the fluid at the intake orifice during the refilling of the mantle. Difficulty in visualising the flow near the refill orifices of the *Nautilus* meant measurements of refill velocities could not be obtained via PIV in the current investigation and therefore had to be estimated. It was assumed that the total volume of water ejected during jetting was equal to the volume of water taken in to the mantle during refilling. Therefore, the refill velocity could be estimated as follows:

$$\bar{u}_{\mathrm{r}}=\frac{\bar{u}_{\mathrm{j}}A_{\mathrm{j}}t_{\mathrm{j}}}{A_{\mathrm{r}}t_{\mathrm{r}}} \qquad [5.3]$$

where A_r is the area of the refill orifice and t_j and t_r are the durations of the jetting and refill periods, respectively. Jet duration (t_j) was calculated as the time interval between the beginning of contraction of the head to within the mantle cavity to the beginning of relaxation of the head to its initial position. The refill duration (t_r) was calculated as the beginning of relaxation the start of the next contraction cycle. The sum of these two time periods represents the total cycle duration (t_{cd}). The duty cycle was defined as the ratio between the duration of the jet period and the total cycle duration.

Slip (S), an indicator of the inverse of the propulsive efficiency, was calculated from $\bar{u}_\mathrm{j}$ and $\bar{U}$ (Bartol et al., 2009b) as:

$$S = \frac{\bar{u}_\mathrm{j}}{\bar{U}} \qquad [5.4]$$

Formation number was calculated as:

$$F = \frac{L_\mathrm{j}}{D_\mathrm{j}} \qquad [5.5]$$

where L_j is the jet length measured as the extent of the vorticity field along the jet centreline and D_j is the diameter of the vortex ring measured from the two peaks of vorticity that make up the ring (Bartol et al., 2009b).

Jet angle (β) is the angle of the jet relative to the swimming path of the *Nautilus*.

5.3.4 Statistical analyses

Statistical analysis was carried out in SPSS for Mac (IBM SPSS Statistics for Mac, Version 21.0. Armonk, NY). Data were checked for normality using a Shapiro–Wilks test. Data were fitted with linear regressions and tested using one-way ANOVA to determine if a significant difference existed between means. If a difference was detected, Tukey's post-hoc tests were used to identify where these differences occurred. All data are reported as mean ± s.e.m.

5.4 Results

In total 4 *Nautilus* were filmed swimming posterior first, whilst only 3 were filmed swimming anterior first, swimming at mean *Re* of 6.7 x 10^3.

Table 5.1. *Nautilus* morphology and swimming kinematics.

	Posterior First	Anterior First
Shell diameter (cm)	9.15 ± 0.58	9.28 ± 0.6
Swimming Speed (BL s^{-1})	0.90 ± 0.12	0.73 ± 0.05
Jet orifice area (cm^2)	1.03 ± 0.08	0.58 ± 0.15
Jet refill orifice area (cm^2)	3.75 ± 0.43	3.98 ± 0.83
Cycle frequency (Hz)	1.51 ± 0.05	1.21 ± 0.06
Duty Cycle[a]	0.51 ± 0.01	0.52 ± 0.01

[a] Duty cycle, the proportion of the swimming cycle that is made up of the power stroke

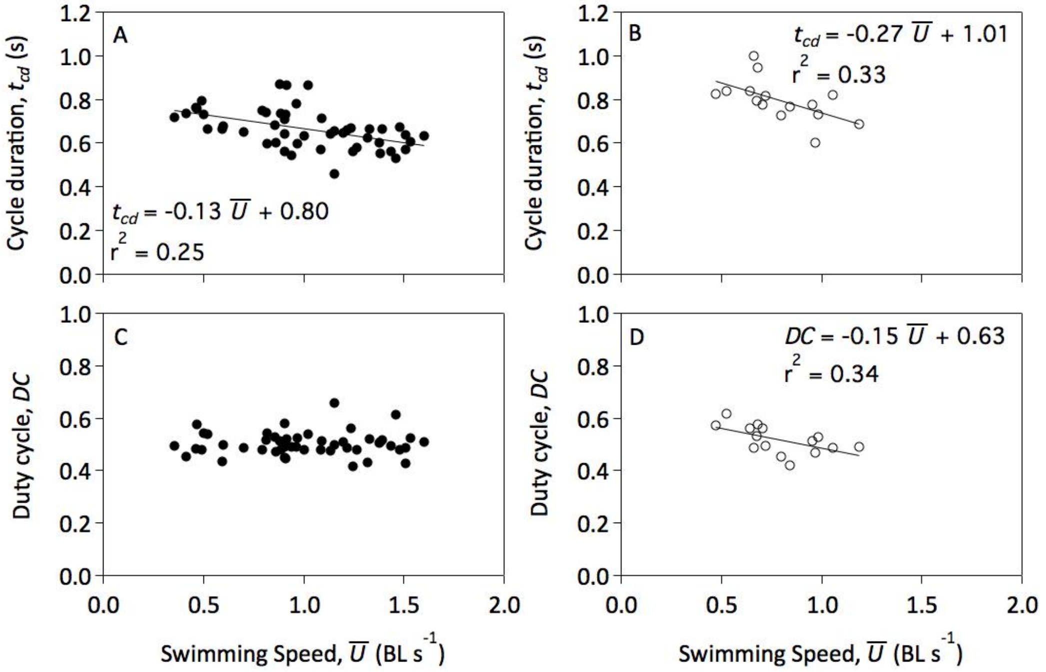

Figure 5.2. Swimming mechanics as a function of swimming speed in *Nautilus.* Cycle duration plotted as a function of swimming speed for posterior first (A) and anterior first swimming (B). Duty cycle plotted as a function of swimming speed for posterior first (C) and anterior first (D) swimming.

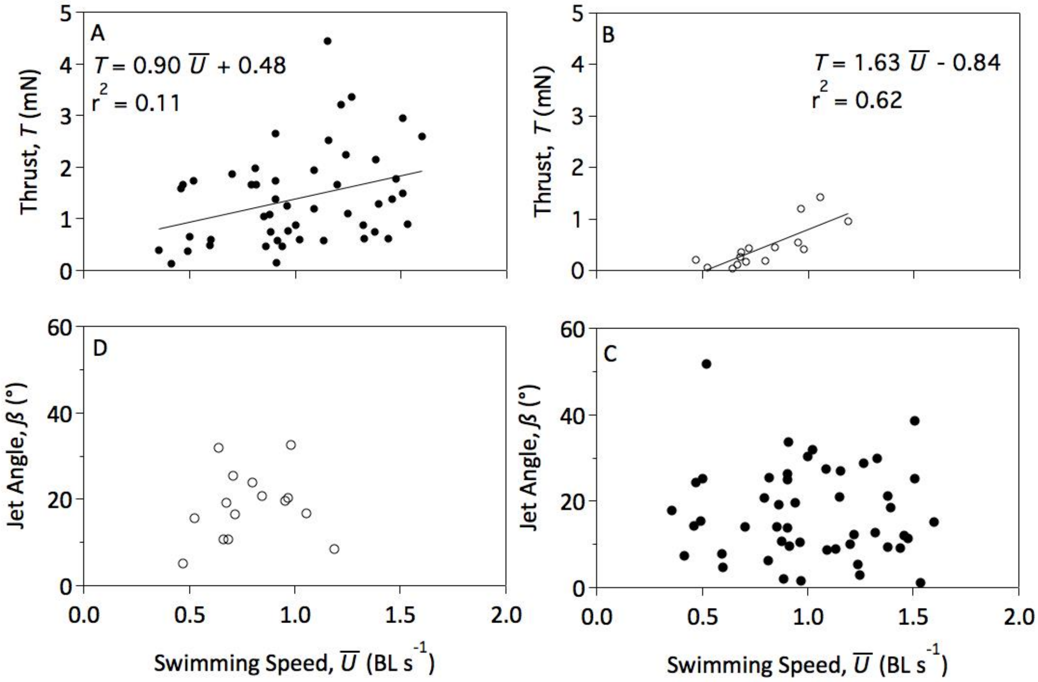

Figure 5.3. Swimming mechanics as a function of swimming speed in *Nautilus.* Thrust plotted as a function of swimming speed for posterior first (A) and anterior first (B) swimming. Jet angle in relation to swimming direction plotted as a function of swimming for posterior first (C) and anterior first swimming (D).

During swimming two distinct propulsive orientations were observed, with animals swimming either 'anterior first' or 'posterior first'. Posterior first swimming was the most frequently observed with 49 sequences captured, whereas only 15 were recorded during anterior first swimming. Average swimming speed during posterior first swimming was 0.90 ± 0.12 BL s^{-1} (range = 0.35-1.60 BL s^{-1}) and 0.73 ± 0.05 BL s^{-1} (range = 0.48-1.19 BL s^{-1}) during anterior first swimming. Cycle duration decreased with increasing swimming speed for both posterior first ($F_{1,47}$ = 15.28, p<0.001; fig. 5.2A) and anterior first ($F_{1,13}$ = 7.01, p<0.05; fig. 5.2B). Duty cycle during posterior first swimming was 49.73 ± 0.86% (range = 41.72-65.79 %) and 51.76 ± 1.12 (range = 41.88-61.72 %) for anterior first swimming. Duty cycle was independent of swimming speed during posterior first swimming (p=0.91; fig. 5.2C) but decreased with increasing swimming speed during anterior first swimming, ($F_{1,13}$ = 6.50, p<0.05; fig. 5.2D). Thrust increased with increasing swimming speed in both posterior first ($F_{1,47}$ = 5.82, p<0.05; fig. 5.3A) and anterior first swimming ($F_{1,13}$ = 23.99, p<0.001 fig. 3B). Mean jet angle was 16.15 ± 1.58° (range = 1.13-33.69°) in posterior first swimming and 16.79 ± 2.50° (range = 5.09-32.47°) in anterior first swimming. Jet angle was independent of swimming speed for both posterior first (p=0.219; fig. 5.3C) and anterior first swimming (p=0.138; fig. 5.3D).

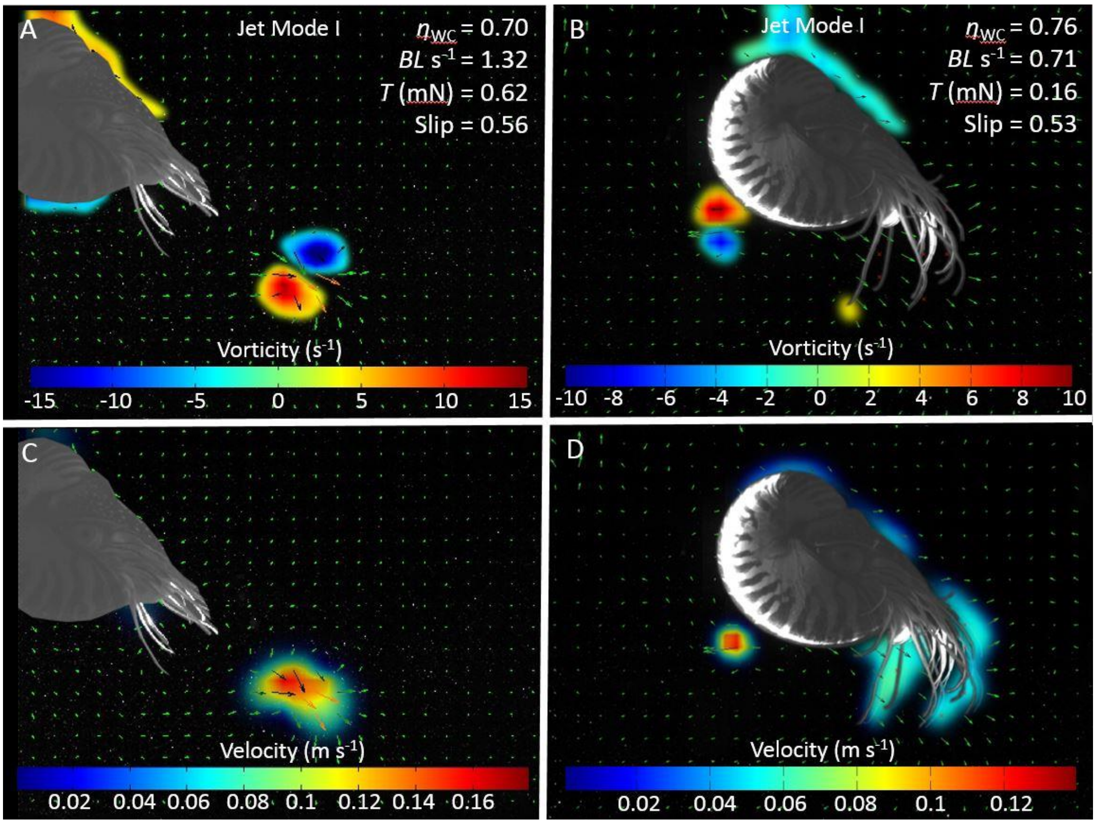

Figure 5.4. Vorticity and velocity fields of jet mode I jets produced during swimming in *Nautilus.* Jets formed during posterior first (A,C) and during anterior first (B,D) swimming. On vorticity plots red and blue regions denote clockwise and counter clockwise rotation respectively.

5.4.1 Jet wake properties

Visualisation of the jets of swimming *Nautilus* revealed two categories of jet structures: jets in which all of the ejected fluid rolled up into an isolated vortex ring (termed 'jet mode I' jets; fig. 5.4); and jets that consisted of an elongated jet of ejected fluid (termed 'jet mode 2' jets; fig. 5.5). Both types of jet were observed during both posterior (fig. 5.4A, C; fig. 5.5A, C) and anterior first (fig. 5.4B, D; fig. 5.5B, D) swimming behaviours.

During posterior first swimming formation number ranged from 0.79-2.16 in jet mode 1 jets and 3.16-6.29 in jet mode 2 jets. During anterior first swimming formation number ranged from 1.08-1.52 during jet mode 1 swimming and 3.29-5.51 during jet mode 2 swimming.

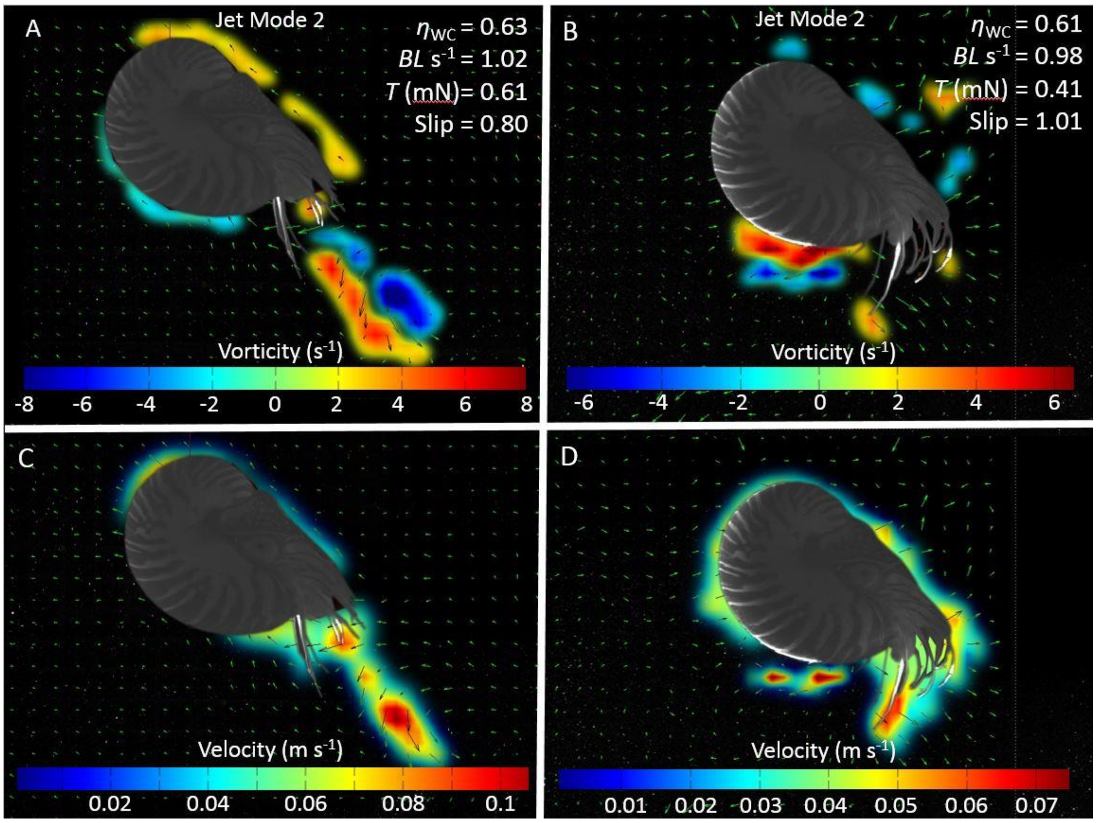

Figure 5.5. Vorticity and velocity fields of jet mode 2 jets produced during swimming in *Nautilus.* Jets formed during posterior first (A,C) and during anterior first (B,D)swimming. On vorticity plots red and blue regions denote clockwise and counter clockwise rotation respectively.

5.4.2 Propulsive efficiency

The mean area of the refill orifice during refilling was determined from still images of *Nautilus* during swimming and was approximately 4 times the mean jet orifice area during posterior first swimming and 7 times the area during anterior first swimming (table 5.1). Refill velocity (estimated using equation 4) was 0.16 - 0.36 times the jet velocity; these estimations were then used to calculate whole-cycle propulsive efficiency in *Nautilus*.

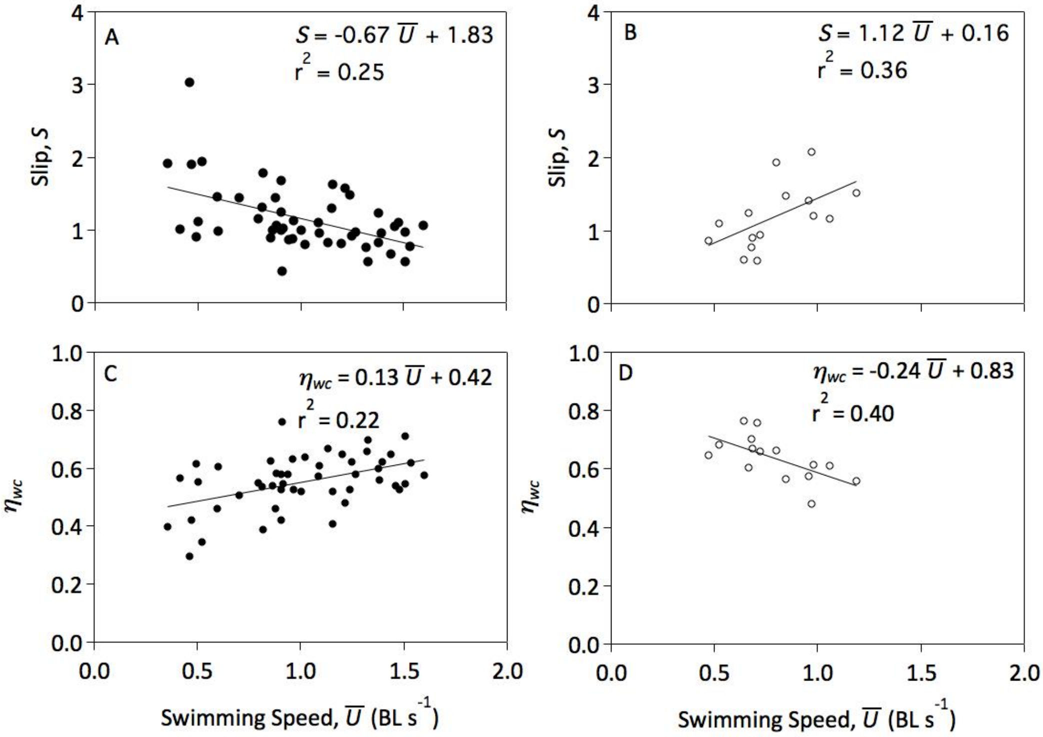

Figure 5.6. Slip and swimming efficiency as a function of swimming speed in *Nautilus*. Slip as a function of swimming speed for posterior first (A) anterior first swimming (B). Hydrodynamic propulsive efficiency η_{wc} as a function of swimming speed for posterior first (C) anterior first swimming (D).

Slip decreased with increasing swimming speed during posterior first swimming ($F_{1,47}$ = 15.82, $p<0.001$; fig. 5.6A), but increased with increasing swimming speed during anterior first swimming ($F_{1,13}$ = 9.42, $p<0.05$; fig. 5.6B). Mean slip during posterior first swimming was 1.14 ± 0.09 (range = 0.44-3.03) and during anterior first swimming was 1.05 ± 0.10 (range = 0.51-1.95). During posterior first swimming propulsive efficiency increased with increasing swimming speed ($F_{1,47}$ = 11.46, $p<0.05$; fig. 5.6C). In contrast, propulsive efficiency decreased with increasing swimming speed during anterior first swimming ($F_{1,13}$ = 114.53, $p<0.05$; fig. 5.6D).

5.4.3 Jet mode and swimming performance

Propulsive efficiency was found to vary with swimming orientation and jet mode ($F_{3,9}$ =4.62, $p<0.05$; fig. 5.7A). Anterior first jet mode 1 swimming was shown to be more efficient than posterior first jet mode 2 swimming ($p<0.05$; fig. 5.6C, D; fig. 5.7A). Thrust was also found to vary with swimming orientation and jet mode ($F_{3,9}$ =7.01, $p<0.05$; Fig. 5.7B) Anterior first jet mode 1 swimming was found to produce less thrust than posterior first jet mode 2 swimming ($p<0.05$; Fig. 5.7B). Slip was independent of swimming orientation and jet mode ($F_{3,9}=1.41$, $p=0.302$; fig. 5.6A, B).

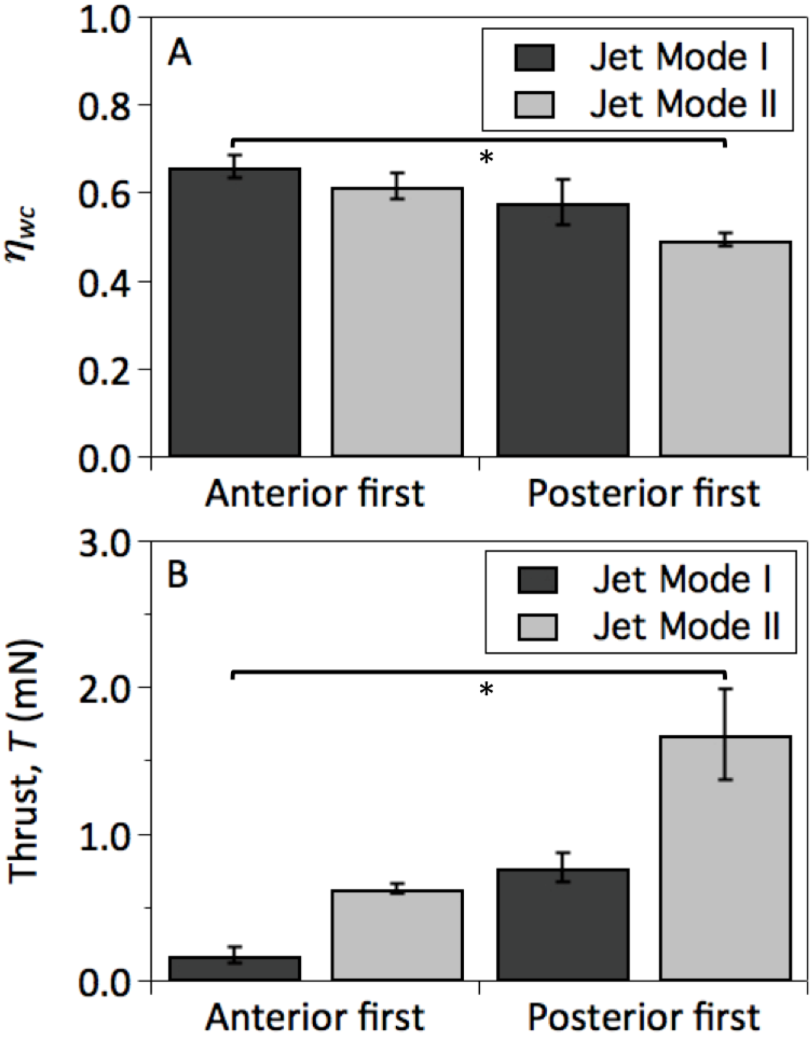

Figure 5.7. Swimming efficiency and thrust during swimming as function of jet mode in *Nautilus.* Hydrodynamic propulsive efficiency (η_{wc}) as a function of jet mode for posterior first and anterior first swimming (A). Thrust as a function of jet mode for posterior first and anterior first swimming (B). Error bars represent ±1 s.e.m..

During posterior first swimming, there was no evidence of a particular jet mode preference across swimming speeds, as both jet modes were observed across a range of overlapping speeds. However, during anterior first swimming, jet mode 1 jets were never seen at speeds exceeding 0.8 BL s^{-1}, whilst jet mode 2 jets were identified at speeds ranging from 0.47-1.19 BL s^{-1}.

5.5 Discussion

The nautiloids are the most primitive living cephalopods (Ward, 1984). Whilst other members of the class Cephalopoda have lost their shells, favouring increased swimming speed, the nautiloids are the only representatives to have retained an external shell. Despite the retention of the external shell in *Nautilus*, they share a common locomotor strategy with their extant coleoid relatives. As scavengers, they are reliant on infrequently available food sources so they need to be economical, it is expected that this would be reflected by their locomotion.

5.5.1 Jet Modes

Two different structures were identified during jet propulsion swimming: jet mode 1 jets, in which all of the ejected fluid rolls up into an isolated vortex ring (fig. 5.4), and jet mode 2 jets, where fluid is ejected as an elongated jet (fig. 5.5). These two jet modes were comparable to the jet modes observed in free-swimming brief squid (Bartol et al., 2009a, 2009b). In *Nautilus* it was found that thrust tended to be higher during jet mode 2, compared with jet mode 1, with jet mode 2 jets produced during posterior first swimming producing significantly more thrust than jet mode 1 jets during anterior first swimming. There was also a significant difference in swimming efficiency across jet modes and swimming orientation, with jet mode 2 jets produced during posterior first swimming being significantly less efficient than jet mode 1 jets during anterior first swimming. This is similar to juvenile and adult squid (Bartol et al., 2009b), where higher efficiencies but lower thrusts were exhibited whilst swimming via jet mode I swimming compared to jet mode 2. Conversely, a self propelled jetting vehicle known as 'Robosquid' was shown to have an increase in both efficiency and thrust at formation numbers that correspond to jet mode 1, just below the transition to jet mode 2 jets (Nichols et al., 2008). The lack of a difference in whole cycle efficiency and thrust generation between the two modes may explain why the jet mode was not exclusively related to swimming speed across both swimming orientations. The highest swimming speeds that *Nautilus* has been reported to use is 30 cm s^{-1} (O'Dor et al., 1990), compared with the 3 to 17 cm s^{-1} measured here. Whether this has an impact on whole cycle efficiency, thrust generated or the preferred jet mode is unknown.

In *Nautilus* the transition from jet mode 1 to jet mode 2 jets occurred at formation numbers between 2 and 3. Other jet propulsion swimmers have also been reported to exhibit a transition between these two jet modes at formation numbers of approximately 3 (e.g. squid, Bartol et al., 2009). A formation number of 3 is similar to the transition between jet mode I and jet mode 2 in mechanically produced jets (3.6 to 4.5, Krueger and Gharib, 2003); above formation number ratios of around 4, the limit at which the vortex ring can grow is reached, circulation stops being entrained to the vortex ring and separates from the rest of the jet. It has been demonstrated that producing jets with formation numbers of approximately 4 optimises pulse-averaged thrust in which jets can produce more thrust per unit of expelled fluid than elongated jets lasting longer in duration (Krueger and Gharib, 2003). However, while *Nautilus* have the potential to be able to produce jet structures near $F = 4$, there seems to be little benefit in doing so in terms of enhanced thrust production.

5.5.2 Propulsive efficiency

Average hydrodynamic swimming efficiencies were 0.51 ± 0.02 (range = 0.29-0.66) in posterior first swimming and 0.61 ± 0.02 (range = 0.45-0.68) during anterior first swimming (fig. 5.6). These values are higher than those reported in squid when refilling period was accounted for, with swimming efficiencies in squid being calculated as 0.42-0.49 (Anderson and Grosenbaugh, 2005) and 0.38-0.44 (Anderson and Demont, 2000). Intriguingly, propulsive efficiency increases as a function of speed in posterior first swimming, but decreases as a function of speed during anterior first swimming. The differences appear to be as a consequence of variability in slip across swimming speeds in both swimming orientations. Slip is a measure of wasted kinetic energy in the wake produced by the jets, during posterior first swimming slip decreases as a function of speed, whereas in anterior first swimming, slip increases as a function of speed (fig. 5.6C, D). In other studies on jet propelling squids, slip tends to decrease as speed increases, resulting in an increase in efficiency (Bartol et al., 2008). This trend is matched during posterior first swimming in

Nautilus, but seemingly reversed during anterior first swimming. These results are different from those comparing swimming orientation in squid, in which swimming efficiency was found to increase with increase swimming speed irrespective of swimming orientation (Bartol et al., 2016).

The differences in slip with swimming orientation are intriguing. One aspect of the swimming mechanics of posterior and anterior first swimming to consider is the size and shape of the funnel. During anterior first swimming the funnel is turned back on itself, creating a bend that the fluid must pass through before getting ejected and propelling the animal forward. Fluid flows in pipes that are forced to change direction experience energy losses as the bend produces turbulence in the fluid, these losses become greater as fluid velocity increases (Itō, 1960). During anterior first swimming, losses in energy due to turbulence produced as the ejected fluid negotiates the bend of the funnel may increase as a function of swimming speed and that may reduce propulsive efficiency with increasing swimming speed.

Another explanation for the inverse relationship between swimming speed and whole cycle propulsive efficiency across swimming orientations could lie within the differences in swimming mechanics between the two orientations. Anderson and Grosenbough (2005) investigated how slip could be reduced during jet propulsion swimming in cephalopods, thereby increasing their propulsive swimming efficiency. It was noted that decreasing the volume flow rate of fluid ejected by increasing the jet period reduced slip, resulting in a jet of fluid being ejected at a relatively slower speed. This would require an increase in flow rate during refilling, due to the shorter refill period. In order for the gains in reduced slip to outweigh the losses of the refill period, the refill orifice area would have to be increase. In the anterior first swims in which the highest whole cycle efficiencies were recorded in *Nautilus*, both duty cycle and jet period decreased with increased swimming speed (Fig. 5.2). This means that at their slowest swimming speeds, *Nautilus* spent more time ejecting fluid than refilling, resulting in a low speed jet being ejected, followed by an increase in the volume flow rate during refilling. In addition to this, the refill orifice is relatively bigger than the jet orifice during anterior first swimming in comparison to posterior first swimming. This is not due to a change in the refill orifice area, but rather a reduction in the jetting orifice area. During anterior first swimming, the jet orifice area is approximately half of that during posterior first swimming, whereas the refill orifice area was constant during both swimming orientations. This results in the refill orifice being approximately seven times the area of the jetting orifice during anterior first swimming, compared with approximately four times the area during posterior first swimming (table 5.1).

Therefore, it appears that at slow speeds, *Nautilus* are able to adopt a swimming style that increases whole cycle efficiency through a reduction of slip. As swimming speed increases the benefit is lost, as *Nautilus* shift to using a shorter jet period with a higher velocity jet, leading to a reduction in whole cycle efficiency.

There was no relationship found between swimming speed and jet angle. Previous studies of squid locomotion have found a decrease in jet angle with increased swimming speed (Bartol et al., 2008). Higher jet angles at lower swimming speeds are necessary to counteract the negative buoyancy of squid, with higher angles being required at slower speeds to prevent sinking, enabling the squid to maintain its position within the water column. Jets directed at steep angles in relation to body orientation in addition to highly angled body orientation for body lift generation at low speeds lead to high energetic costs (Bartol et al., 2001). The neutrally buoyant *Nautilus* does not need to adjust its jet angle to produce increased lift at slow swimming speeds. Consequently, large ranges of jet angles are observed at all swimming speeds in both anterior first and posterior first swimming. The energetic benefits of being neutrally buoyant are more pronounced at slow speeds due the high cost of swimming slowly in squid. However, at higher speeds it would be expected that animals like squid would gain an advantage, owing to their streamlined bodies that are capable of producing hydrodynamic lift at high speeds (Stewart et al., 2010), whereas the external shell would likely serve as a hindrance due to the increase in drag associated with the relatively higher frontal area.

5.5.3 Implications for *Nautilus* Life History

The metabolic cost of locomotion in *Nautilus* at the animal's typical foraging swimming speed is much lower than that in either jet propelled squid (Webber and O'Dor, 1986), or the undulatory swimming salmon (Brett and Glass, 1973). The low metabolic cost of locomotion in *Nautilus* occurs despite its use of jet propulsion and presumed lower Froude efficiency in comparison with undulatory swimmers (Webber and O'Dor, 1986). The animal's neutral buoyancy and efficient use of the muscles involved in jetting have been suggested as potential explanations for the low cost of locomotion (Webber and O'Dor, 1986). However, our study demonstrating that *Nautilus* has a high propulsive efficiency at low speeds offers an alternative or additional explanation, and it is noteworthy that the swimming orientation and speed that we found to yield the highest whole cycle efficiency also correspond to those at which the lowest metabolic cost of locomotion were measured (O'Dor and Weber, 1986). Slow anterior first swimming yielded whole cycle efficiencies that were comparable to high-speed posterior first swimming, coupling increased whole cycle efficiency with low slip. The inverse relationships between swimming speed and swimming efficiency across swimming orientation may be of an energetic benefit to *Nautilus*. The highest swimming efficiencies were reported at slow anterior first swimming, likely to be used during foraging, and high posterior first swimming, which may be employed when trying to evade predators. The cost for searching for food within its habitat is extremely low for a *Nautilus*. It seems that *Nautilus* have persisted due to their ability to exploit the niche in which they exist, expending as little energy as possible through the use of low power output, slow, but comparatively efficient swimming.

5.5.4 Summary

The evidence gathered here suggests that *Nautilus* are geared towards a life of slow cruising rather high speed activity, with high swimming efficiencies being found during typical foraging swimming orientation. One topic of further investigation would be the differences associated with different swimming modes that have been previously identified as being employed by *Nautilus*. The swims investigated in this study probably don't represent the very upper limit in *Nautilus* swimming performance, as they were generally cruising at intermediate speeds with jets formed through the compression of the ‘wings’ that make up the funnel. Swimming in *Nautilus* via jets formed through the withdrawal of the head into the mantle cavity are likely only performed as an escape response when high speeds would be desirable. This shift in swimming strategy could be considered akin to a shift in gait that is seen in other animal locomotion and would likely produce interesting results. Its seems reasonable to assume that a jet formed from the head retractor muscles may have different properties to those identified in this study, yielding variations in swimming performance not yet identified.

Chapter 6

Jet-paddling jellies: swimming performance in the Rhizostomeae jellyfish *Catostylus mosaicus*

6.1 Abstract

Jellyfish are a successful and diverse class of animals that swim via jet propulsion through the rhythmic pulsing of their bell, which produces thrust. Members of the order Rhizostomeae are characterised by a lack of tentacles and the presence of eight oral arms at the centre of their bell. The implications of this body morphology on the mechanisms by which thrust is produced have not been extensively studied. Here we used particle image velocimetry to characterise wake structures during swimming in the Rhizostomeae jellyfish *Catostylus mosaicus*. During swimming there was a complex interaction between the starting vortex and the stopping vortex from the previous cycle, resulting in regions of high velocity along the line of interaction of the opposite signed vortices. The relaxation phase of the swimming cycle was shown to have important implications for propulsion of the animal, with significant thrust being produced during this phase via the circulation of the stopping vortex within the subumbrella cavity. In addition, this species is capable of exploiting a type of passive energy recapture, in which swimming velocity increases at the end of the cycle, despite the lack of movement of the bell. The enhanced circulation and thrust is achieved through movement of the flexible bell margin, which is able to manipulate the stopping vortex to within the subumbrella cavity during bell relaxation. These mechanisms improve swimming efficiency in this species by recapturing energy expelled during the power stroke and using it to increase swimming speed.

6.2 Introduction

Pulsed jet propulsion is utilised by many aquatic organisms across a wide range of sizes, from tiny medusa to large squid (Bone and Trueman, 1983; Bartol et al., 2001; Dabiri et al., 2005). Propulsion is achieved by compressing a fluid filled cavity, which creates a pressure difference between the cavity and the external medium, forcing a jet of water out of the cavity and transferring momentum to the environment. The wake of jet-propelled organisms is often characterised by the presence of vortex rings, a toroidal ring of rotating fluid, originating at the jet orifice during propulsion (Bartol et al., 2009b; Dabiri et al., 2010; Sutherland and Madin, 2010). The formation of vortex rings via pulsed jet propulsion has been shown to bring an increase in thrust in comparison to that produced by a steady jet per unit of ejected fluid (Krueger and Gharib, 2003). The increased thrust results from entrainment of ambient fluid into the vortex ring, which in turn increases the mass of fluid that is driven backwards in the wake of the jet. However, there is a limit on the growth of a vortex ring by entrainment and, once this limit is reached, vortex ring ‘pinch-off’ occurs with any remaining fluid from the jet being ejected as a trailing jet (Dabiri and Gharib, 2004a; Gharib et al., 1998). Thrust decreases once pinch off has occurred, as the trailing jet of fluid contributes little to the overall thrust of the jet. Vortex pinch-off depends on the critical dimensional parameter, the formation number (*F*; Krueger and Gharib, 2003). Using mechanically generated jet pulses it has been demonstrated that above *F* ~4, pinch-off occurs and a trailing jet is formed (Krueger and Gharib, 2003).

Jellyfish are excellent organisms in which to investigate the mechanism of locomotion by jet propulsion in fluids. Medusae utilise jet propulsion through the alternate contraction and expansion of the bell. Contraction increases pressure on the fluid in the subumbrella cavity, forcing water out of an orifice at the oral end of the animal. The inner surface of the bell has a layer of muscle cells (radial and circular muscle fibres), with the circular fibres providing most of the power for swimming (Alexander, 1969). Contraction of the muscles deforms the mesoglea; when the muscles relax, the elasticity of the mesoglea expands the bell. Medusae have traditionally been considered as poor locomotory performers, with a hydrodynamic efficiency ranging from 0.09 to 0.53 (Dabiri et al., 2010); in comparison, undulatory fish, have a hydrodynamic efficiency of 0.8 (Videler and Hess, 1984; Webb et al., 1984). However several species of medusa delay pinch off by manipulating the shape of the orifice through which water is ejected, increasing the size of the vortex ring, suggesting that an increase in hydrodynamic efficiency by maximising the thrust of propulsion may be possible (Dabiri et al., 2006).

An additional energy saving mechanism has been identified in Medusae with oblate bells (where the bell height is less than its width) that are also characterised by having a flexible bell margin. These species swim with a jet-paddling form of locomotion that produces a more complex wake structure than those species with prolate bells (Colin and Costello, 2002; McHenry and Jed, 2003). During the relaxation phase of the swimming cycle where the bell expands passively, a second vortex, known as a stopping vortex is formed. The stopping vortex has opposite rotational direction to the starting vortex (created during bell contraction) and acts to refill the bell. The stopping vortices initially form on the outside of the bell, but are repositioned by the flexible bell margin to the subumbrella cavity during bell expansion. This increases the pressure in the subumbrella cavity, resulting in thrust generation and forward movement of the medusa (Gemmell et al., 2014). This passive energy recapture reduces the metabolic cost of locomotion (*CoL*) in moon jellyfish (*Aurelia aurita*) by around 48% (Gemmell et al., 2013).

Thrust production can also be augmented if successive vortex rings are closely spaced (less than 3 vortex ring radii apart) due to the velocity induced on adjacent vortices in the wake, in comparison to an isolated vortex ring (Weihs, 1977). A study of flow patterns generated by jellyfish (Dabiri et al., 2005) showed that the interactions between stopping and starting vortices could result in reduced propagation of downstream wake vortices, resulting in close spacing between adjacent vortices. The authors did not investigate further the possibility of this interaction having thrust augmenting effects as proposed by Weihs (Weihs, 1977) and noted that that Weihs' predictions were based around single-sign vortex rings, not the co-joined vortices that they had observed during swimming (Dabiri et al., 2005).

The aims of this study were to characterise the wake structure and thrust producing mechanisms of the blue blubber jellyfish (*Catostylus mosaicus*, Quoy and Gaimard 1824; order Rhizostomeae). This species has a morphology quite unlike that of any species studied to date. Lacking tentacles, *C. mosaicus* instead possess four oral lobes that converge over a central mouth, with eight branching oral arms that transport food to the mouth via a canal like system (Lee et al., 2008). These feeding structures represent a much larger proportion of the overall mass of the organism compared with many other species (Daniel, 1985; Arai, 1997). The bell of *C. mosaicus* is almost spherical in shape, with a bell height approximately 60% of the bell diameter; while still considered an oblate species, *C. mosaicus* has a morphology that is intermediate between that of typical prolate and oblate species. Additionally, *C. mosaicus* is a more active species than those that have previously been studied, with a relatively high pulsing frequency of around 2-3Hz. It was hypothesised that the intermediate body morphology and large feeding structures of *C. mosaicus* would affect the formation of vortex structures and their interactions with one another during swimming in comparison to predominantly oblate and prolate medusae. Additionally, it was hypothesised the high pulsing frequency of *C. mosaicus* would result in closely spaced vortex rings, potentially providing a benefit in swimming performance to the animal during locomotion.

6.3 Materials and methods

6.3.1 Animals

Blue blubber jellyfish (*Catostylus mosaicusii*, Quoy and Gaimard 1824) (Glass Ocean Ltd., London, UK) were housed in a 250 litre kreisel aquarium in artificial seawater (Instant Ocean, Aquarium Systems, Mentor, OH). The aquarium was maintained at temperature of 25 °C and a salinity of 34ppt, corresponding to conditions that the jellyfish would experience in their native habitat (Southcott, 1982). Jellyfish were fed daily with freshly hatched baby brine shrimp. Relaxed bell diameter of the jellyfish ranged from 2.3 – 4.6 cm (mean diameter 3.5 ± 0.35). Jellyfish were allowed to acclimate to the laboratory conditions for a minimum of one week before the experiments took place.

6.3.2 Particle Image Velocimetry (PIV)

Quantitative jet structure of the jellyfish was obtained using two-dimensional particle image velocimetry (PIV). PIV experiments took place in 126 litre (610 × 460 × 450mm) glass aquarium. A smaller working section was created using egg crate in order to increase the likelihood of the jellyfish passing through the laser sheet. This section was 16 litres (160 × 450 × 220 mm) in volume. This successfully restricted the swimming area for the jellyfish whilst still being large enough to ensure that wall effects were avoided (Vogel, 1981). The temperature and salinity of the experimental aquarium matched that of the holding tank. Individual jellyfish were transferred to the experimental tank and allowed to acclimatise for a minimum period of 15 minutes. Recordings took place once the jellyfish was actively swimming around the experimental aquarium.

The swimming area was calibrated in mm by recording an image of a 2D calibrated target (14x14mm square grid with the tank was full of water). The experimental tank was seeded with white talcum powder at a density of 50mg per litre (Wong et al., 2012). Particles were illuminated with a 1 W continuous green (532nm) laser (Shanghai Dream Lasers Technology Co., Ltd., Shanghai, People’s Republic of China) directed through a Powell lens (Thorlabs, Inc., Newton, NJ, USA) creating a vertically oriented 1mm thick light sheet. The wake of swimming jellyfish was visualised in the vertical plane, with the light sheet orientated to bisect the animal and thus the jet. Only those sequences in which the laser crossed the central, vertical axis of the bell and thereby the middle of the vortex ring were used for analysis. The jellyfish and wake were recorded using a high speed camera (Fastcam SA3, Photron Ltd, Tokyo, Japan) operating at 500 frame s^{-1} and shuttered at 1/500 s mounted perpendicular to the laser sheet; all videos were acquired using Photron Fastcam Viewer software (Photron Ltd, Tokyo, Japan).

Fluid movements were determined using PIVlab (Thielicke and Stamhuis, 2012) an open source program written in MATLAB (R2012a; The Mathworks, Inc., Natick, MA, USA). The image sequences were pre-processed with a contrast-limited adaptive histogram equalisation tool to enhance contrast and increase the probability of detecting particles. The body of the jellyfish was masked on the images to eliminate edge effects. A cross correlation technique with adaptive, multi-pass processing was used to analyse image pairs and track particle movement between frames. A total of three passes were used to analyse images, with an initial interrogation window of 128 x 128 pixels and a final size of 32 x 32 pixels with a 50% overlap between each pass. A standard deviation filter was used to remove vectors more than 7 deviations away from the mean flow. 0.68%±0.03 of the vectors were found to be erroneous in an 1400 vector frame. Missing velocity vectors were then interpolated using a boundary value solver.

6.3.3 Propulsive force calculation

The resultant sequences of particle motion were used to characterise the jet structures produced during swimming. Maximum vorticity was taken as the peak vorticity reached by the vortex rings over the entire swim cycle (where each swimming cycle is defined to be the period from the start of one bell contraction to the start of the next bell contraction).

The propulsive force of the vortex rings was calculated following Stamhuis and Nauwelaerts (2005). The average propulsive force (F_p) was calculated by dividing the accumulated momentum (I) by the propulsion phase duration. In this instance momentum is accumulated during the contraction phase of the swim cycle (t_j), taken as the period from the beginning of bell contraction to the beginning of bell relaxation. Average force is then calculated as:

$$F_\mathrm{p} = \frac{I}{t_\mathrm{j}} = \frac{\rho \Gamma \pi \mathrm{r}^2}{t_\mathrm{j}} \quad [6.1]$$

where ρ is fluid density (1025 kg m^{-3}), Γ the circulation and r is the vortex ring radius. The circulation (Γ) of the vortex rings was calculated by intergrating tangential velocity of a path around the vortex. The momentum (I) present in the vortex ring was calculated as:

$$I = \rho \Gamma \pi \mathrm{r}^2 \quad [6.2]$$

6.3.4 Kinematics and swimming performance

The swimming kinematics of the jellyfish were determined by digitising the position of the apex of the bell, in two-dimensions, using DLTdv5 (Hedrick, 2008) in MATLAB (R2012a; The Mathworks, Inc., Natick, MA, USA). The bell diameter (A_j) during the swimming cycle was also determined by digitising the position of the extreme anterior and posterior edges of the bell margin. All positional data were smoothed by applying fourth-difference smoothing (following Rayner and Aldridge, 1985). The swimming speed of the jellyfish (U) was derived from the position of the apex of the bell, and calculated as:

$$\mathrm{U} = \frac{\sqrt{(x_\mathrm{n} - x_\mathrm{n-1})^2 + (y_\mathrm{n} - y_\mathrm{n-1})^2}}{t_\mathrm{n} - t_\mathrm{n-1}} \quad [6.3]$$

where *x* and *y* are the co-ordinates of the bell apex, *t* is time and *n* is frame number. Acceleration (*a*) of the body was calculated as:

$$a = \frac{U_\mathrm{f} - U_\mathrm{i}}{t_\mathrm{n} - t_\mathrm{n-1}} \qquad [6.4]$$

Where U_f is the final speed of the jellyfish and U_i is the initial speed.

Hydrodynamic efficiency was calculating following Alexander's (2003) method for calculating hydrodynamic efficiency in jet propelling animals that have a rearward facing jet intake and was calculated as:

$$\eta_\mathrm{WC} = \frac{2\bar{U}\bar{u}_\mathrm{j}}{2\bar{U}\bar{u}_\mathrm{j} + \bar{u}_\mathrm{r}^2 + \bar{u}_\mathrm{j}^2} \qquad [6.5]$$

where $\bar{u}_\mathrm{j}$ is the time-averaged jet velocity in the wake, $\bar{u}_\mathrm{r}$ is time averaged refill velocity of fluid into the bell, $\bar{U}$ is the time average swimming speed of the jellyfish.

Slip (*S*), an indicator of the inverse of the propulsive efficiency, was calculated from $\bar{u}_\mathrm{j}$ and $\bar{U}$ (Bartol et al., 2009b) as:

$$\mathrm{S} = \frac{\bar{u}_\mathrm{j}}{\bar{U}} \qquad [6.6]$$

Formation number was calculated as:

$$F = \frac{L_\mathrm{j}}{D_\mathrm{j}} \qquad [6.7]$$

where L_j is the jet length measured as the extent of the vorticity field along the jet centreline and D_j is the diameter of the vortex ring measured from the two peaks of vorticity that make up the ring (Bartol et al., 2009b).

Kinematic, wake structure and efficiency data were gathered from all recorded swims.

6.3.5 Statistical analyses

Statistical analysis was carried out in SPSS for Mac (IBM SPSS Statistics for Mac, Version 21.0, Armonk, NY, USA). All data are reported as mean ± s.e.m. Data were checked for normality using a Shapiro–Wilks test, *t*-tests were used to compare means. All data are reported as mean ± s.e.m.

6.4 Results

In total 74 swimming cycles from 5 individual swimming *C. mosaicus* were analysed. Using average medusa swimming speed (36.22 ± 1.22 mm s^{-1}) and the average excursion of the bell margin during swimming (8.1 ± 0.90 mm), Reynolds number and Strouhal numbers were calculated as 1184 (± 220) and 0.25 (± 0.12), respectively.

6.4.1 The wake structure of swimming *C. mosaicus*

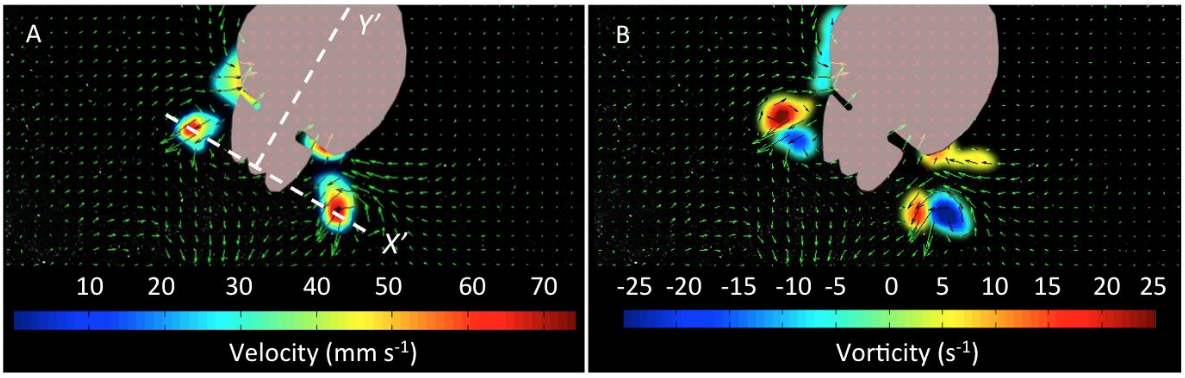

Figure 6.1. Typical Instantaneous velocity vectors (A) and vorticity fields (B) produced during components of vortex rings in free swimming in *C. mosaicus*. Red and blue regions denote clockwise and counter clockwise rotation, respectively.

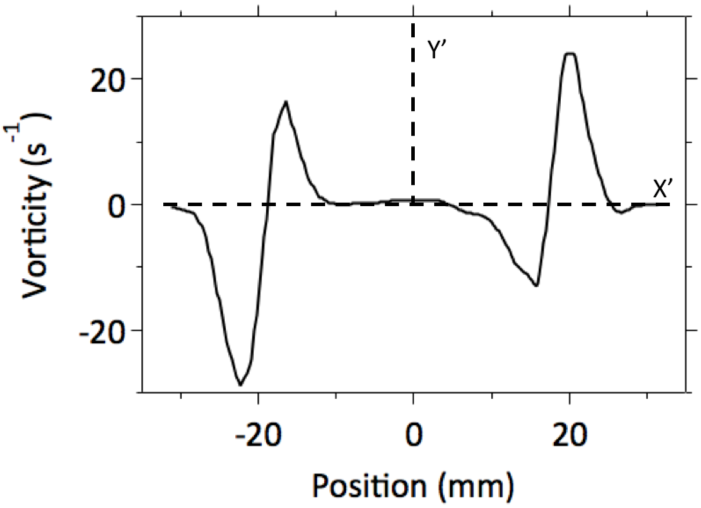

Figure 6.2. Typical vortex ring vorticity distribution across a planar section through the wake of a swimming jellyfish. Vorticity distribution along the X' axis of both vortex cores of the vortex rings. X' is the longitudinal axis that transects the centres of fluid rotation.

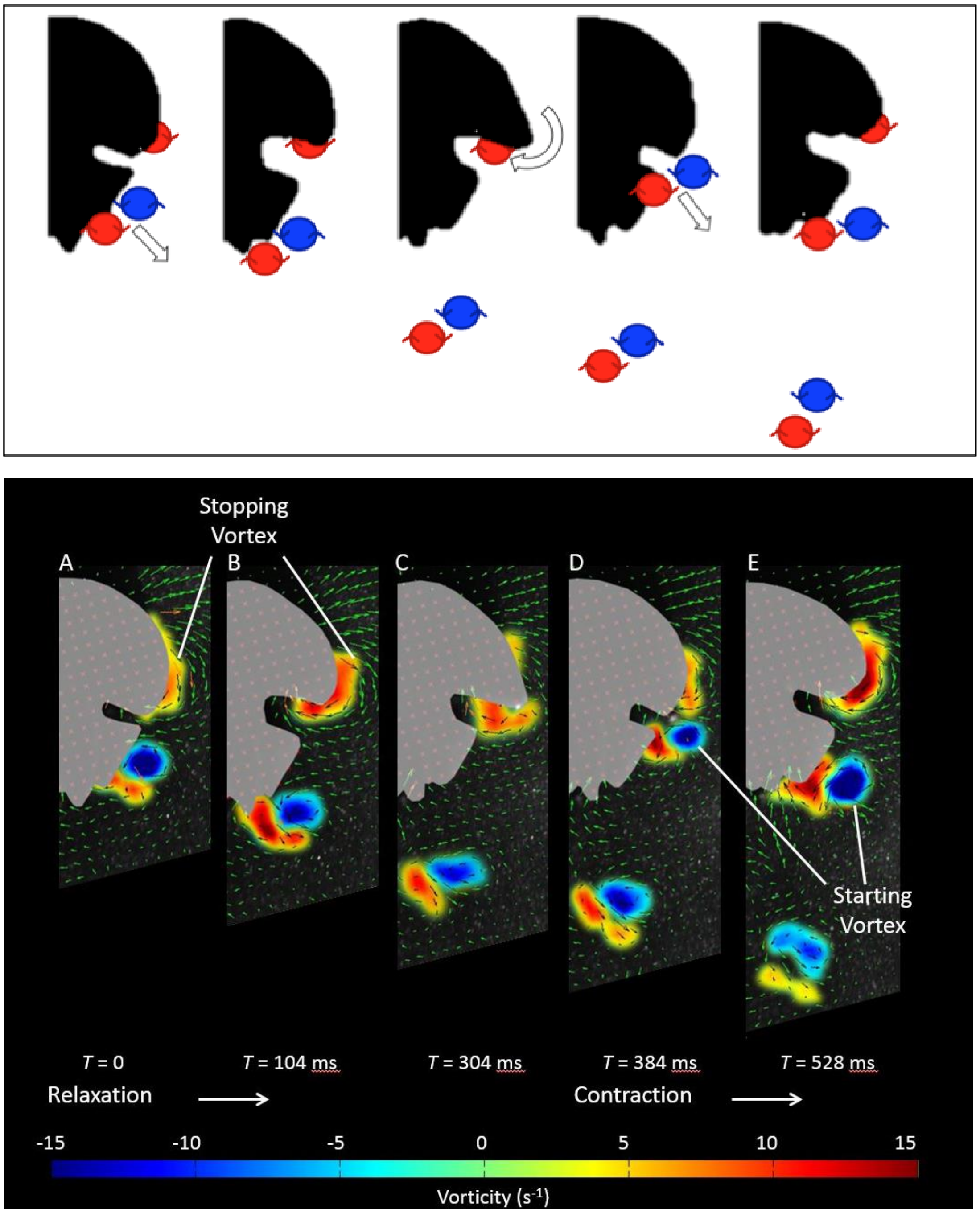

Figure 6.3. The formation and development of stopping and starting vortices in *C. mosaicus*.
(A) At the beginning of the relaxation phase of the swimming cycle, the stopping vortex forms on the outside edge of the bell margin but has low vorticity. (B) Expansion of the bell coupled with bending of the bell margin increase vorticity. (C) At the end of the relaxation phase the vortex ring has been repositioned into the subumbrella cavity of the jellyfish. (D) At the beginning of contraction part of the stopping vortex is ejected from the subumbrella cavity and interacts with the starting vortex that has formed at the bell margin. (E) The vortices move away from the jellyfish as a vortex superstructure. Red and blue regions denote clockwise and counter clockwise rotation, respectively.

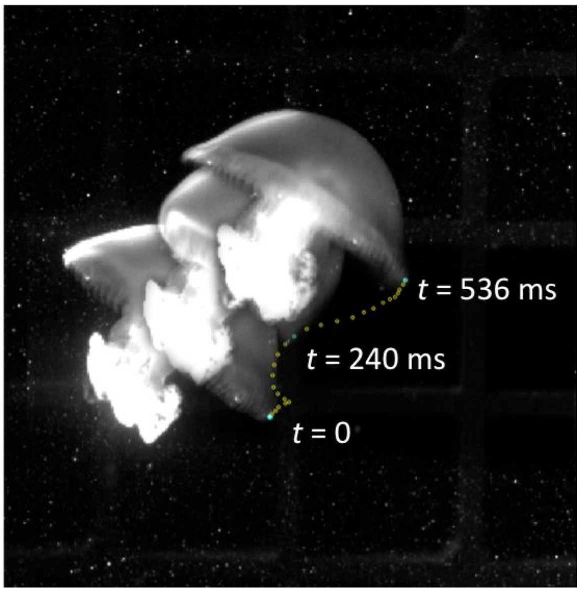

Figure 6.4. Movement of the bell of *C. mosaicus* over one swim cycle. Tracking points are highlighted on one side of the bell.

Visualisation of the wake using PIV revealed that a series of vortices are produced during swimming in *C. mosaicus*. Upon bell contraction the starting vortex interacts with the stopping vortex produced in the preceding contraction cycle, resulting in the formation of a pair of counter-rotating vortex rings (fig. 6.1). Between this counter-rotating vortex pair a jet forms, indicated by the area of high velocity created between the vortices (fig. 6.1A). The result is a mean thrust of 1.38 ± 0.47 mN, which propels the animal forward.

The sequential shedding of the stopping followed by starting vortex, results in the starting vortex being located higher and more laterally than the stopping vortex. The result of this is a jet that is orientated away from the centre line of the jellyfish. Mean jet angle was 26.0 ± 2.2° (range = 13.3° to 42.6°).

The vorticity profile along the *X′* axis is shown in figure 6.2 (axis perpendicular to the centre line of the jellyfish; fig. 6.1A), showing the vorticity of the starting vortex rings and the shed part of the stopping vortex. Vorticity distributions of the shed vortices were typical of a vortex ring (fig. 6.2B; Gharib et al., 1998).

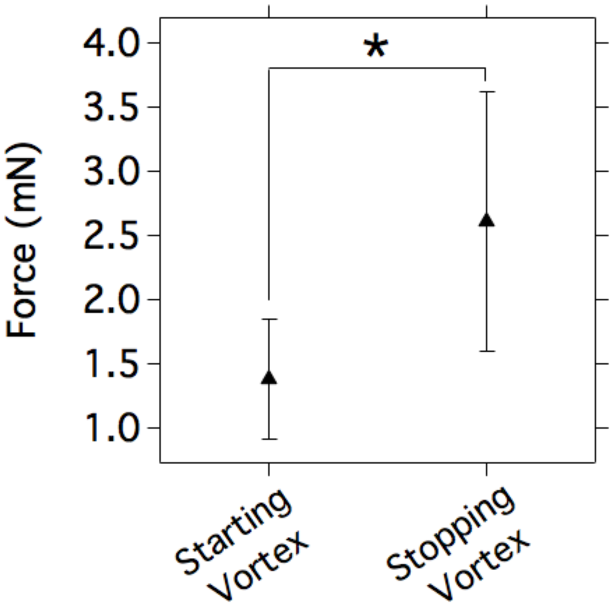

Figure 6.5. Average thrust ± s.e.m produced by stopping and starting vortices in swimming *C. mosaicus*. Significantly more force is produced from the stopping vortex (* = $p<0.05$).

In addition to the fluid that is ejected from the bell during bell contraction, the jellyfish are able to create vortices through the movement of the bell margin, which acts like a paddle as the jellyfish 'rows' through the water. The formation of these vortices starts during bell relaxation, with fluid rolling up over the top of the bell as the bell expands, creating a stopping vortex (fig. 6.3A). The movement of the bell leads to the stopping vortex being repositioned under the jellyfish resulting in the flow of water into the subumbrella cavity (fig. 6.3C). Upon bell contraction this stopping vortex is ejected out of the subumbrella cavity where it interacts with the starting vortex. The starting vortex is formed at the bell margin and joins with the shed stopping vortex to create a downstream vortex superstructure (fig. 6.3D, 6.3E).

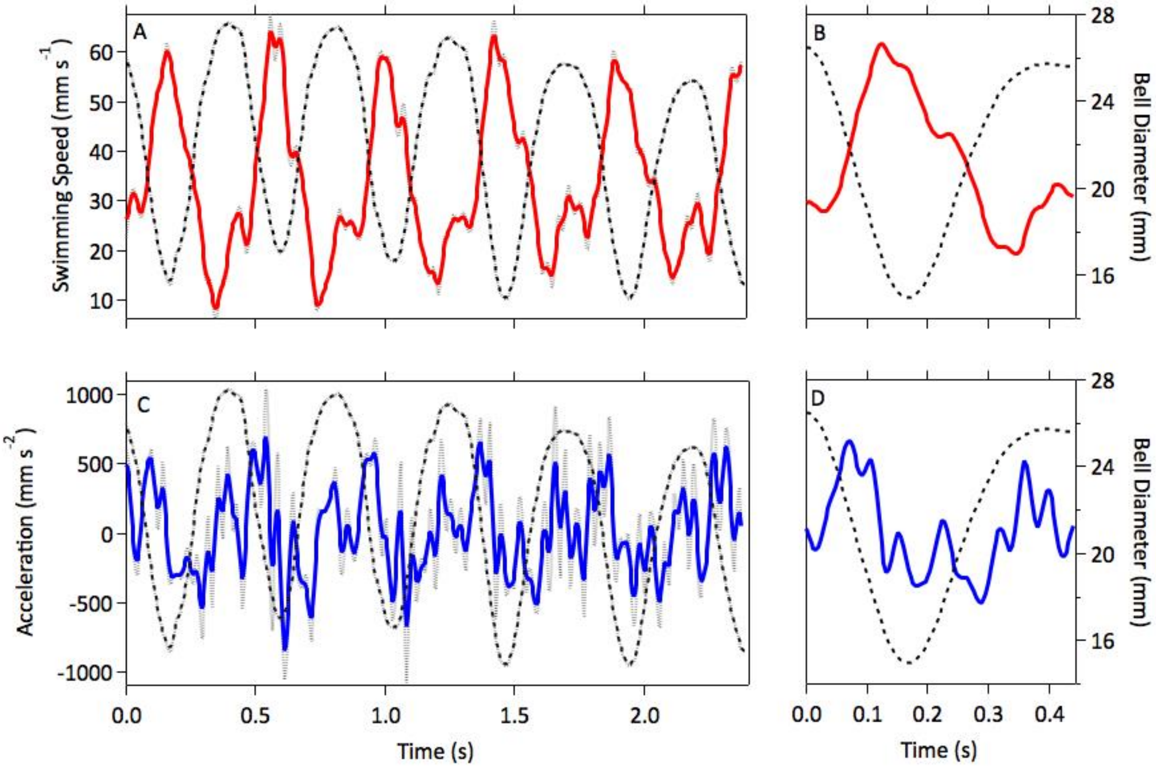

Figure 6.6. Swimming speed and acceleration changes during swimming in *C.* mosaicus. Swimming speed in *C. mosaicus* (red line) with respect to changes in bell diameter (dotted black line) (A). Detailed view of cycle 4 of the same swim (B). Body acceleration in *C. mosaicus* (blue line) with respect to changes in bell diameter (dotted black line) (C). Detailed view of cycle 4 of the same swim (D). Grey dotted lines show raw kinematic data, smoothed data is shown in colour.

The stopping vortices that are created during bell expansion exhibit significantly higher vorticity than that produced by the starting vortex (over the swimming cycle, starting vortex vorticity 3.14 ± 0.6 s^{-1} and stopping vortex vorticity 4.68 ± 0.47 s^{-1} ($t_{1,4}$ = 5.163, $p < 0.01$). Thrust is directly proportional to vorticity and the stopping vortex produced at the end of bell relaxation creates additional thrust, which induces forward motion. The bell margin tips move under the jellyfish during the initial stage of relaxation, creating a region of low pressure on the inner surface of the bell margin in the direction of motion (fig. 6.4). This area of low pressure produces thrust and results in forward motion in the jellyfish. The movement of the bell margin increases fluid circulation in the stopping vortex, which in turn translates to additional thrust that is utilised during the relaxation stage of the swimming cycle. The mean thrust produced by the stopping vortices is significantly higher than that produced by the starting vortices (stopping vortex: 2.62 ± 1.00 mN; starting vortex 1.38 ± 0.47 mN; $t_{1,4}$ = 2.591, $p < 0.05$; fig.6.5).

Radii spacing between subsequent shed vortices ranged from 2.4 - 10.5 radii (mean = 4.65 ±0.64 radii). There was no significant difference in thrust produced in swimming bouts where vortex rings were less than 3 radii apart compared to when the spacing exceeded 3 radii ($t_{1,70} = -0.111$, $p > 0.05$).

6.4.2 Swimming kinematics

Average swimming speed of *C. mosaicus* was 36.22 ± 1.22 mm s^{-1}, whilst mean contraction frequency was 2.18 ± 0.05 Hz. Average duty cycle was 0.34 ± 0.01.

The swimming speed of *C. mosaicus* fluctuated with each completed swimming cycle. Swimming speed increased rapidly following the onset of the contraction phase of the cycle, reaching peak velocity at the end of bell contraction when the bell diameter was smallest (fig. 6.6A). Swimming speed decreased (but the animal continued to move forwards) during bell relaxation, reaching a minimum as the bell reached maximum expansion (fig. 6.6A). Figure 6.6C shows how the forces imparted to the water affect the acceleration of the animal over the course of the swimming cycle, with positive acceleration occurring during bell contraction, during the initial stage of bell relaxation and during the post relaxation phase. The distance covered during the post relaxation phase is on average 11.44±1.02% of the total distance covered during one swim cycle. Whilst on average 37.08±1.51% of the distance travelled by *C. mosaicus* during one swimming cycle was covered in the relaxation phase of the cycle, whilst 51.49±1.53% occurs during bell contraction.

6.4.3 Swimming efficiency

Mean hydrodynamic swimming efficiency was 0.51 ± 0.15. Average slip was calculated as 1.51 ± 0.10. Average formation number was 1.14 ± 0.01 (range = 0.53-2.24).

6.5 Discussion

Swimming performance is determined by the thrust generated by the transfer of momentum to the water, and affects organismal fitness. Natural selection operates on the morphological structures involved in locomotion favouring adaptations that lead to efficient transfer of work from the locomotory muscles into useful kinetic energy in the water. Like other jellyfish, *C. mosaicus* swims by jet propulsion, however, this species has an unusual morphology in that its feeding structures represent a much larger fraction of body mass compared with many other species. It was hypothesised that these feeding adaptations might affect the mechanisms by which thrust is produced in this species, potentially reducing their hydrodynamic efficiency.

The wake structures observed in swimming *C. mosaicus* shared several similarities of those structures observed in other oblate medusae that are considered to be rowers. The formation of a stopping vortex has previously been observed in another species of oblate medusa and is not seen in prolate medusae. The results of this study have revealed a difference in the dynamics of the interaction of the stopping and starting vortices between *C. mosaicus* and *A. aurita* (Dabiri et al., 2005; Gemmell et al., 2013). In *A. aurita* the stopping vortex that is formed during the expansion phase of the swimming cycle, persists in the subumbrella cavity following the end of relaxation. It then contributes to the formation of the subsequent starting vortex. The two vortices interact as they move downstream in the wake, resulting in the starting vortex growing in volume but decreasing in circulation. This is as a result of vorticity cancellation due to the interaction of the starting vortex with the opposite signed vorticity of the preceding stopping vortex. Despite this there is still a net gain in momentum of each wake vortex, as the increased mass of the associated interaction outweighs the loss of circulation due to vorticity cancellation.

6.5.1 Wake structure

The shed vortices of *C. mosaicus* are similar to *A. aurita* in the sense that the starting vortex does interact with the stopping vortex of the proceeding swim cycle and contributes to the wake produced during the power stroke of the cycle. However, in *C. mosaicus* the starting vortex is created in close proximity to the stopping vortex that has formed in the subumbrella cavity. During bell contraction these vortices of opposite rotation move ventrally, away from the medusa in the wake in such a way that large velocities are created along the line of interaction, producing thrust and propelling the jellyfish forward (fig. 6.1B). The sequential shedding of the stopping followed by starting vortex, results in the starting vortex being located higher and more laterally than the stopping vortex. The result of this is that the induced velocities do not lie exactly parallel to the axis of symmetry of the medusa bell, despite it being preferable for thrust production. The PIV results from this experiment are consistent with computational fluid dynamic (CFD) models produced by Sahin et al. (2009) in which they modelled the flow patterns and propulsive performance of the rowing medusa *Aequorea victoria*. Similar vortex interactions were predicted from those models, which agree with the wake structures measured here in *C. mosaicus*.

The study by Sahin et al. (2009) also identified mechanisms of thrust production during bell expansion, parallels can again be drawn on the current study in *C. mosaicus*. During the initial stages of bell expansion the flexible bell margin moves in such a way that the stopping vortex is repositioned to the region around the bell margin of the medusa (fig. 6.3B). This creates regions of low pressure on the inner surface of the bell margin in the direction of travel, which creates thrust and contributes to the forward propulsion of the medusa (fig. 6.4). Flexible bell margins have been demonstrated as having important implications in the formation of vortex rings in jet-paddling medusae (Colin et al., 2012). The highly flexible bell margin associated with oblate medusa is shown to enhance the circulation of the stopping vortices in *C. mosaicus* during the swim cycle. Studies on *A. aurita* have yielded similar results, with stopping vortex circulation increasing as the ring is positioned under the subumbrella surface due to the kinematic movement of the bell during expansion (Gemmell et al., 2014). The result of this movement is thrust from enhanced vorticity and therefore force of the stopping vortex that is formed during bell expansion. It was calculated that on average 37.08% of the distance covered by the jellyfish over one swimming cycle was done so during the recovery phase, demonstrating the impact of this mechanism of propulsion.

Variations in vortex ring spacing provided an opportunity to investigate any vortex interaction effects on thrust during swimming in jellyfish, as had previously been suggested (Weihs, 1977). During swimming vortex ring separation ranged from 2.4 – 10.5 radii between rings, covering the range of within 3 ring radii that Weihs predicted would bring an increase thrust production as a result of the velocity induced on adjacent vortices in the wake (Weihs, 1977). However, there was no significant difference in thrust produced in swimming bouts where vortex rings were less than 3 radii apart compared to when the spacing exceeded 3 radii (*t test*; t = -0.111; d.f.= 70; P > 0.05). This may be due to the fact that Weihs based his models on fully pulsed jets, not the jet-paddle swimming that has been identified in *C. mosaicus*, leading to differences in how individual vortices interact with one another once they have left the jellyfish in the wake. Indeed there was no sign of induced flows between vortex rings during swimming in *C. mosaicus*. This differs from results seen in *A. aurita* (Dabiri et al., 2005), where vortex ring interactions induced a flow of fluid moving toward the central axis of the medusa, suggesting that this type of jet-rowing propulsion might benefit from close vortex ring spacing.

The formation numbers calculated for swimming *C. mosaicus* ranged from 0.53 to 2.24, representing relatively small values for this parameter, this is due to the fact that the fluid ejection time is short for these jellyfish. This allows the jellyfish to avoid pinch-off and the subsequent formation of a trailing jet during swimming; these results are consistent with oblate jellyfish. Prolate jellyfish have been shown to have higher formation numbers of around 8 (Dabiri et al., 2006; Sahin et al., 2009). It has been suggested that these differences may be due to differing foraging strategies amongst species. The low formation numbers of oblate species would be well suited to a passive cruising type of foraging, whereas larger formation numbers are more consistent with the ambush style predation of prolate jellyfish, in which there exist a trade off between efficiency and the ability to produce periodic bursts of high thrust.

6.5.2 Passive energy recapture

C. mosaicus can increase velocity during the post relaxation period of the swimming cycle, when there is no kinematic movement of the bell. The additional thrust is generated as the bell reaches maximum diameter (fig. 6.6A). The low pressure that had built up within at the bell margin during relaxation causes an induced flow of fluid from the stopping vortex. This creates regions of positive pressure within the subumbrella cavity as the jellyfish reaches the end of the swimming cycle. The resultant high pressure creates enough force increasethe forward velocity of the jellyfish. Initially identified by Gemmell et al. (2013) in *A. aurita*, this form of passive energy recapture has been shown to increase swimming efficiency in medusae. This is due to the fact that the additional forward movement comes at almost no metabolic cost to the jellyfish as the refilling of the bell is powered entirely from the release of elastic energy that is stored in the mesoglea during the end of bell contraction, when the potential for hydrodynamic output is low (DeMont and Gosline, 1988). Gemmell et al. estimate that *A. aurita* are able to reduce the cost of transport by 48% through a reduction in metabolic demand bought about by this type of passive energy recapture. It is unlikely that *C. mosaicus* would be able to gain as much benefit from the process as *A. aurita* based on differences in swimming kinematics between the two species. *C. mosaicus* is a very active medusa, shown in these experiments to swim at cycle frequencies of around 2.18 Hz. *A. aurita* on the other hand are more sedentary, generally swimming at around 1 Hz. This lower cycle frequency in *A. aurita* means the post relaxation phase in which there is no movement is quite long in *A. aurita*, around 500 ms in a jellyfish swimming at 1 Hz. This increases the period of time during which the jellyfish can benefit from the thrust associated with passive energy recapture. In contrast, in *C. mosaicus*, the post relaxation time period is around 100ms, and the cycle frequency is higher, meaning that the next contraction begins before the jellyfish can take full advantage of the momentum benefit of the passive energy recapture. In *A. aurita* it was shown that approximately 32% of the total distance travelled in one swim cycle occurred during this post relaxation phase (Gemmell et al., 2013). Passive energy recapture only contributed to around 11% of the total distance covered by *C. mosaicus* in a single cycle.

6.5.3 Swimming efficiency

Previous studies that have measured jellyfish propulsive efficiency have calculated hydrodynamic efficiencies of around 0.09-0.53 (Dabiri et al., 2010). The hydrodynamic efficiency in *C. mosaicus* was 0.51 (±0.15), putting it near the top of efficiency amongst medusae. Compared to some other jet propelling species slip during swimming in *C. mosaicus* (1.52 ± 0.10) was intermediate. For example, in salps slip ranged from 0.2 to 0.8 (Sutherland and Madin, 2010), and in jetting squid slip ranged from 0.25 to 3.5 (Anderson and Grosenbaugh, 2005). The relatively low slip in *C. mosaicus* in comparison to squids is consistent with improved hydrodynamic efficiency expected during jet-paddling, due to the movement of relatively larger volumes of fluid at relatively lower velocities in comparison to jet propulsion (Vogel, 1996).

6.5.4 Impacts of wake on feeding

The structure of the wake likely plays an important role in feeding for *C. mosaicus*. Studies on other jellyfish species have suggested that particular wake characteristics increase fluid mixing at the oral arms, increasing the likelihood of food or prey coming into contact with the feeding tentacles and improving prey capture success rate (Dabiri et al., 2005). In the case of *C. mosaicus* the interaction between stopping and starting vortices results in a mass a fluid that travels down through the oral arms as the vortex rings move away from the medusa in the wake. Similar findings were reported in a study looking at the upside down jellyfish *C. xamachana* (Hamlet et al., 2011). Although a close relative of *C. mosaicus*, *C. xamachana* employs a different foraging strategy. Instead of actively swimming it spends most of its time upside down on the sea floor, using bell pulsations to pass water over its oral arms to facilitate feeding. Interestingly, vortex structures were identified that were similar to those in *C. mosaicus*, with counter rotating vortices emanating from the subumbrella cavity and passing down towards the oral arms, suggesting that bell pulsation may play a key role in feeding in this genus. Although differences in foraging ecology are likely to affect some aspects of how fluid mixing in this way are employed by these two species, the similarities in body morphology and wake dynamics suggest comparable strategies are employed.

6.5.5 Summary

This research reveals fluid interactions in a medusa species with a bell morphology that could be considered intermediary between oblate and prolate. In this paper the thrust production and the mechanisms that produce this thrust have been successfully quantified in *C. mosaicus*. The interaction between stopping and starting vortices creates complex fluid interactions, the result of which is a vortex superstructure consisting of counter rotating vortex rings, producing regions of high velocity along the line of interaction. The relaxation phase of the swim cycle has been shown to be important in thrust production. The ability to produce thrust during bell expansion and passive energy recapture strategies has been demonstrated as being utilized by this species. This work has important implications for understanding the ability for this species to bloom rapidly over a short period of time, with the energetic benefits identified here seemingly allowing them to out compete other species and exploit certain environments other species cannot.

Chapter 7

General Discussion

7.1 The scaling of muscle mass-specific power output

AV Hill's predictions about how animal locomotion should scale with body size were based on assumptions about the geometric similarity of animals and the contractile properties of their muscles (Hill, 1950; Pennycuick and Rezende, 1984). Later research challenged Hill's predictions and predicted alternative relationships between morphology, performance and body size (McMahon, 1973). The work presented in chapters 2 and 3 provides additional data for the arguments of how muscle power should scale with body size, and adds to the small number of studies that have measured the scaling of whole animal muscle power output (Askew et al., 2001).

The main determinant of the scaling of muscle mass-specific power output in scallops was found to be cycle frequency, which scaled with a scaling exponent closer to that expected of elastic similarity (-0.125) over geometric similarity (-0.33). Additionally, the overall scaling exponents of muscle power with body mass were closer to those predicted by elastic similarity (-0.25) rather than geometric similarity (-0.33).

The scallop locomotor system is extremely simple, making it ideal for assessing how varying morphological muscle parameters can affect performance. Being powered by just a single muscle (the adductor muscle), the results of chapter 2 give a good insight into the relationship between variation in strain, duty cycle and cycle frequency on the muscle power output. Chapter 2 represents only the second study that has measured muscle power directly *in vivo* over a range of body sizes. The results generally agree with a study carried out on muscle power output during burst performance in Corvidae (Jackson and Dial, 2011). In both studies muscle power output decreased with increased body size and muscle stress was found to be independent of body size. Muscle strain increased slightly with increased body size in Corvidae, but was independent of size in two scallop species and decreased slightly with increasing size in king scallops. It is important to note that the results gathered in chapter 2 do not agree with all the previous research on the scaling of muscle power output, with some having shown that muscle power output was independent of body size. Studies that have shown this relationship have been focussed on *in vitro* muscle power using the work loop technique (Altringham et al., 1996; Johnson et al., 1993), the disagreement between *in vivo* measurements and *in vitro* results may reflect a limitation in the experimental procedures. Indeed, strain was not optimised in the two previously cited work loop studies and was instead kept constant, however strain has been shown to vary with body size in this thesis and other studies (Jackson and Dial, 2011).

Previous *in vitro* work on isolated muscle fibres and those gathered here in chapter 3 demonstrates the value of these studies to increasing our knowledge of body mass associated effects on animal locomotion (Altringham and Johnston, 1990; Altringham et al., 1996; Johnson et al., 1993). Although it is reasonable to assume that during movement muscles will be subject to varying loads that are difficult to simulate *in vitro*, working on isolated muscles can give a good indication of the intrinsic properties of the muscles. In chapter 3, the contractile characteristics of the adductor muscles from scallops covering a range of body masses were subject to isotonic contractions of varying loads; V_{max} was found to scale negatively with body mass. Although the scaling exponent did not match exactly the scaling of cycle frequency in scallops, the similarity in the relationships suggest that muscles are intrinsically designed towards operating at a shortening velocity that matches their *in vivo* function.

The information gathered on the scaling of muscle power output with body mass in scallops gives a good indication of how power can scale with body mass. This knowledge can be used to infer how whole animal performance may scale in much more complex species, where locomotion is controlled by numerous muscles that would otherwise pose a challenge to study.

7.2 Vortex formation in biological propulsion systems

The ability of jet propelling organisms to produce jet structures that are optimised for thrust is both interesting and potentially vital to their continued survival. Evolution has likely acted on propulsion systems to operate in such a way that enhances the efficiency of movement. During pulsed jets, it has been demonstrated that there exists an optimum in terms of thrust production per unit of expelled fluid. This optimum is produced in jets that are formed near the dimensionless formation number, which results in jets consisting of isolated vortex rings.

Mechanically generated jet pulses have been demonstrated as producing isolated vortex rings and vortex rings pinched off from an elongated jet (Gharib et al., 1998; Krueger and Gharib, 2003; Mohseni et al., 2001; Rosenfeld et al., 1998). From these investigations, it was revealed that there was a limiting principle for the formation of vortex rings, characterised in terms of F. There exists a limit to the impulse and energy that a vortex ring can accept; above F, vortex rings stop growing in size and instead separate from the jet. This limit is reached when F is around 4.

This thesis has quantified jet wake structure in two jet propelling organisms for the first time, (*Nautilus* and scallops) and added to the current understanding of vortex ring formation in rowing medusae. Both *Nautilus* and scallops were shown to produce two jet modes. Significantly, they were both able to produce jets near the theorised optimum for pulsed jet propulsion, F.

Early mechanically generated jet pulse experiments were done in a stationary arrangement, meaning that there was no co-flow component to the study. In biological propulsion systems co-flow will be present as the animal moves through the water, subsequently affecting vortex formation. Later works on mechanically generated jets looked to assess the affect of co-flow on vortex ring formation. It was shown that co-flow lowers *F* due to a decrease in the strength of the shear layer that is feeding the vortex ring, with *F* being <1 when the ratio of co-flow velocity to jet velocity is greater than >0.5 (Krueger et al., 2006). In *Nautilus*, *F* was found to be 2.17, whilst in scallops it was 4. It appears that whilst *Nautilus* are limited in their ability to increase *F* in the presence of co-flow, scallops can maintain *F* at a value that might be expected if co-flow were not present. This likely comes down to the variable jet orifice diameter of the scallop, whilst jet orifice diameter in *Nautilus* remains approximately constant, scallops were shown to decrease their jet diameter by approximately 89%. A decrease in jet orifice size during jet formation has been demonstrated as increasing *F* (Dabiri and Gharib, 2005; Dabiri et al., 2006), this is bought about by an increase in the velocity of the jet as it leaves the orifice, allowing it to keep up with the leading vortex ring and continue to feed it momentum for a longer duration than would be possible through a constant orifice jet.

There appeared to be a benefit in producing jets near *F* in scallops, with a prominent increase in average thrust produced around *F* = 4 compared to jets in which formation number deviated from 4. In *Nautilus*, thrust increased as *F* increased, with more elongated jets producing more thrust than ones consisting of isolated vortex rings.

The benefit of producing jets at formation numbers close to the transition between jet modes has been attributed to the relative contribution of over-pressure at the nozzle exit, that is, the acceleration of ambient fluid relative to the jet (Krueger and Gharib, 2003). Thrust from pulsed jet propulsion is the product of both jet momentum and over-pressure, with isolated vortex rings benefiting from an increase by the contribution of over-pressure. However, over-pressure also leads to more kinetic energy in the flow, so swimming via isolated vortex rings may not always be the most efficient means of propulsion. It seems that whilst scallop propulsion benefits from the increased contribution of over-pressure to jets with an

F of around 4, the jets produced by *Nautilus* are not influenced in the same way, so jet thrust increases concurrently with jet momentum.

7.2.1 Propulsive Efficiency

The hydrodynamic propulsive efficiency of jet propulsion swimming has long been considered inefficient because thrust is produced by imparting relatively large accelerations to relatively small amounts of water (Alexander, 1968; Lighthill, 1970; Vogel, 2003).

Propulsive efficiencies have been calculated as 0.83 in cod (Videler, 1993), 0.7-0.9 in trout and salmon, whilst a value of 0.6 was obtained in fish swimming via thrust produced by their pectoral fins (Webb, 1975). In contrast to this, squid have been shown as having efficiencies of 0.29-0.44 and 0.34-0.48, (Anderson and Demont, 2000; Bartol et al., 2001), with salps having propulsive efficiencies of 0.47-0.55 (Sutherland and Madin, 2010). The research presented in this thesis includes some of the highest propulsive efficiencies measured in cephalopods in which the refilling phase of the cycle is included in the calculation. Hydrodynamic propulsive efficiency in scallops covered a range which included some values higher than those measured in squid (0.19-0.63), whilst jellyfish propulsive efficiency (0.51) was comparable to salps.

Nautilus was found to be amongst the most efficient hydrodynamic swimmers, with efficiencies approaching 0.7 during slow anterior first swimming and fast posterior first swimming. Efficiency seems to be improved by their ability to maintain neutral buoyancy within the water column via the diffusion of gas into its external shell. The *Nautilus* has not lost it shell in the pursuit of speed, instead choosing to remain relatively unchanged during its life history. However the cost of having such a large external shell should not be ignored. The large shell means *Nautilus* are unable to swim at the high speeds attained by squid and cuttlefish. This limits them in both their foraging and avoidance of predators, with *Nautilus* becoming scavengers rather than predators like their cephalopod relatives. Predator avoidance in *Nautilus* is not well studied, but it is assumed that their shell is its first line of defence, being all but incapable of out pacing a potential predator.

The trend in swimming efficiency to increase with increasing speed is something that has been shown in jet propelling squids throughout ontogeny, with increased efficiencies being associated with a reduction in slip (Bartol et al., 2009b; Bartol et al., 2016). The reduction in slip is associated with a decrease in the amount of excess kinetic energy that is lost in the wake. The relationship was similar in scallops and *Nautilus* swimming posterior first, but inverted during anterior first swimming in *Nautilus*. It seems *Nautilus* are able to adjust their swimming mechanics in the pursuit of efficient, slow speed swimming.

During slow anterior first swimming, *Nautilus* adjusted the mechanics of their propulsion system, ejecting fluid at a relatively slower velocity by increasing the length of the contraction phase of their swim cycle, jets emitted at a lower velocity experience a reduction in excess kinetic energy that is lost in the wake. Similar results have been seen in the paralarvae of squid, which have been shown to be more efficient than their adult counterparts by having relatively larger jet funnel apertures that eject fluid at a relatively lower velocity (Bartol et al., 2008). *Nautilus* it seems, are geared towards a sedentary life, with a low cost of locomotion at low speeds, allowing them to forage economically, and persist within the niche that they utilise.

7.3 Future Work

The work presented in chapters 2 and 3 adds knowledge to our understanding of how muscle power output changes with body size. It does not however, provide conclusive evidence in the support of either the predications made from geometric or elastic similarity models. Interspecific variation was found in some of the scaling relationships amongst the three species of scallops studies, so there would likely be even more variability in muscle power quantified in species that employ completely different modes of locomotion. Further studies quantifying muscle power output during different swimming modes, terrestrial locomotion and flight would give a more detailed explanation of how muscle power changes with body mass, and would give an indication of whether any model is able to predict these changes accurately. Moreover, both twitch rise time and $V_{\max}$ were observed to change with varying cycle frequency, suggesting a link between them. However, the mechanisms by which a muscle might contract at a faster rate are yet to be measured.

Fluid dynamics has likely played an integral role in the evolution of jet propulsion amongst marine invertebrates. The finding that *Nautilus* and scallops are able to produce jets of a variety of structures is interesting. Some of these jet structures were found to have formation numbers near to those that would be predicted for optimal vortex ring formation. In order to more accurately reconstruct the wakes of swimming animals, 3-D volumetric flow analysis is necessary. Such techniques would allow for fluid interactions around the whole of the animal to be quantified. This would provide data for refill velocities in *Nautilus*, allowing the data on swimming efficiency presented in this thesis to be corroborated. Work on some of the more proficient species of scallop would likely provide some interesting data. The function of the riblets could be analysed, with their ability to reduce drag quantified, and the vortex structures associated with this reduction identified. 3-D PIV would also give an insightful look into the vortex interactions in *C. mosaicus*, being able visualise the shedding of vortices would allow for the impact of the oral arms to be fully assessed, and theories about their implications to feeding validated.

In order to achieve a full understanding of a particular locomotor system, the energy transduction across all levels of an animals locomotor system needs to be traced, from the chemical energy derived from food through to useful energy transferred to the environment to generate propulsion. A definitive understanding of such a relationship is most likely to be achieved in an organism with a relatively simple locomotor system. Combining PIV data with measurements of muscle power output is the last step of the energy transduction chain. Quantifying the efficiency by which high energy phosphates are produced from chemical substrates would allow for the efficiency of the whole locomotor system to be quantified, tracking of the transfer of energy from the contractile proteins in the muscles to the whole organism, and finally to the environment.

References

Alexander, R. M. (1966). Rubber-like properties of the inner hinge-ligament of Pectinidae. *J. Exp. Biol.* **44**, 119–130.

Alexander, R. M. (1968). Animal mechanics. *Seattle Univ. Wash. Press*.

Alexander, R. M. (1983). Animal mechanics, 2nd edn. Oxford: *Blackwell Scientific Publications*.

Alexander, R. M. (2003). *Principles of animal locomotion*. Princeton University Press.

Altringham, J. D. and Johnston, I. A. (1990). Scaling effects on muscle function: power output of isolated fish muscle fibres performing oscillatory work. *J. Exp. Biol.* **151**, 453–467.

Altringham, J. D., Morris, T., James, R. S. and Smith, C. I. (1996). Scaling effects on muscle function in fast and slow muscles of *Xenopus laevis*. *Exp. Biol. Online* **1**, 1–8.

Altshuler, D., Dudley, R., Heredia, S. and McGuire, J. (2010). Allometry of hummingbird lifting performance. *J. Exp. Biol.* **213**, 725–734.

Anderson, E. J. and Demont, M. E. (2000). The mechanics of locomotion in the squid *Loligo pealei*: locomotory function and unsteady hydrodynamics of the jet and intramantle pressure. *J. Exp. Biol.* **203**, 2851–2863.

Anderson, E. J. and Grosenbaugh, M. A. (2005). Jet flow in steadily swimming adult squid. *J. Exp. Biol.* **208**, 1125–1146.

Anderson, M. E. and Johnston, I. A. (1992). Scaling of power output in fast muscle fibers of the Atlantic cod during cyclical contractions. *J. Exp. Biol.* **170**, 143–154.

Anderson, E. J., MacGillivray, P. S. and Demont, M. E. (1997). Scallop shells exhibit optimization of riblet dimensions for drag reduction. *Biol. Bull.* **192**, 341–344.

Arai, M. N. (1997). *A functional biology of Scyphozoa*. Springer Science & Business Media.

Askew, G. N. and Marsh, R. L. (1997). The effects of length trajectory on the mechanical power output of mouse skeletal muscles. *J. Exp. Biol.* **200**, 3119–3131.

Askew, G. N. and Marsh, R. L. (1998). Optimal shortening velocity (V/Vmax) of skeletal muscle during cyclical contractions: length-force effects and velocity-dependent activation and deactivation. *J. Exp. Biol.* **201**, 1527–1540.

Askew, G. N. and Marsh, R. L. (2001). The mechanical power output of the pectoralis muscle of blue-breasted quail (*Coturnix chinensis*): the *in vivo* length cycle and its implications for muscle performance. *J. Exp. Biol.* **204**, 3587–3600.

Askew, G. N. and Marsh, R. L. (2002). Muscle designed for maximum short-term power output: quail flight muscle. *J. Exp. Biol.* **205**, 2153–2160.

Askew, G. N., Marsh, R. L. and Ellington, C. P. (2001). The mechanical power output of the flight muscles of blue-breasted quail (*Coturnix chinensis*) during take-off. *J. Exp. Biol.* **204**, 3601–3619.

Askew, G. N., Tregear, R. T. and Ellington, C. P. (2010). The scaling of myofibrillar actomyosin ATPase activity in apid bee flight muscle in relation to hovering flight energetics. *J. Exp. Biol.* **213**, 1195–1206.

Astley, H., Abbott, E., Azizi, E., Marsh, R. and Roberts, T. (2013). Chasing maximal performance: a cautionary tale from the celebrated jumping frogs of Calaveras County. *J. Exp. Biol.* **216**, 3947–3953.

Bailey, D. M. and Johnston, I. A. (2005). Scallop swimming kinematics and muscle performance: modelling the effects of “within-animal” variation in temperature sensitivity. *Mar. Freshw. Behav. Physiol.* **38**, 1–19.

Bartol, Patterson, M. R. and Mann, R. (2001). Swimming mechanics and behavior of the shallow-water brief squid *Lolliguncula brevis*. *J. Exp. Biol.* **204**, 3655–3682.

Bartol, I. K., Krueger, P. S., Thompson, J. T. and Stewart, W. J. (2008). Swimming dynamics and propulsive efficiency of squids throughout ontogeny. *Integr. Comp. Biol.* **48**, 720–733.

Bartol, I. K., Krueger, P. S., Stewart, W. J. and Thompson, J. T. (2009a). Pulsed jet dynamics of squid hatchlings at intermediate Reynolds numbers. *J. Exp. Biol.* **212**, 1506–1518.

Bartol, I. K., Krueger, P. S., Stewart, W. J. and Thompson, J. T. (2009b). Hydrodynamics of pulsed jetting in juvenile and adult brief squid *Lolliguncula brevis*: evidence of multiple jet “modes” and their implications for propulsive efficiency. *J. Exp. Biol.* **212**, 1889–1903.

Bartol, I. K., Krueger, P. S., Jastrebsky, R. A., Williams, S. and Thompson, J. T. (2016). Volumetric flow imaging reveals the importance of vortex ring formation in squid swimming tail-first and arms-first. *J. Exp. Biol.* **219**, 392–403.

Basil, J. A., Hanlon, R. T., Sheikh, S. I. and Atema, J. (2000). Three-dimensional odor tracking by *Nautilus pompilius*. *J. Exp. Biol.* **203**, 1409–1414.

Biewener, A. A. (2003). *Animal locomotion*. Oxford University Press.

Biewener, A. A. and Daley, M. A. (2007). Unsteady locomotion: integrating muscle function with whole body dynamics and neuromuscular control. *J. Exp. Biol.* **210**, 2949–2960.

Biewener, A. A. and Gillis, G. B. (1999). Dynamics of muscle function during locomotion: accommodating variable conditions. *J. Exp. Biol.* **202**, 3387–3396.

Biewener, A. A., Konieczynski, D. D. and Baudinette, R. V. (1998). *In vivo* muscle force-length behavior during steady-speed hopping in tammar wallabies. *J. Exp. Biol.* **201**, 1681–1694.

Bomphrey, R. J., Lawson, N. J., Harding, N. J., Taylor, G. K. and Thomas, A. L. (2005). The aerodynamics of *Manduca sexta*: digital particle image velocimetry analysis of the leading-edge vortex. *J. Exp. Biol.* **208**, 1079–1094.

Bone, Q. and Trueman, E. R. (1983). Jet propulsion in salps (Tunicata, Thaliacea). *J. Zool.* **201**, 481–506.

Brett, J. R. and Glass, N. R. (1973). Metabolic rates and critical swimming speeds of sockeye salmon (*Oncorhynchus nerka*) in relation to size and temperature. *J. Fish. Res. Board Can.* **30**, 379–387.

Buchwald, R. and Dudley, R. (2010). Limits to vertical force and power production in bumblebees (Hymenoptera: *Bombus impatiens*). *J. Exp. Biol.* **213**, 426–432.

Caddy, J. (1968). Underwater observations on scallop (*Placopecten magellanicus*) behaviour and drag efficiency. *J. Fish. Board Can.* **25**, 2123–2141.

Carlson, B. A. (2010). Collection and aquarium maintenance of Nautilus. In *Nautilus*, pp. 563–578. Springer.

Chai, P. and Millard, D. (1997). Flight and size constraints: hovering performance of large hummingbirds under maximal loading. *J. Exp. Biol.* **200**, 2757–2763.

Cheng, J.-Y. and DeMont, M. E. (1996a). Hydrodynamics of scallop locomotion: unsteady fluid forces on clapping shells. *J. Fluid Mech.* **317**, 73–90.

Cheng, J. Y. and DeMont, M. E. (1996b). Jet-propelled swimming in scallops: swimming mechanics and ontogenic scaling. *Can. J. Zool.* **74**, 1734–1748.

Cheng, J. Y., Davison, I. and DeMont, M. E. (1996). Dynamics and energetics of scallop locomotion. *J. Exp. Biol.* **199**, 1931–46.

Cheng, J. Y., Pedley, T. J., and Altringham, J. D. (1998). A continuous dynamic beam model for swimming fish. *Philosophical Transactions of the Royal Society of London B: Biological Sciences*, *353*(1371), 981-997.

Colin, S. P. and Costello, J. H. (2002). Morphology, swimming performance and propulsive mode of six co-occurring hydromedusae. *J. Exp. Biol.* **205**, 427–437.

Colin, S. P., Costello, J. H., Dabiri, J. O., Villanueva, A., Blottman, J. B., Gemmell, B. J. and Priya, S. (2012). Biomimetic and live medusae reveal the mechanistic advantages of a flexible bell margin. *PLoS ONE* **7**, e48909.

Dabiri, J. O. and Gharib, M. (2004a). Fluid entrainment by isolated vortex rings. *J. Fluid Mech.* **511**, 311–331.

Dabiri, J. O. and Gharib, M. (2004b). Delay of vortex ring pinchoff by an imposed bulk counterflow. *Phys. Fluids 1994-Present* **16**, L28–L30.

Dabiri, J. O. and Gharib, M. (2005). Starting flow through nozzles with temporally variable exit diameter. *J. Fluid Mech.* **538**, 111–136.

Dabiri, J. O., Colin, S. P., Costello, J. H. and Gharib, M. (2005). Flow patterns generated by oblate medusan jellyfish: field measurements and laboratory analyses. *J. Exp. Biol.* **208**, 1257–1265.

Dabiri, J. O., Colin, S. P. and Costello, J. H. (2006). Fast-swimming hydromedusae exploit velar kinematics to form an optimal vortex wake. *J. Exp. Biol.* **209**, 2025–2033.

Dabiri, J. O., Colin, S. P., Katija, K. and Costello, J. H. (2010). A wake-based correlate of swimming performance and foraging behavior in seven co-occurring jellyfish species. *J. Exp. Biol.* **213**, 1217–1225.

Daniel, T. L. (1985). Cost of locomotion: unsteady medusan swimming. *J. Exp. Biol.* **119**, 149–164.

DeMont, M. E. (1990). Tuned oscillations in the swimming scallop Pecten maximus. *Can. J. Zool.* **68**, 786–791.

DeMont, M. E. and Gosline, J. M. (1988). Mechanics of jet propulsion in the hydromedusan jellyfish, *Polyorchis pexicillatus*: I. Mechanical properties of the locomotor structure. *J. Exp. Biol.* **134**, 313–332.

Didden, N. (1979). On the formation of vortex rings: rolling-up and production of circulation. *Z. Für Angew. Math. Phys. ZAMP* **30**, 101–116.

Dunstan, A. J., Ward, P. D. and Marshall, N. J. (2011). Vertical distribution and migration patterns of *Nautilus pompilius*. *PloS One* **6**, e16311.

Ebashi, S. and Endo, M. (1968). Calcium and muscle contraction. *Prog. Biophys. Mol. Biol.* **18**, 123IN9167–166IN12183.

Edman, K., Elzinga, G. and Noble, M. (1978). Enhancement of mechanical performance by stretch during tetanic contractions of vertebrate skeletal muscle fibres. *J. Physiol.* **281**, 139.

Ellerby, D. J. and Askew, G. N. (2007). Modulation of pectoralis muscle function in budgerigars Melopsitaccus undulatus and zebra finches *Taeniopygia guttata* in response to changing flight speed. *J. Exp. Biol.* **210**, 3789–3797.

Ellington, C. P. (1999). The novel aerodynamics of insect flight: applications to micro-air vehicles. *J. Exp. Biol.* **202**, 3439–3448.

Ellington, C. P., Van Den Berg, C., Willmott, A. P. and Thomas, A. L. (1996). Leading-edge vortices in insect flight. *Nature* **384**, 626-630.

Emerson, S. B. (1978). Allometry and jumping in frogs: helping the twain to meet. *Evolution* **32**, 551–564.

Gemmell, B. J., Costello, J. H., Colin, S. P., Stewart, C. J., Dabiri, J. O., Tafti, D. and Priya, S. (2013). Passive energy recapture in jellyfish contributes to propulsive advantage over other metazoans. *Proc. Natl. Acad. Sci.* **110**, 17904-17909.

Gemmell, B. J., Costello, J. H. and Colin, S. P. (2014). Exploring vortex enhancement and manipulation mechanisms in jellyfish that contributes to energetically efficient propulsion. *Commun. Integr. Biol.* **7**, e29014.

Gharib, M., Rambod, E. and Shariff, K. (1998). A universal time scale for vortex ring formation. *J. Fluid Mech.* **360**, 121–140.

Girgenrath, M. and Marsh, R. L. (1997). *In vivo* performance of trunk muscles in tree frogs during calling. *J. Exp. Biol.* **200**, 3101–3108.

Gordon, A., Huxley, A. F. and Julian, F. (1966). The variation in isometric tension with sarcomere length in vertebrate muscle fibres. *J. Physiol.* **184**, 170.

Graham, L. J. and Soria, J. (1994). A study of an inclined cylinder wake using digital particle image velocimetry. CSIRO. Division of Building, Construction and Engineering.

Hamlet, C., Santhanakrishnan, A. and Miller, L. A. (2011). A numerical study of the effects of bell pulsation dynamics and oral arms on the exchange currents generated by the upside-down jellyfish *Cassiopea xamachana*. *J. Exp. Biol.* **214**, 1911–1921.

Hayami, I. (1991). Living and fossil scallop shells as airfoils: an experimental study. *Paleobiology* **17**, 1–18.

Hill, A. (1938). The heat of shortening and the dynamic constants of muscle. *Proc. R. Soc. Lond. B Biol. Sci.* **126**, 136–195.

Hill, A. V. (1950). The dimensions of animals and their muscular dynamics. *Sci Prog* **38**, 209–230.

Hoerner, S. F. and Borst, H. V. (1975). Fluid-dynamic lift: practical information on aerodynamic and hydrodynamic lift. *NASA STIRecon Tech. Rep. A* **76**, 32167.

Huey, R. B. and Hertz, P. E. (1982). Effects of body size and slope on sprint speed of a lizard *Stellio* (*Agama*). *J. Exp. Biol.* **97**, 401–409.

Itō, H. (1960). Pressure losses in smooth pipe bends. *J. Basic Eng.* **82**, 131–140.

Jackson, B. E. and Dial, K. P. (2011). Scaling of mechanical power output during burst escape flight in the Corvidae. *J. Exp. Biol.* **214**, 452–61.

J. Nichols, Ali Moslemi and Paul Krueger (2008). Performance of a self-propelled pulsed-jet vehicle. In *38th Fluid Dynamics Conference and Exhibit*, American Institute of Aeronautics and Astronautics.

Johnson, T. P., Swoap, S. J., Bennett, A. F. and Josephson, R. K. (1993). Body size, muscle power output and limitations on burst locomotor performance in the lizard *Dipsosaurus dorsalis*. *J. Exp. Biol.* **174**, 199–213.

Josephson, R. K. (1985). Mechanical power output from striated muscle during cyclic contraction. *J. Exp. Biol.* **114**, 493–512.

Josephson, R. K. and Darrell, S. R. (1989). Strain, muscle length and work output in a crab muscle. *J. Exp. Biol.* **145**, 45–61.

Kelly, R. E. and Rice, R. V. (1967). Abductin: a rubber-like protein from the internal triangular hinge ligament of Pecten. *Science* **155**, 208–210.

Kline, S., Reynolds, W., Schraub, F. and Runstadler, P. (1967). The structure of turbulent boundary layers. *J Fluid Mech* **30**, 741–773.

Krueger, P. S. (2001). The significance of vortex ring formation and nozzle exit over-pressure to pulsatile jet propulsion. Diss. California Institute of Technology, 2001.

Krueger, P. S. and Gharib, M. (2003). The significance of vortex ring formation to the impulse and thrust of a starting jet. *Phys. Fluids* **15**, 1271–1281.

Krueger, P. S. and Gharib, M. (2005). Thrust augmentation and vortex ring evolution in a fully-pulsed jet. *AIAA J.* **43**, 792–801.

Krueger, P. S., Dabiri, J. O. and Gharib, M. (2006). The formation number of vortex rings formed in uniform background co-flow. *J. Fluid Mech.* **556**, 147–166.

Lee, H., Yoon, W. and Lim, D. (2008). Description of feeding apparatus and mechanism innemopilema nomurai kishinouye (scyphozoa: rhizostomeae). *Ocean Sci. J.* **43**, 61–65.

Lighthill, M. (1970). Aquatic animal propulsion of high hydromechanical efficiency. *J. Fluid Mech.* **44**, 265–301.

Lindstedt, S. L., McGlothlin, T., Percy, E. and Pifer, J. (1998). Task-specific design of skeletal muscle: balancing muscle structural composition. *Comp. Biochem. Physiol. B Biochem. Mol. Biol.* **120**, 35–40.

Lutz, G. J., Rome, L. C. and American Association for the Advancement of Science (1994). Built for jumping: the design of the frog muscular system. American Association for the Advancement of Science.

Marden, J. H. (1994). From damselflies to pterosaurs: how burst and sustainable flight performance scale with size. *Am. J. Physiol.-Regul. Integr. Comp. Physiol.* **266**, R1077–R1084.

Marsh, R. L. (1988). Ontogenesis of contractile properties of skeletal muscle and sprint performance in the lizard *Dipsosaurus dorsalis*. *J. Exp. Biol.* **137**, 119–139.

Marsh, R. L. (1990). Deactivation rate and shortening velocity as determinants of contractile frequency. *Am. J. Physiol. - Regul. Integr. Comp. Physiol.* **259**, R223–R230.

Marsh, R. L. (1994). Jumping ability of anuran amphibians. *Adv. Vet. Med.* **2**, 51–111.

Marsh, R. L. (1999). How muscles deal with real-world loads: the influence of length trajectory on muscle performance. *J. Exp. Biol.* **202**, 3377–3385.

Marsh, R. and Bennett, A. (1985). Thermal dependence of isotonic contractile properties of skeletal muscle and sprint performance of the lizard *Dipsosaurus dorsalis*. *J. Comp. Physiol. B* **155**, 541–551.

Marsh, R. L. and Bennett, A. F. (1986). Thermal dependence of contractile properties of skeletal muscle from the lizard *Sceloporus occidentalis* with comments on methods for fitting and comparing force-velocity curves. *J. Exp. Biol.* **126**, 63–77.

Marsh, R. L. and Olson, J. M. (1994). Power output of scallop adductor muscle during contractions replicating the *in vivo* mechanical cycle. *J. Exp. Biol.* **193**, 139–156.

Marsh, R. L., Olson, J. M. and Guzik, S. K. (1992). Mechanical performance of the scallop adductor muscle during swimming. *Nature* **357**, 411–413.

Maxworthy, T. (1977). Some experimental studies of vortex rings. *J. Fluid Mech.* **81**, 465–495.

McComas, A. J. (1996). Skeletal muscle: form and function. Champaign, IL: Human Kinetics.

McHenry, M. J. and Jed, J. (2003). The ontogenetic scaling of hydrodynamics and swimming performance in jellyfish (*Aurelia aurita*). *J. Exp. Biol.* **206**, 4125–4137.

McMahon, T. (1973). Size and shape in biology. *Science* **179**, 1201–1204.

McMahon, T. A. (1975). Using body size to understand the structural design of animals: quadrupedal locomotion. *J. Appl. Physiol.* **39**, 619–627.

Melling, A. (1997). Tracer particles and seeding for particle image velocimetry. *Meas. Sci. Technol.* **8**, 1406.

Miller, K., Monteforte, P. B. and Landis, L. F. (1993). Scaling of locomotor performance and enzyme activity in the leopard frog, *Rana pipiens*. *Herpetologica* **49**, 383–392.

Millman, B. M. (1967). Mechanisms of contraction in molluscan muscle. *Am. Zool.* **7**, 583–591.

Mohseni, K. and Gharib, M. (1998). A model for universal time scale of vortex ring formation. *Phys. Fluids 1994-Present* **10**, 2436–2438.

Mohseni, K., Ran, H. and Colonius, T. (2001). Numerical experiments on vortex ring formation. *J. Fluid Mech.* **430**, 267–282.

Moore, J. and Trueman, E. (1971). Swimming of the scallop, *Chlamys opercularis* (L.). *J. Exp. Mar. Biol. Ecol.* **6**, 179–185.

Morton, B. (1980). Swimming in *Amusium pleuronectes* (Bivahia: Pectinidae). *J. Zool.* **190**, 375–404.

Mullins, J. (1997). Secrets of a perfect skin. *New Sci.* 28–31.

O'Dor, R. (1982). Respiratory metabolism and swimming performance of the squid, *Loligo opalescens*. *Can. J. Fish. Aquat. Sci.* **39**, 580–587.

O'Dor, R. K., Wells, J. and Wells, M. J. (1990). Speed, jet Pressure and oxygen consumption relationships in free-swimming *Nautilus*. *J. Exp. Biol.* **154**, 383–396.

Olcay, A. B. and Krueger, P. S. (2010). Momentum evolution of ejected and entrained fluid during laminar vortex ring formation. *Theor. Comput. Fluid Dyn.* **24**, 465–482.

Olson, J. M. and Marsh, R. L. (1993). Contractile properties of the striated adductor muscle in the bay scallop *Argopecten irradians* at several temperatures. *J. Exp. Biol.* **176**, 175–193.

Pennycuick, C. (1975). Mechanics of flight. *Avian Biol.* **5**, 1–75.

Pennycuick, C. J. (2008). *Modelling the flying bird*. Elsevier.

Pennycuick, C. J. and Rezende, M. A. (1984). The specific power output of aerobic muscle, related to the power density of mitochondria. *J. Exp. Biol.* **108**, 377–392.

Peplowski, M. M. and Marsh, R. L. (1997). Work and power output in the hindlimb muscles of Cuban tree frogs *Osteopilus septentrionalis* during jumping. *J. Exp. Biol.* **200**, 2861–2870.

Quoy, J. R. C. and Gaimard, P. (1824). Zoologie. Imprimerie royale.

Rall, J. A. (1981). Mechanics and energetics of contraction in striated muscle of the sea scallop, *Placopecten magellanicus*. *J. Physiol.* **321**, 287–295.

Rand, A. S. and Rand, P. J. (1966). The relation of size and distance jumped in *Bufo marinus*. *Herpetologica* **22**, 206–209.

Rayner, J. and Aldridge, H. (1985). Three-dimensional reconstruction of animal flight paths and the turning flight of microchiropteran bats. *J. Exp. Biol.* **118**, 247–265.

Roberts, T. J., Marsh, R. L., Weyand, P. G. and Taylor, C. R. (1997). Muscular force in running turkeys: the economy of minimizing work. *Science* **275**, 1113–1115.

Roberts, T. J., Higginson, B. K., Nelson, F. E. and Gabaldón, A. M. (2007). Muscle strain is modulated more with running slope than speed in wild turkey knee and hip extensors. *J. Exp. Biol.* **210**, 2510–2517.

Roberts, T. J., Abbott, E. M. and Azizi, E. (2011). The weak link: do muscle properties determine locomotor performance in frogs? *Philos. Trans. R. Soc. B Biol. Sci.* **366**, 1488–1495.

Rome, L. C., Sosnicki, A. A. and Goble, D. O. (1990). Maximum velocity of shortening of three fibre types from horse soleus muscle: implications for scaling with body size. *J. Physiol.* **431**, 173–185.

Rosenfeld, M., Rambod, E. and Gharib, M. (1998). Circulation and formation number of laminar vortex rings. *J. Fluid Mech.* **376**, 297–318.

Sahin, M., Mohseni, K. and Colin, S. P. (2009). The numerical comparison of flow patterns and propulsive performances for the hydromedusae *Sarsia tubulosa* and *Aequorea victoria*. *J. Exp. Biol.* **212**, 2656–2667.

Schmidt-Nielsen, K. (1984). Scaling: why is size so important. *N. Y. Camb. Univ. Press*.

Seow, C. Y. and Ford, L. E. (1991). Shortening velocity and power output of skinned muscle fibers from mammals having a 25,000-fold range of body mass. *J. Gen. Physiol.* **97**, 541–560.

Shusser, M. and Gharib, M. (2000). Energy and velocity of a forming vortex ring. *Phys. Fluids 1994-Present* **12**, 618–621.

Southcott, R. (1982). Jellyfishes (Classes Scyphozoa and Hydrozoa). *Mar. Invertebr. South. Aust. Part I* 115–159.

Stamhuis, E. J. and Nauwelaerts, S. (2005). Propulsive force calculations in swimming frogs II. Application of a vortex ring model to DPIV data. *J. Exp. Biol.* **208**, 1445–1451.

Stephens, P. J. and Boyle, P. R. (1978). Escape responses of the queen scallop *Chlamys opercularis* (L.) (Mollusca: Bivalvia). *Mar. Behav. Physiol.* **5**, 103–113.

Stewart, W. J., Bartol, I. K. and Krueger, P. S. (2010). Hydrodynamic fin function of brief squid, *Lolliguncula brevis*. *J. Exp. Biol.* **213**, 2009–2024.

Sutherland, K. R. and Madin, L. P. (2010). Comparative jet wake structure and swimming performance of salps. *J. Exp. Biol.* **213**, 2967–2975.

Thielicke, W. and Stamhuis, E. J. (2012). PIVlab - Time-resolved digital particle image velocimetry tool for MATLAB. PIVver. 1.32. *PIVver 132*.

Tobalske, B. W. and Dial, K. P. (2000). Effects of body size on take-off flight performance in the Phasianidae (Aves). *J. Exp. Biol.* **203**, 3319–3332.

Tremblay, I., Samson-Dô, M. and Guderley, H. E. (2015). When behavior and mechanics meet: scallop swimming capacities and their hinge ligament. *J. Shellfish Res.* **34**, 203–212.

Trueman, E. R. (1953). Observations on certain mechanical properties of the ligament of Pecten. *J. Exp. Biol.* **30**, 453–467.

Videler, J. J. (1993). Fish swimming. Springer Science & Business Media.

Videler, J. and Hess, F. (1984). Fast continuous swimming of two pelagic predators, saithe (*Pollachius virens*) and mackerel (*Scomber scombrus*): a kinematic analysis. *J. Exp. Biol.* **109**, 209–228.

Vogel, S. (1981). Life in moving fluids. *Phys. Biol. Tlow Princet. N Princet. Univ. Press Princet. N. J.*

Vogel, S. (1996). Life in moving fluids: the physical biology of flow. Princeton University Press.

Vogel, S. (2003). Comparative biomechanics: life's physical world Princeton University Press. *Princet. N. J. USA*.

Ward, P. (1984). Is *Nautilus* a living fossil? In *Living Fossils*, pp. 247–256. Springer.

Warrick, D. R., Tobalske, B. W. and Powers, D. R. (2009). Lift production in the hovering hummingbird. *Proc. R. Soc. Lond. B Biol. Sci.* **276**, 3747–3752.

Webb, P. W. (1971). The swimming energetics of trout: I. Thrust and power output at cruising speeds. *J. Exp. Biol.* **55**, 489–520.

Webb, P. W. (1975). Efficiency of pectoral-fin propulsion of *Cymatogaster aggregata*. In *Swimming and flying in nature*, pp. 573–584. Springer.

Webb, P., Kostecki, P. and Stevens, E. D. (1984). The effect of size and swimming speed on locomotor kinematics of rainbow trout. *J. Exp. Biol.* **109**, 77–95.

Webber, D. M. and O'Dor, R. K. (1986). Monitoring the metabolic rate and activity of free-swimming squid with telemetered jet pressure. *J. Exp. Biol.* **126**, 205–224.

Weihs, D. (1977). Periodic jet propulsion of aquatic creatures. *Forsch Zool* **24**, 171–175.

Weis-Fogh, T. and Alexander, R. (1977). The sustained power output from striated muscle. *Scale Eff. Anim. Locomot.* 511–525.

Wells, M. and O'Dor, R. (1991). Jet propulsion and the evolution of the cephalopods. *Bull. Mar. Sci.* **49**, 419–432.

Westergaard, C. and Buchhave, P. (1993). PIV: comparison of three autocorrelation techniques. pp. 535–541. International Society for Optics and Photonics.

Wilson, R. S., Franklin, C. E. and James, R. S. (2000). Allometric scaling relationships of jumping performance in the striped marsh frog *Limnodynastes peronii*. *J. Exp. Biol.* **203**, 1937–1946.

Wong, C. Y., Nathan, G. J. and Kelso, R. M. (2012). PIV as a complement to LDA in the study of an unsteady oscillating turbulent flow, the particle image velocimetry - characteristics, limits and possible applications. *Giovanna Cavazzini Ed* ISBN: 978–953–51–0625–8, InTech, DOI: 10.5772/34696.

Zug, G. R. and Altig, R. (1978). Anuran locomotion - strucuture and function: the jumping forces of frogs. *J. Wash. Acad. Sci.* **68**, 144.